

Multifrequency methods for Electrical Impedance Tomography

Emma Rosa Malone

A dissertation submitted in partial fulfillment
of the requirements for the degree of
Doctor of Philosophy
of
University College London.

Department of Medical Physics and Biomedical Engineering
University College London

2015

Author Declaration

I, Emma Rosa Malone, confirm that the work presented in this thesis is my own. Where information has been derived from other sources, I confirm that this has been indicated in the work.

Abstract

Multifrequency Electrical Impedance Tomography (MFEIT) is an emerging imaging modality which exploits the dependence of tissue impedance on frequency to recover images of conductivity. Given the low cost and portability of EIT scanners, MFEIT could provide emergency diagnosis of pathologies such as acute stroke, brain injury and breast cancer. Whereas time-difference, or dynamic, EIT is an established technique for monitoring lung ventilation, MFEIT has received less attention in the literature, and the imaging methodology is at an early stage of development. MFEIT holds the unique potential to form images from static data, but high sensitivity to noise and modelling errors must be overcome.

The subject of this doctoral thesis is the investigation of novel techniques for including spectral information in the image reconstruction process. The aim is to improve the ill-posedness of the inverse problem and deliver the first imaging methodology with sufficient robustness for clinical application. First, a simple linear model for the conductivity is defined and a simultaneous multifrequency method is developed. Second, the method is applied to a realistic numerical model of a human head, and the robustness to modelling errors is investigated. Third, a combined image reconstruction and classification method is developed, which allows for the simultaneous recovery of the conductivity and the spectral information by introducing a Gaussian-mixture model for the conductivity. Finally, a graph-cut image segmentation technique is integrated in the imaging method.

In conclusion, this work identifies spectral information as a key resource for producing MFEIT images and points to a new direction for the development of MFEIT algorithms.

Acknowledgements

It has been a great privilege to work with my principle supervisor, Simon Arridge, who has provided me with unfaltering intellectual and moral support throughout my doctoral studies. I am grateful to David Holder for introducing me to the topic of my dissertation, and Timo Betcke for many helpful discussions.

I extend my thanks to Gustavo Sato Dos Santos, Markus Jehl, Jem Hebden, Gary Royle, Ben Cox, Bruce Amm, David Davenport, and to my colleagues in both the EIT group and CMIC, each of whom have provided me with significant assistance and support as I undertook this work.

I am grateful to my PhD examiners Ville Kolehmainen and Dean Barratt for their many valuable comments.

Finally, I wish to thank my parents Sinéad and Patrick, my siblings Hannah and Stephen, my partner Sam, and my friends for their limitless patience and encouragement.

This work was funded by the EPSRC grant EP/J50225X/1.

Emma Rosa Malone, 2014.

Contents

1	Overview	15
1.1	Introduction	15
1.2	Purpose	18
1.3	Structure	19
1.4	Publications	19
2	Literature review	21
2.1	Introduction	21
2.1.1	Bioimpedance	21
2.1.2	EIT measurements	23
2.1.3	EIT imaging modalities	25
2.1.4	EIT of the human head	27
2.2	Image reconstruction principles	32
2.2.1	Introduction	32
2.2.2	Ill-posedness	33
2.3	Mathematical problem definition of EIT	34
2.4	Forward problem	36
2.4.1	Weak formulation	37
2.4.2	Numerical methods	37
2.4.3	Mesh generation	38
2.4.4	Electrode model	39
2.4.5	Galerkin FEM formulation	40
2.4.6	Sensitivity matrix	42
2.5	Inverse problem	43
2.5.1	Introduction	43
2.5.2	Regularization	44
2.5.3	Linear algorithms	45
2.5.4	Non-linear iterative algorithms	48

2.5.5	Nonlinear direct methods	53
2.5.6	Other methods	55
2.5.7	Regularization parameter selection	56
2.6	Multifrequency EIT	57
2.6.1	Introduction	57
2.6.2	Simple frequency-difference	58
2.6.3	Weighted frequency difference	58
2.7	Image segmentation	60
2.7.1	Introduction	60
2.7.2	Labelling problem with MRF prior	60
2.7.3	Graph cut optimization	61
3	Multifrequency EIT using spectral constraints	64
3.1	Introduction	64
3.1.1	Overview	64
3.1.2	Related work	64
3.1.3	Purpose	65
3.1.4	Experimental design	65
3.2	Methods	66
3.2.1	Fraction model	66
3.2.2	Fraction image reconstruction	68
3.2.3	Fraction image reconstruction: indirect method	72
3.2.4	Image quantification	73
3.3	Results	74
3.3.1	Tissue impedance spectra	74
3.3.2	Numerical Validation	74
3.3.3	Robustness to spectral errors	75
3.3.4	Phantom study	78
3.3.5	Comparison with indirect multifrequency imaging	79
3.3.6	Comparison with WFD conductivity imaging	81
3.3.7	Spectral constraints method for nonlinear case	81
3.3.8	Multiple tissue case	82
3.3.9	Approximation error evaluation	84
3.4	Discussion	88

3.4.1	Robustness to spectral errors	88
3.4.2	Comparison with indirect multifrequency imaging	88
3.4.3	Comparison with WFD conductivity imaging	89
3.4.4	Multiple tissue case	89
3.4.5	Approximation error evaluation	90
3.5	Conclusion	90
4	Stroke type differentiation using spectrally constrained MFEIT	92
4.1	Introduction	92
4.1.1	Overview	92
4.1.2	Related work	92
4.1.3	Purpose	93
4.1.4	Experimental design	93
4.2	Methods	95
4.2.1	Model and tissue impedance spectra	95
4.2.2	Data simulation	96
4.2.3	Image reconstruction	97
4.2.4	Numerical validation	97
4.2.5	Error simulation	98
4.2.6	Image quantification	98
4.3	Results	99
4.3.1	Numerical validation	99
4.3.2	Erroneous electrode positions	100
4.3.3	Erroneous tissue spectra	100
4.3.4	Erroneous electrode impedances	101
4.4	Discussion	105
4.4.1	Numerical validation	105
4.4.2	Erroneous electrode positions	105
4.4.3	Erroneous tissue spectra	105
4.4.4	Erroneous electrode impedances	106
4.4.5	Technical remarks	106
4.5	Conclusion	107
5	A reconstruction-classification method for MFEIT	108
5.1	Introduction	108

5.1.1	Overview	108
5.1.2	Related work	108
5.1.3	Purpose	109
5.1.4	Experimental design	109
5.2	Method	111
5.2.1	Multinomial model	111
5.2.2	Combined reconstruction-classification outline	112
5.2.3	Reconstruction	113
5.2.4	Classification	114
5.2.5	Frequency-difference reconstruction-classification outline	116
5.2.6	Frequency-difference reconstruction	117
5.2.7	Frequency-difference classification	118
5.2.8	Spatial smoothing	118
5.2.9	Image quality evaluation	118
5.3	Results	119
5.3.1	Numerical phantom and data simulation	119
5.3.2	RC with homogeneous MRF regularization	119
5.3.3	Robustness to spectral errors	120
5.3.4	RC with independent elements	121
5.3.5	RC with label-dependant MRF regularization	121
5.3.6	Frequency-difference RC: numerical validation	121
5.3.7	Image quality evaluation	122
5.3.8	Comparison with other methods	122
5.3.9	Phantom experiment	123
5.4	Discussion	133
5.4.1	Numerical results	133
5.4.2	Robustness to spectral errors	133
5.4.3	Frequency-difference combined reconstruction-classification	133
5.4.4	Comparison with other methods	134
5.4.5	Phantom experiment	135
5.5	Conclusion	135
6	Reconstruction-classification using graph cut optimization	137
6.1	Introduction	137

6.1.1	Overview	137
6.1.2	Related work	137
6.1.3	Purpose	138
6.1.4	Experimental design	138
6.2	Method	138
6.2.1	Bayesian formulation of the inverse problem of EIT	139
6.2.2	Labelling in MFEIT	139
6.2.3	Hidden Markov Random field model	140
6.2.4	Gaussian HMRF model	140
6.2.5	Gaussian HMRF model-based labelling in MFEIT	141
6.2.6	Reconstruction-classification with HMRF: outline	142
6.2.7	Reconstruction	143
6.2.8	Labelling with graph-cut optimization	143
6.2.9	Classification: fitting the HMRF model with EM	144
6.3	Results	146
6.3.1	Numerical validation	146
6.3.2	Robustness to spectral errors	146
6.3.3	Phantom experiment	146
6.4	Discussion	151
6.4.1	Methodology	151
6.4.2	Numerical validation	151
6.4.3	Robustness to spectral errors	152
6.4.4	Phantom experiment	152
6.5	Conclusion	152
7	Conclusion	154
7.1	Summary of findings	154
7.2	Limitations and future work	156
7.2.1	Conductivity modelling	156
7.2.2	Boundary modelling errors	157
7.2.3	Algorithm speed	158
	Bibliography	158

List of Figures

2.1	Cole-Cole model of electrical properties of a cell.	22
2.2	The movement of current through cells at low and high frequencies. . .	22
2.3	The UCL Mk 2.5 EIT system.	23
2.4	Diagram of the two-electrode and four-electrode measurement methods.	23
2.5	Conductivity of tissues in the head.	28
2.6	Binary image segmentation example.	61
2.7	Schematic of graph cut optimization method.	62
3.1	Direct and indirect fraction reconstruction.	73
3.2	Conductivity values of test tissues.	75
3.3	Fraction reconstruction numerical validation model.	76
3.4	Fraction reconstruction numerical validation images.	76
3.5	Robustness to spectral errors images.	77
3.6	Robustness to spectral errors image quantification.	78
3.7	Phantom experiment setup.	78
3.8	Phantom experiment fraction images.	79
3.9	Absolute conductivity images of phantom.	80
3.10	Indirect multifrequency imaging results.	80
3.11	Image quantification for absolute conductivity and fraction images. . . .	81
3.12	WFD conductivity images of phantom.	82
3.13	Image quantification for WFD conductivity and fraction images.	82
3.14	WFD comparison simulation model.	83
3.15	WFD comparison simulation fraction images.	83
3.16	WFD comparison simulation conductivity images.	84
3.17	Four-tissue case tissue spectra.	85
3.18	Four-tissue case numerical model.	85
3.19	Four-tissue case fraction images.	86
3.20	Approximation error evaluation model.	86
3.21	Mean fraction model approximation error.	87

4.1	Conductivity spectra of tissues in the head.	96
4.2	Human head model.	96
4.3	Numerical validation imaging results.	99
4.4	Numerical validation image quantification results.	99
4.5	Electrode areas for the fine and coarse meshes.	100
4.6	Erroneous electrode positions imaging results.	101
4.7	Erroneous electrode positions image quantification results.	101
4.8	Erroneous tissue spectra imaging results.	102
4.9	Erroneous tissue spectra image quantification results.	102
4.10	Frequency-difference conductivity spectra of tissues in the head.	103
4.11	Erroneous conductivity spectra imaging results.	104
4.12	Erroneous conductivity spectra image quantification results.	104
5.1	Numerical phantom model.	120
5.2	Reconstruction-classification with homogeneous MRF.	124
5.3	Robustness to errors in the initial guess of the tissue spectra.	125
5.4	Reconstruction-classification in the case of independent elements.	126
5.5	Reconstruction-classification with label-dependent MRF.	127
5.6	Frequency-difference reconstruction-classification model.	128
5.7	Frequency-difference reconstruction-classification results.	129
5.8	Image quality of numerical results.	130
5.9	Comparison with other methods.	130
5.10	Phantom experiment setup and RC results for absolute data.	131
5.11	Phantom experiment RC results for frequency-difference data.	132
6.1	Schematic representation of the prior models used in RC.	141
6.2	Reconstruction-classification with graph cuts, numerical validation.	147
6.3	Reconstruction-classification with graph cuts, image quantification.	148
6.4	Robustness to errors in the initial guess of the tissue spectra.	149
6.5	Phantom experiment images obtained by RC with graph cuts.	150

List of symbols

Chapter 2

Symbol	Description
Z	Impedance
R	Resistance
C	Capacitance
ω	Frequency
I	Current
V	Voltage
L	Number of electrodes
l	Electrode index
\boldsymbol{v}	Voltage measurements
$p(\boldsymbol{x})$	Probability of \boldsymbol{x}
$\mathcal{L}(\boldsymbol{x}, \boldsymbol{y})$	Negative log-likelihood of \boldsymbol{y} given \boldsymbol{x}
A	Forward map
Ψ	Regularization function
τ	Regularization parameter
\boldsymbol{h}	Measurement noise
Σ_y	Covariance of \boldsymbol{y}
Ω	Parameter space domain
$\partial\Omega$	Parameter space boundary
γ	Admittivity
σ	Conductivity
ϵ	Permittivity
\boldsymbol{E}	Electric field
\boldsymbol{J}	Current density
\boldsymbol{D}	Electric displacement
\boldsymbol{H}	Magnetic flux
\boldsymbol{B}	Magnetic field

ν	Permeability
ρ	Electric charge density
\mathbf{n}	Outward normal unit vector
z	Contact impedance
P	Number of current injection patterns
p	Current pattern index
Q	Number of measurement pairs
q	Measurement pair index
K	Number of measurements
k	Measurement index
M	Number of nodes
N	Number of elements
n	Element index
Φ	Objective function
\mathbf{J}	Jacobian of the forward map
$\nabla\Phi$	Gradient of the objective function
$\nabla^2\Phi$	Hessian of the objective function
\mathbf{d}	Search direction
α	Step size
\mathcal{T}	Labels space
\mathcal{V}	Voxels space
\mathcal{X}	Image labellings space

Chapter 3

Symbol	Description
M	Number of frequencies
i	Frequency index
J	Number of tissues
j	Tissue index
ϵ_{ij}	Conductivity of tissue j at frequency i
f_{nj}	Fraction of element n and tissue j
\mathbf{F}	Fraction matrix of values f_{nj} , size $N \times T$

Chapter 5

Symbol	Description
ζ_{nj}	Class/tissue labels
λ_j	Class probability
\mathbf{m}_j	Class spectrum mean
$\mathbf{\Sigma}_j$	Class spectrum variance
$\mathbf{\Gamma}_j$	Class parameter of the NIW distribution
ν_j	Class parameter of the NIW distribution
$\boldsymbol{\theta}_j$	The pair $(\mathbf{m}_j, \mathbf{\Sigma}_j)$
$\boldsymbol{\sigma}$	Conductivity matrix of values σ_{ni} , size $N \times M$
\mathbf{v}	Data matrix of values v_{ki} , size $K \times M$
ρ_{ni}	Reconstruction auxiliary variable $\rho_{ni} = \log \sigma_{ni}$
r_{nj}	Responsibility

Chapter 6

Symbol	Description
ξ	Regularization parameter for labelling problem

Chapter 1

Overview

1.1 Introduction

Electrical Impedance Tomography (EIT) is a non-invasive technique for imaging physiological and pathological body functions. The underlying principle is to exploit the electrical properties of biological tissues to extract information about the anatomy and physiology of organs. A small amount of current is injected into the body and voltage measurements are acquired using peripheral electrodes. A reconstruction algorithm based on a modified formulation of Ohm's law for current flow in a volume is implemented to image the impedance distribution of the subject in two or three dimensions.

If current travelled in a straight, collimated beam between source and sink, then an image of conductivity could be reconstructed using a simple backprojection algorithm, in the same way as for Computed Tomography. Only the conductive tissue crossed by the current would contribute to the measurements, therefore the information contained in the measurements could be spread back along the localized current flow path. In reality, although the current density is higher near the electrodes, the current flows in the whole object, and the spatial information provided by the measurements is poor. By mapping the current density in the domain, a measure of the sensitivity of the data to changes in conductivity in different locations is obtained. This provides an indication for each injection pattern of where to "place" the information contained in the measurements, which must be spread out unevenly across the domain. Most commonly used EIT reconstruction algorithms are based on sensitivity mapping (see section 2.5). In this sense EIT is non-local, and all voxels and measurements must be considered at the same time in order to reconstruct an image. Despite the name, EIT is also non-tomographic, in that slices cannot be reconstructed independently. Furthermore, EIT is severely ill-posed because small errors in the measurements can produce large errors in the reconstructed image (see section 2.2.2). From the mathematical point of

view, this makes EIT an interesting and challenging imaging problem.

The problem of determining the conditions under which the internal conductivity of an object can be uniquely determined from boundary voltage measurements was first studied by Calderón in 1980 [22] for the linearized problem (see section 2.4). In principle, if the boundary shape is known exactly, the current-to-voltage map depends uniquely on conductivity. Thus, the conductivity can be determined by full knowledge of the current-to-voltage map on the entire boundary. In practice, knowledge of the boundary is incomplete and uncertain, and the reconstruction depends strongly on modelling errors such as boundary geometry, electrode placement, size and shape, and contact impedance of the interface between the electrode and the skin.

Imaging a small and localized change in conductivity, which occurs over time, constitutes a relatively simple problem (see section 2.1.3.1). Two data sets are acquired at different time points and then subtracted. In this case, the relationship between conductivity and voltage changes is often modelled by a linearized model, and the conductivity change can be recovered by inverting the sensitivity map (see section 2.5.3). Producing one-shot static images without baseline measurements, is an exponentially more difficult problem. The first reason is that the data do not, in general, depend linearly on conductivity. Some attempts have been made to solve the full nonlinear problem and recover an image of the absolute conductivity values from a single data set (see sections 2.1.3.2 and 2.5.4) [62, 113]. However, a consequence of the problem being ill-posed is that it is much easier to image a *change* in conductivity, than its absolute value: when two data sets are subtracted, constant modelling or instrumentation errors are cancelled out, whereas if the absolute data is used, the reconstruction is more sensitive to errors. For this reason, the overwhelming majority of clinical EIT images have been produced using time-difference imaging.

The difficulty in imaging absolute conductivity has prompted researchers to investigate multifrequency methods for producing static images. Multifrequency EIT (MFEIT) involves varying the modulation frequency of the injected current, and acquiring two or more data sets at different frequencies (see section 2.6). The conductivity spectrum of biological tissues is dependent on histology; therefore it is possible to distinguish between tissues on the basis of their frequency response. Following the same logic of time-difference imaging, it seems natural to attempt to image a variation of conductivity across frequency: i.e. use a low frequency as reference and subtract two data sets acquired at different frequencies; then reconstruct an image by inverting the sensitivity

map calculated at the reference frequency. Unfortunately this approach is successful only in resolving a small, frequency dependent anomaly from a frequency independent, homogeneous background [97, 58, 3, 83]. The method has been extended to the case of a frequency dependent background by using a weighted difference between the data, but the range of applications remains severely limited. This technique is unsuitable for clinical application in that it does not accommodate for the complexity of human anatomy.

Initially developed for geophysical studies, EIT was first applied to clinical research in 1987 by the Sheffield University research group, led by Barber and Seagar in the Department of Medical Physics and Clinical Engineering at Royal Hallamshire Hospital. The Sheffield Mark 1 EIT system had a ring of 16 electrodes, and a single current source [17]. Using a multiplexer, current was injected and voltages were measured at adjacent pairs of electrodes. Most early clinical studies were made with the Sheffield Mark I, and many research groups still use systems based on this first example (see section 2.1.2) [72, 82, 26, 35]. The first algorithm for imaging conductivity changes in a 2D cross-section, the so-called "Sheffield algorithm", was based on a backprojection method [6]. The Sheffield group is also accredited with proposing to reference measurements taken at different frequencies against each other [16, 41]. Three-dimensional imaging methods and realistic electrode models were initially developed at the Rensselaer Polytechnic Institute [23, 104, 74], and statistical approaches to image reconstruction and regularization were pioneered by researchers at the Universities of Helsinki and Kuopio (now University of Eastern Finland) [111, 113, 59, 60]. Electrical Impedance and Diffuse Optical Reconstruction Software (EIDORS) is a freely available MATLAB toolbox for EIT imaging [86, 66] based on software developed at the Universities of Manchester and Kuopio [114, 112].

The benefits of EIT applications in medicine lie in the possibility of obtaining high temporal resolution, and in the portability and limited cost of the scanner. The main limitation is the low spatial resolution, which is due to the non-locality and high sensitivity of the reconstruction problem to modelling and experimental errors. EIT has been applied successfully in clinical studies to monitor dynamic body functions such as lung ventilation [74], gastric emptying [70] and the cardiac cycle [34]. Holder proposed EIT as a method for imaging neuronal depolarization [47] and localizing epileptic foci in the brain [48] (see section 2.1.4.2).

EIT is currently being investigated as a clinical diagnostic tool. The applications listed previously all involve imaging of a time series, and therefore time-difference methods

are used. In order to extend the application of EIT to diagnostic imaging, a method for producing static images is necessary. For example, it has been proposed to use MFEIT for breast cancer screening [69], lung imaging [41, 18], monitoring of brain injury in intensive care [99] and differentiating between stroke types in the ambulance (see section 2.1.4.1) [52, 92, 83]. The latter techniques all involve the differentiation of tissues on the basis of their characteristic impedance spectrum, therefore it is sufficient to acquire a single multifrequency dataset. However, MFEIT has received little attention in the literature and is at an earlier stage of development with respect to time-difference EIT. Due to the ill-posedness of the inverse problem, MFEIT imaging is highly sensitive to modelling errors and suffers from poor signal-to-noise ratio. The main challenge in this field is to develop an imaging approach with sufficient robustness to noise and model uncertainty for clinical application.

1.2 Purpose

The subject of this dissertation is the investigation of novel approaches to multifrequency EIT for diagnostic purposes, with a focus on brain imaging. The ultimate goal of this work is to provide a mathematical framework for static EIT imaging for a multitude of clinical applications. The use of multifrequency data and prior spectral information is explored as a means to improve the ill-posedness of the image reconstruction problem, and thus improve the outcome of the solution. The purpose is to provide an algorithm with sufficient robustness to experimental error and model uncertainty to be applied reliably to clinical data. The main contributions to the field are summarized as follows:

- The proposal of a novel method for performing MFEIT using explicit spectral constraints, the *fraction reconstruction method*.
- The analysis of the application of the newly developed method to stroke type differentiation in the presence of model uncertainty.
- The proposal of a novel simultaneous approach to image reconstruction and segmentation for MFEIT, the combined *reconstruction-classification method*.
- The proposal of a novel reconstruction-classification method for MFEIT based on graph-cut optimization, which allows for the inclusion of a spatial prior in the segmentation.

1.3 Structure

In the second chapter, a literature review of the relevant background is outlined. An introduction to EIT imaging, image reconstruction methods, multifrequency algorithms and image segmentation is described. In the third chapter, a novel method for performing multifrequency EIT using spectral constraints is formalized and discussed. The results of application to simulated and experimental phantom data are presented. In the fourth chapter, the application of EIT using spectral constraints to the problem of differentiating stroke types is discussed. Results of a numerical feasibility study using a realistic human head model are presented. In the fifth chapter, a novel combined reconstruction-classification method for estimating spectral constraints while simultaneously reconstructing conductivity is formalized, validated and tested on phantom data. In the sixth chapter, the reconstruction-classification method is formalized in the Bayesian framework, and graph cut optimization is applied to solving the problem of labelling the image per tissue type. In the seventh and final chapter, the conclusions to this work are discussed and the aims of future work are laid down.

1.4 Publications

The work presented in this thesis has been published in the following peer-reviewed journal papers:

Chapter 3

E. Malone, G. Sato dos Santos, D. Holder, S. Arridge. ‘*Multifrequency Electrical Impedance Tomography using spectral constraints*’, IEEE Transactions on Medical Imaging, 33(2), 340-350, October 2013, doi:10.1109/TMI.2013.2284966.

Chapter 4

E. Malone, M. Jehl, S. Arridge, T. Betcke, D. Holder. ‘*Stroke type differentiation using EIT: evaluation of feasibility in a realistic head model*’, Physiological Measurement, 35(6), 1051-66, May 2014, doi:10.1088/0967-3334/35/6/1051.

Chapter 5

E. Malone, G. Sato dos Santos, D. Holder, S. Arridge. ‘*A reconstruction-classification method for Multifrequency Electrical Impedance Tomography*’, IEEE Transactions on Medical Imaging, submitted April 2014.

The work in **chapter 3** is also covered by the following U.S. patent application:

E. Malone, D. Holder, S. Arridge, G. Sato dos Santos, ‘*Method and system for tomographic imaging*’, May 2012, US Patent 20130307566.

Chapter 2

Literature review

2.1 Introduction

2.1.1 Bioimpedance

The physical parameter that describes the basic electrical properties of biological tissue with regard to the flow of current is *impedance* [46]. In the absence of magnetic effects, impedance is dependant on resistance and capacitance. Resistance measures the extent to which tissue can oppose current flow within it, and capacitance measures the ability to retain and store electrical charge. Impedance is often substituted with its inverse, *admittivity*, to simplify notation.

The fundamental principle that allows different tissues to be distinguished using EIT is that the electrical properties of biological tissues depend on histology. The impedance of a cell was schematically modelled by Cole and Cole [25] as a parallel circuit containing a resistance R_e that represents the extracellular space, a resistance R_i that represent the intracellular space, and a capacitance C_m that represents the bi-lipid cell membrane (figure 2.1). The resulting impedance of the cell is

$$Z = \frac{R_i R_e + \frac{R_e}{i\omega C_m}}{R_i + R_e + \frac{1}{i\omega C_m}}. \quad (2.1)$$

The analogy arises from to the insulating properties of cell walls (figure 2.2). At low frequencies the current does not cross the membrane and flows mainly in the extracellular space, therefore the impedance is mainly resistive

$$\lim_{\omega \rightarrow 0} Z = R_e. \quad (2.2)$$

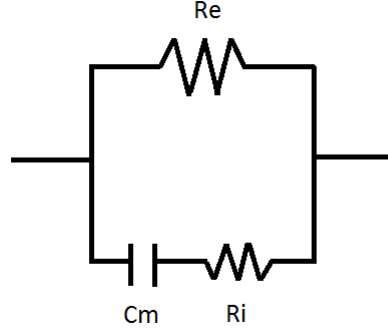


Figure 2.1: Cole-Cole model of electrical properties of a cell. R_e represents the extracellular space, R_i the intracellular space, and C_m the bi-lipid cell membrane.

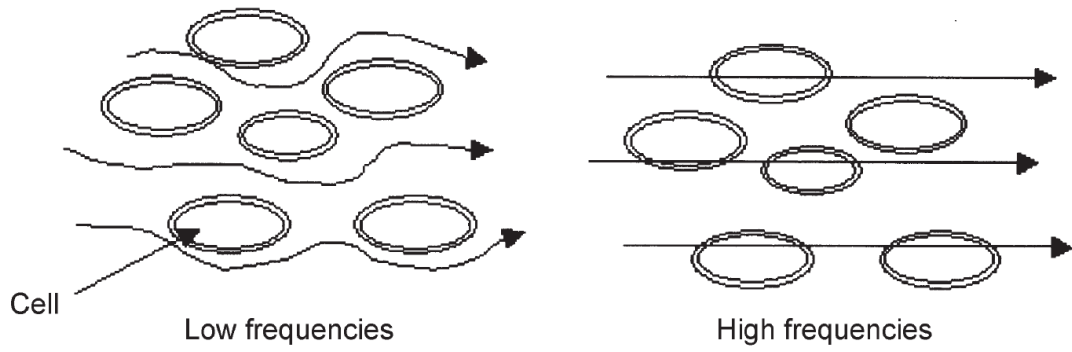


Figure 2.2: The movement of current through cells at low and high frequencies [46].

Similarly, at high frequencies the membrane never fully charges or discharges so

$$\lim_{\omega \rightarrow \infty} Z = R_i \parallel R_e, \quad (2.3)$$

where \parallel indicates resistances in parallel.

The physical parameter of interest in EIT is usually the real component of impedance, *resistance*. In the case of biological tissue, this is frequency dependent:

$$R(\omega) = \Re(Z) = \frac{R_i R_e (R_i + R_e) + \frac{R_e}{\omega^2 C_m^2}}{(R_i + R_e)^2 + \frac{1}{\omega^2 C_m^2}}. \quad (2.4)$$

Resistance increases with the length of the current flow path, and decreases with the cross-section. If measured at low frequencies, bodily fluids will have low resistance and dense tissues such as bone or fat will have high resistance. If expressed in terms of a volume density, resistance is known as resistivity ρ and its inverse as conductivity σ , which is measured in $\frac{S}{m}$. Ohm's law for a resistor-capacitor network

$$V = I \cdot Z \quad (2.5)$$

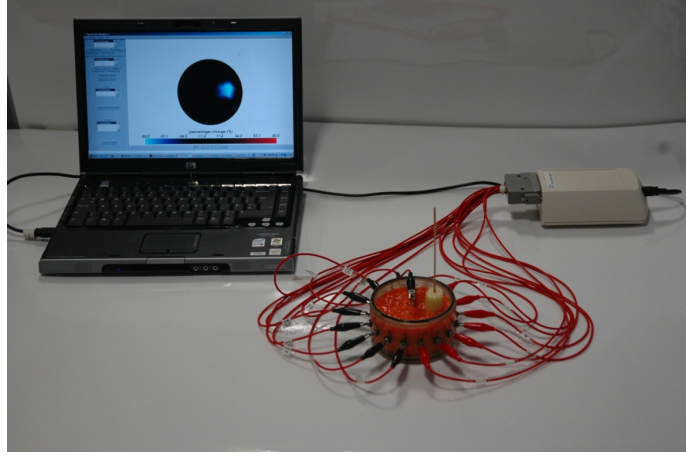


Figure 2.3: The UCL Mk 2.5 EIT system [72].

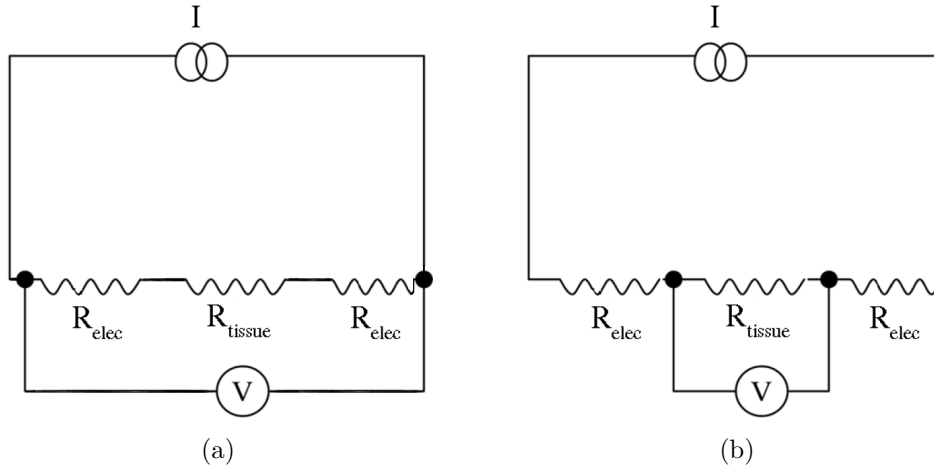


Figure 2.4: Diagram of the two-electrode (a) and four-electrode (b) measurement methods.

describes the relationship between injected current I , voltage V and impedance Z in a circuit. This suggests that the real component of tissue impedance can be estimated by injecting current and measuring the in-phase component of the resulting voltage.

2.1.2 EIT measurements

The essential components of an EIT system for clinical use are a high-precision current source, an array of electrodes, and a voltmeter (Figure 2.3).

The *current pattern* determines which electrodes are activated in driving the current, and the *measurement pattern* determines the voltage measurements acquired for each current pattern, which is determined by the spatial configuration of active electrodes. The first EIT system, the Sheffield Mk 1 developed in 1987, injected current at a single frequency (50 kHz) by use of a circular ring of electrodes. The current was driven through pairs of adjacent electrodes, and voltage measurements were acquired at all adjacent

pairs not involved in driving the current. The number of independent measurements for this configuration is $L(L - 3)$, where L is the number of electrodes. If the current is driven through electrodes $l - 1$ and l then the set of measurements is

$$\mathbf{v}_{(l-1,l)} = (V_1 - V_2, \dots, V_{l-3} - V_{l-2}, V_{l+1} - V_{l+2}, \dots, V_{L-1} - V_L), \quad (2.6)$$

where V_l is the voltage on the l th electrode referred to ground. This approach, commonly referred to as *adjacent* current pattern, is not optimal because very little current crosses the centre of the domain. In order to obtain better sensitivity in the centre, current can be applied at opposite electrodes. This approach is known as the *polar* current pattern. Given that the pattern is highly symmetrical, the number of independent measurements is limited to $L(L - 4)/2$. If the current is driven through electrodes l and $L/2 + l - 1$ then the set of measurements is

$$\begin{aligned} \mathbf{v}_{(l,L/2+l-1)} = & (V_1 - V_2, \dots, V_{l-2} - V_{l-1}, V_{l+1} - V_{l+2}, \dots, V_{L/2+l-1-2} - V_{L/2+l-1-1}, \\ & V_{L/2+l-1+1} - V_{L/2+l-1+2}, \dots, V_{L-1} - V_L). \end{aligned} \quad (2.7)$$

To increase the number of independent measurements, it has been suggested to break the symmetry and drive electrode that are "just off" opposite when using a circular ring of electrodes [2].

The *distinguishability* of an anomaly is defined as the L_2 -norm of the difference between the boundary voltages of an object including and not including the anomaly, respectively V^1 and V^0 [55]:

$$\|V^1 - V^0\|. \quad (2.8)$$

For rotationally symmetric geometries with a centred inclusion, the current pattern that reveals the largest change in the data after the insertion of an anomaly can be calculated analytically by maximizing the distinguishability. Thus, the best patterns are the eigenfunctions corresponding the maximum eigenvalues of the operator

$$\Lambda_1^{-1} - \Lambda_0^{-1}, \quad (2.9)$$

where Λ_σ^{-1} is the linear map such that $\Lambda_1^{-1}(j) = V^1$ and $\Lambda_0^{-1}(j) = V^0$, where j is the current at the boundary (for a formal definition of Λ_σ^{-1} see section 2.4, equation (2.32)). It is easily shown that for cylindrically symmetric objects, the optimal patterns are

	Dynamic	Static
Qualitative	Time-difference	Frequency-difference
Quantitative	(Absolute)	Absolute

Table 2.1: Table of EIT imaging modalities.

the spatial harmonics [55]. The optimum pattern can be computed on the continuous boundary, and approximated using discrete electrodes. The ACT3 system is an adaptive system that injects sinusoidal patters, which are progressively modified using a feedback loop to approximate the optimal current pattern for a generic 2D geometry [26].

The technical advancement necessary for adopting optimal current patterns is a multiple-inject current source. The EIT system must allow for the simultaneous addressing of all electrodes, both for injecting current and acquiring measurements. The disadvantage of multiple-inject current patterns is that the same electrodes used for injecting the current are involved in acquiring the voltage measurements. The *two-electrode* method (figure 2.4a) for injecting current and measuring voltages is more sensitive to variations in the contact impedance of the electrodes than the traditional *four-electrode* method (figure 2.4b). The reason for this is that the two-electrode method measures the object impedance plus the impedance of the driving electrodes, whereas the four-electrode method only measures the conductivity of the object [71]. In the two-electrode case, the contact impedance must be estimated empirically [72], or reconstructed analytically [116]. In the case that application of the optimal current pattern is crucial for obtaining sufficient contrast, it may be preferable to attempt to correct for the contact impedance in two-electrode measurements rather than to use sub-optimal four-electrode current patterns. However, multiple-inject current patterns are more susceptible to errors in the contact impedance and electrode shape [62]. In order to reduce the effect of the contact impedance, the latter can be reduced below an acceptable threshold by abrading the skin and applying conductive gel to the electrode-skin interface [71, 93, 62].

2.1.3 EIT imaging modalities

EIT imaging modalities are differentiated by the choice of data. EIT is either dynamic or static, qualitative or quantitative (see table 2.1).

2.1.3.1 Linearized time-difference EIT

In time-difference imaging, measurements acquired at time t are referred to a previous time point t_0 , and the difference data is considered

$$\Delta \mathbf{v}^{\text{TD}} = \mathbf{v}_t - \mathbf{v}_{t_0}. \quad (2.10)$$

Time-difference EIT allows for the imaging of small and localized variations in conductivity. If an assumption of linearity between changes in conductivity and voltage recordings is made, the image reconstruction problem can be solved by a relatively simple method. In order to interpret the data, it is sufficient to build the map at time t_0 of the sensitivity of the measurements to changes in the conductivity and to invert the map by some method. The result is a contrast image, of the change in conductivity over time, which provides qualitative information about the object. The advantage of time-difference imaging is that time-independent instrumentation or modelling errors, such as uncertainty in the geometry of the boundary and skin-electrode contact impedance, are partially subtracted from the data [71]. Therefore the imaging is highly robust to time-independent errors.

2.1.3.2 Absolute EIT

Absolute imaging aims to reconstruct quantitative conductivity values from an absolute data set v , acquired at a single time-point [62, 113]. The imaging problem is nonlinear and very difficult to solve. The result is a quantitative image of the absolute conductivity of the object. The advantage of absolute imaging is the potential to image an event without information regarding the condition prior to the onset, which is a requirement for diagnostic imaging. If repeated at multiple time points, absolute imaging can also be used to image a dynamic process. Although absolute EIT has been attempted by many research groups, high sensitivity to uncertainty in the physical model and instrumentation noise have so far prevented the production of satisfactory images from clinical data.

2.1.3.3 Frequency-difference EIT

In frequency-difference imaging, measurements acquired at modulation frequency ω , are referred to a lower frequency ω_0

$$\Delta \mathbf{v}^{\text{FD}} = \mathbf{v}_\omega - \mathbf{v}_{\omega_0}. \quad (2.11)$$

Frequency-difference EIT allows for the suppression of frequency-independent instrumentation and modelling errors. The result is a qualitative image of the state of the object at a single time-point; therefore frequency-difference is an alternative to absolute imaging for diagnostic purposes. The disadvantage with respect to absolute imaging is the lack of quantization, and the loss of absolute contrast between tissues. Linearisation around the reference frequency can only be used to resolve a small anomaly from a large homogeneous background [58, 83]. This is insufficient for most clinical applications, and nonlinear approaches must be pursued [51].

2.1.3.4 Multifrequency EIT

The term *multifrequency*, or spectroscopic, indicates any EIT modality which considers measurements acquired at multiple frequencies. Therefore frequency-difference EIT is inherently multifrequency. Time-difference and absolute EIT can also be multifrequency, if measurements acquired at different frequencies are considered simultaneously in reconstructing an image. In multifrequency mode, tissues are distinguished by their unique conductivity spectrum, in either absolute, frequency-difference, or time-difference terms.

2.1.4 EIT of the human head

The main focus of the EIT research group at UCL is the application of EIT to imaging functional and pathological brain function. There are currently two primary areas of interest: stroke type differentiation using EIT, and EIT of fast neural activity in the brain.

2.1.4.1 EIT of stroke

Stroke is the third most common cause of death and leading cause of disability in the UK. Haemorrhagic stroke is caused by bleeding in the brain and requires surgery for treatment. Ischaemic stroke is an interruption of blood flow in a region of the brain caused by a thrombosis or embolism. In 2003, a thrombolytic drug which relieves the occlusion and restores blood flow, recombinant tissue plasminogen activator (tPA), was licensed in the UK for treating ischaemic stroke. In order to be successful, "clot-busting" drugs must be administered within three hours of the onset of the stroke. However, an image of the brain must first confirm the type of stroke, as the drug may be damaging in the case of haemorrhage. The current procedure is to take a CT image, therefore treatment is delayed until the patient is transported to hospital and the scan is performed. Recent statistics show that in the UK, although about 80% of all strokes are ischemic,

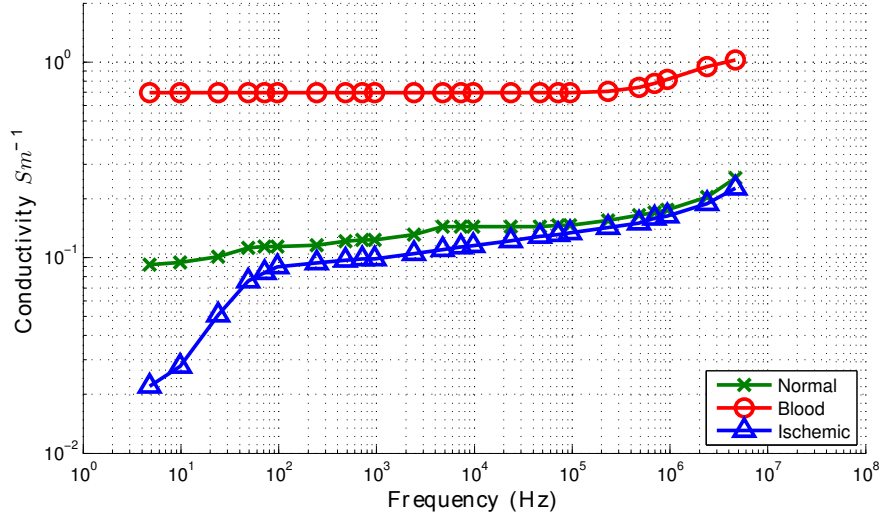


Figure 2.5: Conductivity spectrum of normal brain tissue, ischaemic brain tissue and blood, adapted from [52].

only 2.5-5% of these are identified and treated in time [87].

In the case of ischaemic stroke, cell swelling caused by energy failure results in an impedance increase. In the case of haemorrhagic stroke, increased blood volume results in higher conductivity (Figure 2.5). Preliminary studies suggest that EIT could be successful in differentiating between ischaemic and haemorrhagic stroke for the purpose of informing the course of treatment [52, 83]. Although EIT cannot compete with CT in terms of image quality, limited cost and portability could make EIT scanners immediately available in the ambulance or casualty department. Studies are currently being performed that investigate methods for fast application and localization of the electrodes in emergency situations. If successful, application of EIT to stroke imaging could result in fast administration of thrombolytic drugs and significantly improve the outcome of treatment.

Stroke type differentiation using scalp electrodes presents a series of modelling and technological challenges. Application of EIT to brain imaging is complicated by the presence of the scalp, skull and CSF. The highly resistive skull limits current flow in the centre of the head, and the highly conductive CSF surrounding the brain acts as an electrical shunt, diverting the current from the area of interest. These effects result in a low signal-to-noise ratio because the areas crossed by more current contribute more to the measurements. The amplitude of the injected current is limited by medical safety regulations, therefore the obtainable signal amplitude is also limited. Electrode positions must be measured accurately as deviations in the physical model may cause severe

artefacts in the reconstructed image. Furthermore, skin-to-electrode contact impedance is highly variable and difficult to account for in modelling, and therefore constitutes an unpredictable source of noise. This is especially a problem in the setting of acute stroke.

The imaging challenge of stroke EIT arises from the necessity to image the event without knowledge of a baseline condition. Patients are usually admitted into care after the onset of the stroke, therefore a baseline recording of the healthy brain is not available. Therefore it is not possible to solve the reconstruction problem using a simple linear method. One-shot, or absolute, imaging could potentially provide high contrast, but is highly sensitive to errors in the boundary geometry and electrode positions. Frequency-difference imaging would allow for the subtraction of modelling errors and, given the spectral properties of blood and ischaemic tissue, is suitable for stroke classification. However, a non-linear, large-scale inversion framework is therefore potentially required [51, 53].

2.1.4.2 EIT of fast neural activity

The aim of fast neural EIT is to image functional brain activity for research purposes. When a region of the brain is activated, energy is consumed, and an increase in oxygenation levels occurs that results in increased blood flow. Local impedance variations due to physiological activity fall into two main categories. Fast changes in impedance, which occur over milliseconds, are of the order of 0.01% and are caused by the opening of neural ion channels during depolarization. Slow changes, which occur over tens of seconds, are of the order of 10% and are due to blood flow and volume variations that result from the accumulation of depolarization activity [48]. The latter changes can be observed using, for example, PET or functional MRI, while the former changes can not.

Inverse source modelling using Electro-Encephalography (EEG) and, more recently, Magneto-Encephalography (MEG), have produced good results in localizing simple sources of activity near the surface of the brain. However, in the case of complex or deep sources, these methods are unsuccessful in producing unique solutions, and the accuracy of reconstructed images is doubtful. EIT holds a unique potential for providing large-scale 3D imaging of the transmission of electric signals in the brain, which may shed light on many unanswered questions in the field of neuroscience.

Another possible application of this technique, which is currently under investigation, is the localization of seizure sources during preoperative assessment of epileptic patients. EIT of epilepsy could improve accuracy in localizing epileptic foci, thus reducing the invasiveness and risks of surgery, and increasing the number of patients suitable for

surgery.

2.1.4.3 Conductivity of tissues in the head

The study of the dielectric spectra of biological tissues is of prime importance to impedance imaging. Many studies have been performed that investigate the theoretical aspects of bioimpedance and present corroborative measurement data. The dielectric spectra of different tissues are shown to have similar properties: resistivity decreases at high frequencies in three main steps known as α , β and γ dispersion. The β dispersion, in the region of hundreds of kHz, is described by the Cole-Cole model (2.1): an increase in conductivity is caused by the polarization of cell membranes allowing current to flow in the intracellular space. The α dispersion occurs at lower frequencies and is due to ionic diffusion at the cell membrane. Finally, the γ dispersion is associated with the polarization of water molecules in the tissue, and occurs at very high frequencies (~ 10 GHz) [46].

2.1.4.4 Skin

Skin impedance measurements are highly relevant to the design of impedance tomography systems and electrode application techniques. Variations in skin impedance are difficult to model and may produce severe artefacts in reconstructed images. Rossel *et al.* [93] measured skin impedance on 10 volunteers in 10 different locations, including the forehead. Gel was used to apply the electrodes but, in order to simulate worst-case application conditions, no cleaning or abrasion of the skin was performed. The results show that skin impedance can be modelled by a 3 element equivalent circuit of a resistance in series with a resistor-capacitor parallel. At high frequencies the resistance is similar for each location, whereas at lower frequencies there is a wider spread. This suggests that the in-series resistor can be fixed at approximately 120Ω . The capacitance of the barrier layer of the skin is modelled by a 10-40 nF capacitor, while the in-parallel resistance varies across different locations. The latter can be significantly reduced by abrading the skin before applying the electrodes.

2.1.4.5 Skull

Several studies have shown that the resistivity of the skull is between 15 and 80 times higher than the resistivity of the brain. For this reason, accurate representation of skull resistivity is crucial to impedance imaging. Tang *et al.* [108] measured the resistivity of 388 skull samples obtained from patients undergoing surgery in the range 1 Hz — 4 MHz. The study revealed that the resistivity of the skull is non-homogeneous and

inversely dependent on frequency. The samples were classified into 6 categories according to structural variations such as sutures (fibrous joint), diploe (spongy interior tissue), and joints. Skull resistivity is strongly influenced by structural variations, with standard compact skull having the highest resistivity ($26546 \pm 5374 \Omega \cdot \text{m}$), and squamous suture skull (joint between the parietal and temporal bones) the lowest ($12747 \pm 4120 \Omega \cdot \text{m}$). The spectra of samples with different structures were shown to have a similar trend. The resistivity is approximately constant up to 10 kHz and then decreases. In a subsequent study [107] the authors defined the characteristic parameters for modelling the resistivity of each skull tissue type in the range 30 Hz — 3 MHz.

2.1.4.6 Blood

Gabriel *et al.* [37] performed a literature review of tissue dielectric properties. The survey revealed consistency between measured resistivity values of blood obtained from different species. The conductivity spectrum is relatively flat up to 100 kHz, and then increases significantly. Zhao [122] measured human blood samples at low frequencies and considered the effect of temperature and haematocrit (cell count) levels. Further studies are necessary to determine the conductivity of blood flowing in the body at 37° for reasonable haematocrit levels.

2.1.4.7 Grey and white matter

Latikka *et al.* [64] made *in vivo* measurements in patients undergoing brain surgery. They recorded a conductivity of 0.28 S/m for grey matter and 0.25 S/m for white matter. White matter is highly anisotropic in that it is formed of nerve fibres, and is consequently difficult to model because the conductivity depends on the direction of flow of the current. Nicholson [78] reported a factor of 9-10 times between the longitudinal and transverse conductivity. Similar anisotropic properties were found in the cerebellum of frogs and toads by Nicholson and Freeman [77]. For a recent review see [38] and references.

2.1.4.8 Cerebral spinal fluid

Cerebral spinal fluid (CSF) occupies the ventricles and a thin layer surrounding the whole brain. It presents a very low cell concentration, therefore its conductivity is approximately constant across frequencies and relatively high with respect to the other tissues of the head. Application of EIT to brain imaging is complicated by the presence of the CSF because the high contrast in conductivity causes a shunting effect that reduces the current injected into the brain, and therefore the sensitivity of boundary

measurements to changes in conductivity. For this reason accurate modelling of the CSF is necessary. Ranck and BeMent [91] recorded low frequencies measurements in cats and found the conductivity of the CSF to be approximately 1.67 S/m. Latikka *et al.* [64] reported a conductivity of 1.25 S/m at 50 kHz.

2.2 Image reconstruction principles

2.2.1 Introduction

Image reconstruction is defined as the process of mapping the distribution of a parametrised property of an object from measured data. In Bayesian inversion, the likelihood of obtaining measurements \mathbf{y} given a parameter \mathbf{x} is described by the *likelihood* distribution $p(\mathbf{y}|\mathbf{x})$. Otherwise, given the measurements \mathbf{y} , the resulting probability of the variable \mathbf{x} is

$$p(\mathbf{x}|\mathbf{y}) = \frac{p(\mathbf{y}|\mathbf{x})p(\mathbf{x})}{p(\mathbf{y})} \propto p(\mathbf{y}|\mathbf{x})p(\mathbf{x}), \quad (2.12)$$

where $p(\mathbf{x})$ and $p(\mathbf{y})$ are the prior distributions of the variable and data, respectively. The maximum-a-posteriori (MAP) estimate of \mathbf{x} is obtained by maximizing

$$\begin{aligned} \mathbf{x} &= \arg \max_{\mathbf{x}} p(\mathbf{y}|\mathbf{x})p(\mathbf{x}) \\ &= \arg \min_{\mathbf{x}} \mathcal{L}(\mathbf{x}, \mathbf{y}) + \tau\Psi(\mathbf{x}), \end{aligned} \quad (2.13)$$

where $\mathcal{L}(\mathbf{x}, \mathbf{y}) = -\log p(\mathbf{y}|\mathbf{x})$ is the negative log-likelihood, and $\tau\Psi(\mathbf{x}) = -\log p(\mathbf{x})$ is the negative log of the prior.

In order to determine $\mathcal{L}(\mathbf{x}, \mathbf{y})$, knowledge of how the measured data depends on the object parameters is necessary. This relationship is described by the *forward* function $A : S_x \rightarrow S_y$, which maps the parameter space S_x into the measurement space S_y . The forward map is essentially a description of the physical process that causes certain measurements \mathbf{y} for an object with properties given by \mathbf{x} . The forward map is dependent on the geometry and state of the object, which are represented by a model. In practice, experimental measurements are affected by noise, therefore the measured data is given by

$$\hat{\mathbf{y}} = A(\mathbf{x}) + \mathbf{h}, \quad (2.14)$$

where \mathbf{h} is random noise. Given that \mathbf{x} and \mathbf{h} are independent, the likelihood of \mathbf{y} given \mathbf{x} is

$$p(\mathbf{y}|\mathbf{x}) = p(A(\mathbf{x}) - \mathbf{y}) \quad (2.15)$$

If the noise \mathbf{h} is drawn from a multivariate Gaussian distribution with covariance Σ_h and zero mean, then the negative log-likelihood of the data is

$$\mathcal{L}(\mathbf{x}, \mathbf{y}) = -\frac{1}{2} \|A(\mathbf{x}) - \mathbf{y}\|_{\Sigma_h^{-1}}^2, \quad (2.16)$$

where $\|\cdot\|$ indicates the L^2 -norm. Finally, an *image* of the parameter \mathbf{x} is obtained by minimizing

$$\hat{\mathbf{x}} = \arg \min_{\mathbf{x}} \frac{1}{2} \|A(\mathbf{x}) - \mathbf{y}\|_{\Sigma_h^{-1}}^2 + \tau \Psi(\mathbf{x}), \quad (2.17)$$

where the regularization parameter τ , balances the confidence in the data with the confidence in the prior.

2.2.2 Ill-posedness

It has been shown that a successful outcome to the imaging problem is possible under the *Hadamard conditions of well posedness* [67]:

1. A solution exists for every set of measured data
2. The solution is unique for every set of measured data
3. The solution depends continuously on the measured data.

Under these conditions the equation $A(\mathbf{x}) = \mathbf{y}$ is solvable for \mathbf{x} . Otherwise, if any of the three Hadamard conditions is violated, the problem is ill-posed, and the equation has either none, or infinite, or unstable solutions.

The imaging problem of EIT, which consists in recovering conductivity from boundary voltage measurements, is severely ill-posed. The most problematic is the third condition: for measurements of any precision, an undetectable anomaly of arbitrary amplitude can be produced [55]. The solution is exponentially unstable, therefore small changes in the data can cause large changes in the reconstructed image. Furthermore, experimental measurements are limited in number and precision, so the second condition is also violated. In order to find an approximate solution, the ill posed problem must be converted into a different, well-posed problem through regularization and incorporation of sufficient *a priori* information. This information is encoded by the prior probability distribution of the variable $p(\mathbf{x})$, which determines the regularization term $\tau \Psi(\mathbf{x}) = -\log p(\mathbf{x})$.

In the following, the case of isotropic distributions is considered. Isotropy requires the assumption that the physical property of interest in the imaging problem is independent of direction. In the case of EIT, this is equivalent to assuming that the conductivity

is independent of the direction of flow of the current. For recent results on recovering anisotropic conductivity in the head see [1].

2.3 Mathematical problem definition of EIT

Let us consider a three-dimensional domain Ω with a smooth boundary $\partial\Omega$, on which a position-dependent admittivity distribution $\gamma(\mathbf{x}, \omega) = \sigma(\mathbf{x}) + i\omega\epsilon(\mathbf{x})$ is defined, where σ is the conductivity and ϵ is the permittivity of the medium. The symbol $\mathbf{x} \in \mathbb{R}^3$ now indicates position in three dimensions. The injection of a current through the boundary generates an electric field $\mathbf{E}(\mathbf{x})$ that satisfies $\mathbf{J}_c = \sigma\mathbf{E}$, where $\mathbf{J}_c(\mathbf{x})$ is the conduction current density.

The electric displacement $\mathbf{D} = \epsilon\mathbf{E}$ and magnetic flux $\mathbf{H} = \frac{\mathbf{B}}{\nu}$, where $\mathbf{B}(\mathbf{x})$ is the magnetic field and ν is the magnetic permeability, are determined by the complete Maxwell equations:

$$\nabla \cdot \mathbf{D} = \rho \quad (2.18)$$

$$\nabla \cdot \mathbf{H} = 0 \quad (2.19)$$

$$\nabla \wedge \mathbf{E} = -\frac{\partial \mathbf{B}}{\partial t} \quad (2.20)$$

$$\nabla \wedge \mathbf{H} = \mathbf{J} + \frac{\partial \mathbf{D}}{\partial t} \quad (2.21)$$

where ρ is resistivity and $\mathbf{J} = \mathbf{J}_c + \mathbf{J}_s$ is the sum of the conduction and source current densities. Taking the gradient of equation (2.21) and using (2.18) yields the charge conservation law

$$\nabla \cdot \mathbf{J} = -\frac{\partial \rho}{\partial t} \quad (2.22)$$

that relates changes in current flow through a closed surface $\partial\Omega$ to the presence of current sources within the enclosed volume Ω . If the total internal charge $Q = \int_{\Omega} \rho$ is constant, then $\mathbf{J}_s = 0$ and equation (2.22) becomes

$$\nabla \cdot \mathbf{J} = 0 \quad (2.23)$$

that is the continuum of Kirchoff's law in the absence of current sources.

Solving the EIT forward problem for a generic geometry requires the simplifying assumption that the magnetic field is negligible. This choice is justified by the use of low frequency currents in EIT imaging. An evaluation of the error committed by employing the quasi-static model rather than the full-Maxwell model in high-frequency EIT is

provided in [105, 19]. The approximation is good in the range 3—100 kHz, but the error increases sharply above 100 kHz. This suggests that for very high frequencies it may be desirable to attempt to solve the full Maxwell equations.

Under the *quasi-static* approximation we have that $\nabla \wedge \mathbf{E} = 0$ (equation (2.20)) and the electric field can be expressed on a simply-connected domain as $\mathbf{E} = -\nabla u$, where $u(\mathbf{x})$ is a scalar potential field. The current density \mathbf{J} is thus obtained in function of the potential u

$$\mathbf{J} = \sigma \mathbf{E} = -\sigma \nabla u \quad (2.24)$$

that is the continuum of Ohm's law under quasi-static approximation.

Substituting equation (2.24) into equation (2.23) delivers

$$\nabla \cdot (\sigma \nabla u) = 0 \quad (2.25)$$

that is the generalized Laplace equation. This last equation provides the basis for producing EIT images: it states that, in the absence of current sources, the tendency of charge to flow in or out of a spot \mathbf{x} is zero [23]. The problem is clearly non-linear as the two unknown functions $\sigma(\mathbf{x})$ and $u(\mathbf{x})$ are multiplied together.

The current density at the boundary $\delta\Omega$ is

$$j = -\mathbf{J} \cdot \mathbf{n} = -\sigma \nabla u \cdot \mathbf{n} \quad (2.26)$$

where \mathbf{n} is the outward normal unit vector.

In practice, EIT systems use time-harmonic injection currents of fixed frequency $I = I_0 \sin(\omega t)$. A single sinusoid is optimal for obtaining good signal to noise within the safety constraints of medical applications, which limit the amplitude of the injected current. It is possible to reduce the acquisition time by injecting multiple frequencies simultaneously at the cost of added complexity in the instrumentation, and a reduction in the signal amplitude. The electric field, current distribution and electric potential are time dependent and vary with the same frequency ω . Furthermore, in the case of biological tissue, the conductivity $\sigma(\omega)$ and permittivity $\epsilon(\omega)$ are frequency dependent. Expressing the electric field as

$$\mathbf{E}(\mathbf{x}, t) = \Re(\mathbf{E}(\mathbf{x}) \exp(i\omega t)), \quad (2.27)$$

where $\mathbf{E}(\mathbf{x})$ is a complex phaser and \Re indicates the real component, and substituting

in (2.20) and (2.21) yields the time harmonic Maxwell equations

$$\nabla \wedge \mathbf{E} = -i\omega\nu\mathbf{H} \quad (2.28)$$

$$\nabla \wedge \mathbf{H} = \mathbf{J} + i\omega\epsilon\mathbf{E} \quad (2.29)$$

Given that $\mathbf{J}_c = \sigma\mathbf{E}$, $\mathbf{J}_s = 0$ and $\mathbf{E} = -\nabla u$, (2.29) can be rewritten as

$$\nabla \wedge \mathbf{H} = (\sigma + i\omega\epsilon)\mathbf{E} = \gamma\mathbf{E} = -\gamma\nabla u \quad (2.30)$$

where $\gamma = \sigma + i\omega\epsilon$ is the complex admittivity distribution. Applying the gradient function and using $\nabla \cdot (\nabla \wedge (-)) = 0$ gives

$$\nabla \cdot (\gamma\nabla u) = 0 \quad (2.31)$$

that is the same as (2.25) but for admittivity rather than conductivity.

2.4 Forward problem

The forward problem consists in determining the potential $u(\mathbf{x})$ from knowledge of the conductivity distribution $\sigma(\mathbf{x})$ and the Neumann boundary conditions. The forward map $A : S_\sigma \rightarrow S_v$ reveals how object parameters relate to acquired measurements. In 1980, Calderon [22] proposed the inverse problem of uniquely determining the conductivity distribution $\sigma(\mathbf{x})$ defined on a bounded domain Ω , from knowledge of the Dirichlet-to-Neumann (DtN) boundary conditions operator, defined as

$$\Lambda_\sigma : u \rightarrow \sigma \frac{\partial u}{\partial n} \quad \text{for } u \in \partial\Omega, \quad (2.32)$$

where $\frac{\partial u}{\partial n} = \nabla u \cdot \mathbf{n}$ and \mathbf{n} is normal to the boundary $\partial\Omega$. Solving the forward problem is equivalent to determining the DtN map for an assumed physical model because all the information necessary for recovering σ by applying a voltage and measuring current must be included in Λ_σ . In practice, EIT uses the Neumann-to-Dirichlet (NtD) map Λ_σ^{-1} because it is easier to apply current and measure voltage, and also the NtD map is an integrating function, therefore it is more stable than the derivating DtN map. Accurate representation of the object and of the experimental setup in the forward model are crucial: modelling errors such as incorrect boundary geometry, electrode contact impedance, or electrode positions and shape can severely reduce image quality.

2.4.1 Weak formulation

The mathematical formulation of the generalized Laplace equation (2.25) requires for $u(\mathbf{x})$ to be twice differentiable with respect to the spatial variable \mathbf{x} ($u \in \mathbb{C}^2$). Furthermore, for a solution to exist and be unique, the boundary $\partial\Omega$ must be Lipschitz continuous [76, 84]. These conditions are too strong for realistic physiological models as they are only verified by simple geometries. Extension of the forward solution to piecewise analytic conductivities requires a weak formulation of the problem [61]. This is obtained by assuming that, given a test function v ,

$$\int_{\Omega} v \nabla \cdot (\sigma \nabla u) = 0, \quad (2.33)$$

therefore

$$\int_{\Omega} \nabla v \cdot (\sigma \nabla u) = \int_{\partial\Omega} v \sigma \frac{\partial u}{\partial n}, \quad (2.34)$$

which is the weak formulation of the generalized Laplace equation. If $v = u$ is considered, then the weak formulation implies that

$$\int_{\Omega} \sigma |\nabla u|^2 < \infty, \quad (2.35)$$

which is a reasonable physical assumption as it implies that power dissipation is finite. The integral is null for $\nabla u = 0$, which means that the Dirichlet-to-Neumann map has a non-trivial kernel containing all constant potential distributions. Provided that the conductivity is bounded, the weak formulation requires that the square integrals of u and ∇u are finite. Therefore the solution u belongs to the $H^1(\Omega)$ Hilbert space. As a consequence, the Dirichlet conditions belong to $H^{1/2}(\partial\Omega)$ and the Neumann conditions to $H^{-1/2}(\partial\Omega)$. The weak formulation of the generalized Laplace equation with Dirichlet boundary conditions has a unique solution. In the case of known Neumann boundary conditions, as in EIT, the solution is unique up to a constant, which is determined by choosing a ground point. For a review of uniqueness and stability results see [8].

2.4.2 Numerical methods

An analytical solution to the forward problem is obtained only in the case of simple or highly symmetric geometries, otherwise it is necessary to pursue numerical methods. The *finite element method* (FEM) is employed to solve the forward problem for a generic geometry with arbitrary conductivity. Under the FEM, the domain is discretized into a finite number of irregular polyhedra, and the solution is approximated within each

element by a polynomial of fixed order. The FE forward model consists in an opportune segmentation of the whole domain, or mesh, and conductivity values for each element. The value of the potential function u on each node is calculated by solving a system of M equations, where M is the number of nodes. The final solution $u(\mathbf{x})$ is searched in a M -dimensional discrete sub-space of the H^1 Sobolev space by interpolating the values calculated on each node according to the polynomial basis of the elements. For this reason, the solution is piecewise polynomial. Other numerical solutions such as Finite Differences [85], which employs a regular rectangular mesh, and Boundary Element Method [31], which involves segmenting only the boundary, have been used in the case of simple geometries and homogeneous media, respectively.

2.4.3 Mesh generation

Mesh generation is a complex problem that constitutes a self standing field of research. The three factors involved in the creation of a mesh are the type of partition, the degree of the polynomial approximation of the solution on each element, and the mesh density. The approximated solution converges to the real (weak) solution as the number of elements or the degree of the polynomial increases. The elements must cover the whole boundary and not intersect, so that the vertices of neighbouring elements coincide.

The tetrahedron is the most common shape employed in 3D EIT meshing as it allows for a linear approximation of the solution. Element size and density can be varied within the mesh in order to optimize the trade-off between accuracy and computational time. In EIT, elements that are crossed by the most current have higher sensitivity, therefore it is convenient that elements nearer the electrodes be smaller than elements in the centre of the domain.

The first mesh used in head EIT imaging was a homogeneous sphere [109], followed by a multi-layer sphere [68]. Patient specific meshes have been created by segmenting MRI or CT images [7, 110, 117] of the area of interest. Several such studies suggested that the use of more accurate anatomical meshes would improve the imaging results [5, 62, 119]. In the case of stroke type-differentiation, patient specific meshes would be unavailable in emergency situations. One alternative option may be to select a head model from a library and warp the boundary according to accurately measured electrode positions to approximate the real shape.

2.4.4 Electrode model

An accurate model of the current distribution at the boundary, which determines the Neumann boundary conditions, is crucial in obtaining sufficient reconstruction quality. The positions of the electrodes are carefully measured in the experimental setup and are included in the forward model. It remains to choose a model for the current at the electrodes and elsewhere.

The most simple electrode model is the *gap model*, which assumes that the current density is constant on the driving electrodes and null elsewhere. The *gap shunt model* was developed to account for the fact that, although the total current injected at each electrode I_l is constant, the current density may vary in such a way that

$$\int_{E_l} \sigma \frac{\partial u}{\partial n} dn = I_l, \quad (2.36)$$

where E_l is the l th electrode for $l = 1, \dots, L$.

Under the *complete electrode model* (CEM) [104], a contact impedance z_l is introduced to account for the voltage drop between the skin and the electrode. The boundary voltage on the measurement electrode V_l is constant, and

$$\left\{ \begin{array}{ll} \left(u + z_l \sigma \frac{\partial u}{\partial n} \right) \Big|_{E_l} = V_l & \text{on } \partial\Omega, \\ \sum I_l = 0 & \text{absence of current sources,} \\ \sum V_l = 0 & \text{ground selection.} \end{array} \right. \quad (2.37)$$

The CEM has been shown to have a unique solution and to fit experimental data with an error of less than 0.1%, which is less than the previous models. Although not physically accurate, contact impedance is generally assumed to be constant on each electrode, so that integrating the CEM (2.37) with the weak problem formulation (2.34) yields

$$\int_{\Omega} \nabla v \cdot (\sigma \nabla u) = \sum_{l=1}^L \frac{1}{z_l} \int_{E_l} v (V_l - u), \quad (2.38)$$

where $\frac{1}{z_l}$ has been taken out of the integral. Choosing $v = u$ gives

$$\int_{\Omega} \sigma |\nabla u|^2 + \sum_{l=1}^L \int_{E_l} z_l \left(\sigma \frac{\partial u}{\partial n} \right)^2 = \sum_{l=1}^L V_l I_l, \quad (2.39)$$

which implies that power is either dissipated within the domain or the electrode contacts.

2.4.5 Galerkin FEM formulation

In the FEM formulation, the solution for u is approximated by a discrete interpolation of the values calculated for each node in the mesh. If the nodes are ordered and labelled using an index $j = 1, \dots, M$ then u can be expressed as

$$u = \sum_{j=1}^M u_j \phi_j. \quad (2.40)$$

Choosing linear basis functions, ϕ_j is 1 on the j th node, linear on the neighbouring elements, and 0 elsewhere

$$\phi_j = \begin{cases} 1 & \text{on the node } j; \\ 0 & \text{on all other nodes.} \end{cases} \quad (2.41)$$

In the Galerkin formulation, the system of M equations that determines the value of u at each node is obtained by substituting each of the basis functions into the weak problem formulation. Using ϕ_i , where $i = 1, \dots, M$, as test function and replacing u with the expression (2.40) in the weak equation yields the i th condition:

$$\sum_{j=1}^M u_j \int_{\Omega} \nabla \phi_i \cdot (\sigma \nabla \phi_j) = \sum_{l=1}^L \frac{1}{z_l} \int_{E_l} \phi_i (V_l - \sum_{j=1}^M u_j \phi_j). \quad (2.42)$$

Rearranging the common terms delivers

$$\sum_{j=1}^M u_j \left(\underbrace{\int_{\Omega} \nabla \phi_i \cdot (\sigma \nabla \phi_j)}_{\mathbf{A}_{ij}^U} + \underbrace{\sum_{l=1}^L \frac{1}{z_l} \int_{E_l} \phi_i \phi_j}_{\mathbf{A}_{ij}^Z} \right) + \sum_{l=1}^L V_l \left(\underbrace{-\frac{1}{z_l} \int_{E_l} \phi_i}_{\mathbf{A}_{il}^W} \right) = 0, \quad (2.43)$$

where \mathbf{A}^U is a symmetric $M \times M$ system matrix for the generalized Laplace equation, \mathbf{A}^Z is a $M \times M$ matrix that sets the Neumann boundary conditions, and \mathbf{A}^W is a $M \times L$ matrix that constrains the electrode voltages to $V_l \forall l = 1, \dots, L$.

If the conductivity is chosen to be piecewise constant, then it can be expressed as

$$\sigma(\mathbf{x}) = \sum_{n=1}^N \sigma_n \varphi_n \quad (2.44)$$

where φ_n is the constant basis function of the n th element, defined as

$$\varphi_n = \begin{cases} 1 & \text{on the } n\text{th element;} \\ 0 & \text{elsewhere.} \end{cases} \quad (2.45)$$

Substitution of (2.44) into the definition of \mathbf{A}^U delivers

$$\mathbf{A}_{ij}^U = \sum_{n=1}^N \sigma_n \int_{\Omega_n} \nabla \phi_i \cdot \nabla(\phi_j), \quad (2.46)$$

where the integral is constant for a given mesh and can be calculated off-line.

Using the CEM (2.37) and substituting expression (2.40) in the definition of the total current I_l applied to the l th electrode (2.36), yields

$$I_l = \frac{1}{z_l} \int_{E_l} V_l - u = V_l \underbrace{\frac{|E_l|}{z_l}}_{\mathbf{A}_{ll}^D} + \sum_{j=1}^M u_j \underbrace{\left(-\frac{1}{z_l} \int_{E_l} \phi_j \right)}_{\mathbf{A}_{lj}^W}, \quad (2.47)$$

where \mathbf{A}^D is a $L \times L$ matrix and $|E_l|$ is the area of the l th electrode. Combining the definition of I_l (2.36) with the equation for u (2.40) delivers a compact formulation of the forward problem in terms of the matrices defined above

$$\begin{pmatrix} \mathbf{A}_U + \mathbf{A}_Z & \mathbf{A}_W \\ \mathbf{A}_W^T & \mathbf{A}_D \end{pmatrix} \cdot \begin{pmatrix} \mathbf{u} \\ \mathbf{V} \end{pmatrix} = \begin{pmatrix} \mathbf{0} \\ \mathbf{I} \end{pmatrix}, \quad (2.48)$$

where $\mathbf{u} = (u_1, \dots, u_M)$ is the vector of values of u on the nodes, $\mathbf{V} = (V_1, \dots, V_L)$ and $\mathbf{I} = (I_1, \dots, I_L)$. Equation (2.48) can be further reduced by defining $\tilde{\mathbf{A}}$ so that

$$\tilde{\mathbf{A}} \tilde{\mathbf{u}} = \tilde{\mathbf{I}}, \quad (2.49)$$

where $\tilde{\mathbf{u}} = (\mathbf{u} \ \mathbf{V})$ and $\tilde{\mathbf{I}} = (\mathbf{0} \ \mathbf{I})$.

The final result is obtained by solving simultaneously for all P injection patterns in the measurements protocol $\mathbf{I}_1, \dots, \mathbf{I}_P$

$$\tilde{\mathbf{A}}(\tilde{\mathbf{u}}_1, \dots, \tilde{\mathbf{u}}_P) = (\tilde{\mathbf{I}}_1, \dots, \tilde{\mathbf{I}}_P). \quad (2.50)$$

Equation (2.50) is known as the *forward problem*. A solution is found using a linear

solver such as LU-factorization [40], generalized minimal residuals (GMRes) [95], or conjugate gradients (CG) [98]. For each current injection pattern the difference in boundary voltages between C combinations of electrode pairs $(l_{1c}, l_{2c}) \forall c = 1, \dots, C$ is considered. The result of the forward map is

$$\mathbf{v} = (V_{l_{11}} - V_{l_{21}}, \dots, V_{l_{1c}} - V_{l_{2c}}, \dots, V_{l_{1C}} - V_{l_{2C}}), \quad (2.51)$$

where \mathbf{v} has dimensions $1 \times PC$. Note that \mathbf{v} is independent of the choice of ground. In practice, the ground is set by adding a further electrode, which is connected to ground.

2.4.6 Sensitivity matrix

The sensitivity matrix, or Jacobian, defines the relationship between a change in the k th measurement v_k and a change in the conductivity of the n th element σ_n . The Jacobian coincides with the matrix of first derivatives of the forward map $A : S_\sigma \rightarrow S_v$

$$\mathbf{J}_{kn} = \frac{\partial v_k}{\partial \sigma_n}. \quad (2.52)$$

The Jacobian can be calculated up to a first order approximation by considering the perturbations $\sigma \rightarrow \sigma + \delta\sigma$, $u \rightarrow u + \delta u$, and $V_l \rightarrow V_l + \delta V_l$, with the currents I_l held constant [86]. Substituting in the equation for power conservation (2.39) and ignoring the second order terms gives

$$\int_{\Omega} \delta\sigma |\nabla u|^2 + 2 \int_{\Omega} \sigma \nabla u \cdot \nabla \delta u + 2 \sum_{l=1}^L \int_{E_L} z_l \left(\sigma \frac{\partial u}{\partial n} \right) \delta \left(\sigma \frac{\partial u}{\partial n} \right) = \sum_{l=1}^L I_l \delta V_l. \quad (2.53)$$

Using the weak formulation (2.34) with $v = \delta u$ yields

$$\int_{\Omega} \sigma \nabla u \cdot \nabla \delta u = \int_{\partial\Omega} \delta u \sigma \frac{\partial u}{\partial n}, \quad (2.54)$$

and using the CEM (2.37) on the l th electrode delivers

$$\delta \left(\sigma \frac{\partial u}{\partial n} \right) = \frac{1}{z_l} (\delta V_l - \delta u). \quad (2.55)$$

Therefore equation (2.53) becomes the power perturbation formula

$$\sum_{l=1}^L I_l \delta V_l = - \int_{\Omega} \delta\sigma |\nabla u|^2, \quad (2.56)$$

which defines the total change in power. In order to obtain the change of the q th

electrode combination (l_{1q}, l_{2q}) for the injection pattern \mathbf{I}_p ,

$$\delta v_k = \delta V_{l_{1q}} - \delta V_{l_{2q}} \quad (2.57)$$

where $k = 1, \dots, K$ ($K = PQ$) accounts for both the injection pattern index p and measurement pair index q , the hypothetical measurement current is defined as

$$\mathbf{I}_q = \begin{cases} 1 & \text{on } E_{l_{1q}} \\ -1 & \text{on } E_{l_{2q}} \\ 0 & \text{elsewhere.} \end{cases} \quad (2.58)$$

Equation (2.56) is solved for $u(\mathbf{I}_p) + u(\mathbf{I}_q)$ and $u(\mathbf{I}_p) - u(\mathbf{I}_q)$, where $u(\mathbf{I}_p)$ is the real field generated by the injection pattern \mathbf{I}_p and $u(\mathbf{I}_q)$ is the fictional measurement field. Subtracting the results yields

$$\delta v_k = - \int_{\Omega} \delta \sigma \nabla u(\mathbf{I}_p) \cdot \nabla u(\mathbf{I}_q), \quad (2.59)$$

which is the Fréchet derivative of the measured voltages. Choosing the discretization of the conductivity distribution (2.44) gives the expression

$$\frac{\partial v_k}{\partial \sigma_n} = - \int_{\Omega_n} \nabla u(\mathbf{I}_p) \cdot \nabla u(\mathbf{I}_q), \quad (2.60)$$

which defines the elements of the Jacobian (2.52). The potential fields $u(\mathbf{I}_p)$ and $u(\mathbf{I}_q)$ are computed by solving the forward problem.

2.5 Inverse problem

2.5.1 Introduction

The problem of estimating the internal conductivity distribution of an object from the Neumann-to-Dirichlet map is known as the *inverse problem* of EIT. From equation (2.17), we have than an EIT image is obtained via minimization of a regularized functional $\Phi(\boldsymbol{\sigma}) : \mathbb{R}^N \rightarrow \mathbb{R}$, where N is the number of elements, of the form

$$\begin{aligned} \boldsymbol{\sigma} &= \arg \min_{\boldsymbol{\sigma}} \frac{1}{2} \|A(\boldsymbol{\sigma}) - \mathbf{v}\|_{\boldsymbol{\Sigma}_h^{-1}}^2 + \tau \Psi(\boldsymbol{\sigma}) \\ &= \arg \min_{\boldsymbol{\sigma}} \Phi(\boldsymbol{\sigma}), \end{aligned} \quad (2.61)$$

where $A(\boldsymbol{\sigma})$ is the forward map, $\boldsymbol{\Sigma}_h$ is the covariance of the measurement noise, $\Psi(\boldsymbol{\sigma})$ is a regularizing function, and τ is the regularization parameter. There are several optimization methods used to minimize the functional. In this section, popular techniques for solving the EIT inverse problem are described. Image reconstruction methods are divided into linear and nonlinear according to the order of approximation used in describing the relationship between the conductivity distribution and the boundary data. First, the choice of regularization term is addressed.

2.5.2 Regularization

The regularization term $\Psi(\boldsymbol{\sigma})$ is chosen on the basis of prior knowledge about the solution of $\boldsymbol{\sigma}$, such as smoothness or sparseness [67]. For example, if the solution is multivariate Gaussian with mean $\boldsymbol{\sigma}_0$ and covariance $\boldsymbol{\Sigma}_\sigma \propto \mathbf{I}$, taking the negative log of the prior (as in equation (2.13)) delivers the expression for *zeroth-order generalized Tikhonov* regularization,

$$\Psi(\boldsymbol{\sigma}) = \frac{1}{2} \|\boldsymbol{\sigma} - \boldsymbol{\sigma}_0\|_{\boldsymbol{\Sigma}_\sigma^{-1}}^2, \quad (2.62)$$

where $\|\cdot\|$ indicates the L^2 -norm. For $\boldsymbol{\Sigma}_\sigma = \mathbf{I}$ and $\boldsymbol{\sigma}_0 = \mathbf{0}$, (2.62) is known simply as *zeroth-order Tikhonov* regularization. This choice of regularization favours small solutions by penalizing solutions with high oscillations [111]. Similarly, higher-order Tikhonov regularization terms impose smoothness to the p th spatial derivative:

$$\Psi(\boldsymbol{\sigma}) = \frac{1}{2} \|\nabla^p \boldsymbol{\sigma}\|^2, \quad (2.63)$$

where for discrete domains ∇ is the finite-differences operator and $\nabla^2 = \nabla \cdot \nabla$ for $p = 2$, $\nabla^3 = \nabla \cdot \nabla \cdot \nabla$ for $p = 3$, and so on for $p \in \mathbb{N}$. For example, *first-order Tikhonov* regularization grants a spatial smoothing effect without biasing the solutions towards a prescribed mean.

Other common choices include Total Variation (TV) regularization [9], which allows for step changes while penalizing high-frequency components

$$\Psi(\boldsymbol{\sigma}) = |\nabla \boldsymbol{\sigma}|, \quad (2.64)$$

and the simple L^1 -norm

$$\Psi(\boldsymbol{\sigma}) = |\boldsymbol{\sigma}|, \quad (2.65)$$

which favours sparse solutions. However, using the L_1 -norm causes computational

difficulties in solving the imaging problem in that the functional is non-differentiable.

The term *Markov Random Field* (MRF) indicates any regularization term which defines a relationship between neighbouring elements. For example, *quadratic MRF* regularization takes the form

$$\Psi(\boldsymbol{\sigma}) = \frac{1}{2} \sum_{n=1}^N \sum_l \left| \sigma_n - \sigma_{l(n)} \right|^2, \quad (2.66)$$

where $l(n)$ runs over the neighbours of the n th element [10]. Quadratic MRF is differentiable, favours solutions with large smooth areas.

2.5.3 Linear algorithms

A simple approximation of the forward problem is obtained by truncating the Taylor series at the first derivative and considering

$$A(\boldsymbol{\sigma}) \approx A(\boldsymbol{\sigma}_0) + \mathbf{J}(\boldsymbol{\sigma}_0) \cdot (\boldsymbol{\sigma} - \boldsymbol{\sigma}_0), \quad (2.67)$$

where $\boldsymbol{\sigma}_0$ is the linearisation point. The difference in expected boundary voltages can be expressed in terms of the conductivity change $\Delta\boldsymbol{\sigma} = \boldsymbol{\sigma} - \boldsymbol{\sigma}_0$ as

$$A(\boldsymbol{\sigma}) - A(\boldsymbol{\sigma}_0) \approx \mathbf{J}(\boldsymbol{\sigma}_0) \cdot \Delta\boldsymbol{\sigma}. \quad (2.68)$$

Therefore a variation in conductivity with respect to a baseline can be reconstructed from knowledge of the resulting variation of the data and the sensitivity matrix. Note that in order to compute $\mathbf{J}(\boldsymbol{\sigma}_0)$, the linearisation point $\boldsymbol{\sigma}_0$ must also be known. It has been shown empirically that the linear approximation is valid for a localized change in conductivity with respect to a baseline of less than 20% [49]. Linearization provides a natural formulation for resolving a low-contrast anomaly from a homogeneous baseline and is suitable for imaging conductivity changes that occur over time, but fails in the implementation of absolute or, with the exception of simple problems, frequency-difference imaging.

Let us consider an object which at time t_0 has a known homogeneous conductivity $\boldsymbol{\sigma}_0$, and at time t_1 has an unknown non-homogeneous conductivity $\boldsymbol{\sigma}_1 = \boldsymbol{\sigma}_0 + \Delta\boldsymbol{\sigma}$. Boundary measurements are acquired at t_0 and t_1 and subtracted to obtain the change in the data $\Delta\mathbf{v}$ (see equation (2.10)), and the sensitivity \mathbf{J} is computed in $\boldsymbol{\sigma}_0$ using (2.60). It remains to find a solution for $\Delta\boldsymbol{\sigma}$ by inverting the linearised forward problem. However, the problem is under determined, i.e. there are more variables than measurements, so

the inverse of the sensitivity matrix \mathbf{J}^{-1} is not defined. Instead, the *pseudoinverse* of the row space of \mathbf{J} , or *Moore-Penrose inverse* for the underdetermined problem, is computed

$$\mathbf{J}^\diamond = \left(\mathbf{J}^T \mathbf{J}\right)^{-1} \mathbf{J}^T, \quad (2.69)$$

where the definition of \mathbf{J}^\diamond is independent of the rank of \mathbf{J} , and \mathbf{J}^T indicates the transpose matrix. Assuming that the measurement noise is white and $\boldsymbol{\Sigma}_h = \mathbf{I}$, the Moore-Penrose inverse returns the solution to the least-squares problem

$$\Delta\boldsymbol{\sigma} = \arg \min_{\Delta\boldsymbol{\sigma}} \frac{1}{2} \|\mathbf{J}\Delta\boldsymbol{\sigma} - \Delta\mathbf{v}\|^2, \quad (2.70)$$

because differentiating equation (2.70) with respect to $\Delta\boldsymbol{\sigma}$ and equating to zero delivers

$$\Delta\boldsymbol{\sigma}_{\text{MP}} = \left(\mathbf{J}^T \mathbf{J}\right)^{-1} \mathbf{J}^T \Delta\mathbf{v} = \mathbf{J}^\diamond \Delta\mathbf{v}. \quad (2.71)$$

In the case of ill-posed problems, the Moore-Penrose inverse would amplify the noise in the data and therefore can not be applied. The methods described below were developed to account for measurement noise.

2.5.3.1 Regularization by filtering

Singular value decomposition (SVD) allows for the inclusion of a filter in computing the pseudo-inverse of the Jacobian, which dampens high spatial frequency components affected by noise. For any \mathbf{J} , we have that $\mathbf{J}^T \mathbf{J}$ is Hermitian and semi-positive definite, so there exists an orthonormal base of eigenvectors $\mathbf{W} = (\mathbf{w}_1, \dots, \mathbf{w}_K) \in \mathbb{R}^{N \times K}$ of $\mathbf{J}^T \mathbf{J}$, with eigenvalues $(\lambda_1, \dots, \lambda_K) \geq 0 \in \mathbb{R}$. If we define the singular values as $\varsigma_k = \sqrt{\lambda_k}$, and $\mathbf{u}_k = \varsigma_k^{-1} \mathbf{J} \mathbf{w}_k \in \mathbb{R}^K$, where $k = 1, \dots, K$, then the following relations are easily obtained

$$\mathbf{J}^T \mathbf{J} \mathbf{w}_k = \lambda_k \mathbf{w}_k = \varsigma_k^2 \mathbf{w}_k \quad (2.72)$$

$$\mathbf{J}^T \mathbf{u}_k = \varsigma_k^{-1} \mathbf{J}^T \mathbf{J} \mathbf{w}_k = \varsigma_k^{-1} \lambda_k \mathbf{w}_k = \varsigma_k \mathbf{w}_k \quad (2.73)$$

$$\mathbf{J} \mathbf{J}^T \mathbf{u}_k = \mathbf{J} \mathbf{J}^T \varsigma_k^{-1} \mathbf{J} \mathbf{w}_k = \varsigma_k \mathbf{J} \mathbf{w}_k = \varsigma_k^2 \mathbf{u}_k. \quad (2.74)$$

These show that the vectors \mathbf{u}_k are eigenvectors of $\mathbf{J} \mathbf{J}^T$ and, given that $\mathbf{J} \mathbf{J}^T$ is Hermitian, the matrix $\mathbf{U} = (\mathbf{u}_1, \dots, \mathbf{u}_K) \in \mathbb{R}^{K \times K}$ defines an orthonormal base of the range of \mathbf{J} . The matrix of singular values \mathbf{S} is defined as the diagonal matrix of the ordered values $\varsigma_1 \geq \varsigma_2 \geq \dots \geq \varsigma_K$ padded with zeros to create a $K \times K$ matrix. Following the definitions

of \mathbf{w}_k and \mathbf{u}_k and \mathbf{S} we have that

$$\mathbf{J}\mathbf{W} = \mathbf{U}\mathbf{S}, \quad (2.75)$$

hence

$$\mathbf{J} = \mathbf{U}\mathbf{S}\mathbf{W}^T. \quad (2.76)$$

This relationship allows for the pseudoinverse (2.69) to be expressed as

$$\mathbf{J}^\diamond = \mathbf{W}\mathbf{S}^{-1}\mathbf{U}^T. \quad (2.77)$$

where \mathbf{S}^{-1} is a diagonal matrix holding the values $1/\varsigma_k$.

SVD reveals why the Moore-Penrose inverse can not be applied to noisy data $\Delta\mathbf{v} = \mathbf{g} + \mathbf{h}$, where \mathbf{g} is the change predicted by the forward map and \mathbf{h} is noise. The Moore-Penrose solution (2.71) is

$$\begin{aligned} \Delta\sigma_{\text{MP}} &= \mathbf{J}^\diamond \Delta\mathbf{v} = \mathbf{J}^\diamond (\mathbf{g} + \mathbf{h}) = \\ &= \sum_{k=1}^K \frac{\mathbf{w}_k \mathbf{u}_k^T}{\varsigma_k} (\mathbf{g} + \mathbf{h}) = \sum_{k=1}^K \frac{\mathbf{w}_k \langle \mathbf{u}_k, \mathbf{g} \rangle}{\varsigma_k} + \frac{\mathbf{w}_k \langle \mathbf{u}_k, \mathbf{h} \rangle}{\varsigma_k}, \end{aligned} \quad (2.78)$$

where the projection of the noise \mathbf{h} onto the singular vectors \mathbf{u}_k is weighted by the inverse of the singular values. The decay rate of the singular values provides information about the ill-posedness of the reconstruction problem. The condition number, that is the ratio between highest and lowest singular values, reflects the instability of the solution with respect to small changes in the data as it indicates the accuracy with which the problem can be solved. The steeper the decay of the singular values below bit precision, the more the problem is ill-posed.

A simple solution is to introduce a step filter

$$f_k^{\text{tSVD}} = \begin{cases} 1 & \text{if } k \leq T \\ 0 & \text{if } k > T \end{cases}, \quad (2.79)$$

where $T < K$ is an appropriate truncation level. This method is known as *truncated singular value decomposition*, or tSVD. The truncation can be set to an arbitrary value, such as the value for which the corresponding SV is less than 1/100 of the largest SV, or selected empirically, or computed using an objective selection method.

Alternatively, the singular values can be damped gradually according to a regulariza-

tion hyperparameter τ , so that

$$f_k^{\text{Tikh}} = \frac{\varsigma_k^2}{\varsigma_k^2 + \tau}. \quad (2.80)$$

In this case, the filtered pseudo-inverse becomes

$$\mathbf{J}_{\text{Tikh}}^\diamond = \sum_{k=1}^K \frac{f_k^{\text{Tikh}} \mathbf{w}_k \mathbf{u}_k^T}{\varsigma_k} = (\mathbf{J}^T \mathbf{J} + \tau \mathbf{I})^{-1} \mathbf{J}^T, \quad (2.81)$$

which returns the solution to the least-squares problem with zero-order Tikhonov regularization

$$\boldsymbol{\sigma} = \arg \min_{\Delta \boldsymbol{\sigma}} \frac{1}{2} \left[\|\mathbf{J} \Delta \boldsymbol{\sigma} - \Delta \mathbf{v}\|^2 + \tau \|\Delta \boldsymbol{\sigma}\|^2 \right]. \quad (2.82)$$

Similarly, the solution to the least-squares problem with a generic quadratic regularization of the form

$$\boldsymbol{\sigma} = \arg \min_{\Delta \boldsymbol{\sigma}} \frac{1}{2} \left[\|\mathbf{J} \Delta \boldsymbol{\sigma} - \Delta \mathbf{v}\|^2 + \tau \Delta \boldsymbol{\sigma}^T \mathbf{L} \Delta \boldsymbol{\sigma} \right]. \quad (2.83)$$

is given by

$$\Delta \boldsymbol{\sigma}_{\text{GT}} = \mathbf{J}_{\text{GT}}^\diamond \Delta \mathbf{v} = (\mathbf{J}^T \mathbf{J} + \tau \mathbf{L})^{-1} \mathbf{J}^T \Delta \mathbf{v}, \quad (2.84)$$

which for $\mathbf{L} = \nabla^T \nabla$ is the first-order Tikhonov regularized solution.

2.5.3.2 Variational methods

Variational methods involve the minimization of the regularized linear least squares functional

$$\boldsymbol{\sigma} = \arg \min_{\boldsymbol{\sigma}} \|\mathbf{J} \Delta \boldsymbol{\sigma} - \Delta \mathbf{v}\|_{\boldsymbol{\Sigma}_h^{-1}}^2 + \tau \Psi(\Delta \boldsymbol{\sigma}), \quad (2.85)$$

by considering a perturbation of the variable. Iterative optimization methods such as steepest descent or conjugate gradients are available, which avoid inverting the Jacobian directly. The non-linear variant of these methods are described in the following section. These can easily be reduced to the linear case if the second order derivative of the objective function is ignored, and the number of iterations is set to 1.

2.5.4 Non-linear iterative algorithms

Non linear approaches are mainly based on the iterative search for the global minimum of the objective function $\Phi(\boldsymbol{\sigma})$ (equation (2.61)). At each step, a hypothesis for the minimum is formulated and verified. The methods differ in the criteria to select the minimization step and direction in which to update the variable.

2.5.4.1 Steepest descent

The *steepest descent* method is for iteratively minimizing a multi-variant functional $\Phi(\boldsymbol{\sigma}) : \mathbb{R}^N \rightarrow \mathbb{R}$ by selecting a starting point $\boldsymbol{\sigma}_{t=0}$, where t is an iteration counter, and stepping towards the minimum by following the direction along which the function decreases most rapidly. As the gradient direction $\nabla\Phi$ identifies the direction of steepest increase, the most efficient way to minimize the function must be to follow the opposite direction. The solution is updated as follows

$$\boldsymbol{\sigma}_{t+1} = \boldsymbol{\sigma}_t - \alpha_t \nabla\Phi(\boldsymbol{\sigma}_t) \quad (2.86)$$

where α_t is the step size. The gradient is

$$\nabla\Phi(\boldsymbol{\sigma}_t) = \mathbf{J}^T \boldsymbol{\Sigma}_h^{-1} (A(\boldsymbol{\sigma}_t) - \mathbf{v}) + \tau \nabla\Psi(\boldsymbol{\sigma}_t), \quad (2.87)$$

where $\mathbf{J} = \mathbf{J}(\boldsymbol{\sigma}_t)$ and $\boldsymbol{\Sigma}_h$ is the correlation of the measurement noise.

The gradient reflects only local properties of the function; therefore the step size must be carefully chosen so that the algorithm does not converge to a local, rather than global, minimum. The value of α_t can be either predefined or obtained via a 1D line-search

$$\alpha_t = \arg \min_{\alpha_t > 0} \Phi(\boldsymbol{\sigma}_t - \alpha_t \nabla\Phi(\boldsymbol{\sigma}_t)). \quad (2.88)$$

Convergence of the steepest-descent method can be slow because only the first order derivative information is used.

2.5.4.2 Newton-type methods

The Newton method was developed initially to approximate the root of a nonlinear one-dimensional function. This technique was adapted to minimize a multi-variable functional by searching for the root of its derivative.

The functional $\Phi(\boldsymbol{\sigma}) : \mathbb{R}^N \rightarrow \mathbb{R}$ is approximated locally by the quadratic form

$$\Phi(\boldsymbol{\sigma}_t + \mathbf{d}_t) \approx \Phi(\boldsymbol{\sigma}_t) + \nabla\Phi(\boldsymbol{\sigma}_t)^T \mathbf{d}_t + \frac{1}{2} \mathbf{d}_t^T \nabla^2\Phi(\boldsymbol{\sigma}_t) \mathbf{d}_t, \quad (2.89)$$

where $\nabla^2\Phi(\boldsymbol{\sigma}_t) \in \mathbb{R}^{N \times N}$ is the Hessian and $\nabla\Phi(\boldsymbol{\sigma}_t) \in \mathbb{R}^N$ is the gradient of the objective function calculated in $\boldsymbol{\sigma}_t$.

In order to find the update that minimizes the function, the derivative is taken and

equated to zero

$$\frac{\partial}{\partial \mathbf{d}_t} \Phi(\boldsymbol{\sigma}_t + \mathbf{d}_t) = \nabla \Phi(\boldsymbol{\sigma}_t) + \nabla^2 \Phi(\boldsymbol{\sigma}_t) \mathbf{d}_t = 0, \quad (2.90)$$

this leads to the equation

$$\nabla \Phi(\boldsymbol{\sigma}_t) = -\nabla^2 \Phi(\boldsymbol{\sigma}_t) \mathbf{d}_t \implies \mathbf{d}_t = -\nabla^2 \Phi(\boldsymbol{\sigma}_t)^{-1} \nabla \Phi(\boldsymbol{\sigma}_t), \quad (2.91)$$

which identifies the search direction \mathbf{d}_t , also known as Newton direction. The difficulty of Newton methods lies in the calculation of the Hessian matrix. The *Gauss-Newton* method assumes that the second order derivative of the residual error is negligible, so that

$$\nabla^2 \Phi(\boldsymbol{\sigma}_t) = \mathbf{J}^T \boldsymbol{\Sigma}_h^{-1} \mathbf{J} + \tau \nabla^2 \Psi(\boldsymbol{\sigma}_t). \quad (2.92)$$

If the number of elements of the mesh is large, it is computationally very demanding to store and invert the Hessian matrix. This can be avoided by using a Krylov solver, such as generalized minimal residuals (GMRes) [95] or linear conjugate gradients (CG) [98], to solve

$$\begin{aligned} \nabla \Phi(\boldsymbol{\sigma}_t) &= - \left[\mathbf{J}^T \boldsymbol{\Sigma}_h^{-1} \mathbf{J} + \tau \nabla^2 \Psi(\boldsymbol{\sigma}_t) \right] \mathbf{d}_t \\ &= -\mathbf{J}^T \boldsymbol{\Sigma}_h^{-1} (\mathbf{J} \mathbf{d}_t) - \tau \nabla^2 \Psi(\boldsymbol{\sigma}_t) \mathbf{d}_t, \end{aligned} \quad (2.93)$$

where the brackets highlight the order in which to make the computation. In this case, the Hessian is never formulated explicitly, and only the result of the application of the Hessian to a vector is stored.

The general formulation of the update rule for Newton methods is

$$\boldsymbol{\sigma}_{t+1} = \boldsymbol{\sigma}_t + \alpha_t \mathbf{d}_t = \boldsymbol{\sigma}_t - \alpha_t \nabla^2 \Phi(\boldsymbol{\sigma}_t)^{-1} \nabla \Phi(\boldsymbol{\sigma}_t), \quad (2.94)$$

where α_t is the step size. The *damped* variant allows for a variable α_t , which is selected by performing a line-search along the direction \mathbf{d}_t . Otherwise $\alpha_t = 1$.

The effectiveness of Newton methods depend on the curvature information inherent in the Hessian. If $\nabla^2 \Phi(\boldsymbol{\sigma}_t)$ is positive definite and continuous, then the minimum can be found in one step for any initial guess $\boldsymbol{\sigma}_0$. If $\nabla^2 \Phi(\boldsymbol{\sigma}_t)$ is Lipschitz continuous the algorithm converges to the quadratic minimum as long as the initial guess is close enough to the solution. The algorithm may not converge for a non positive definite Hessian.

2.5.4.3 Levenberg-Maquardt

An alternative to the line-search strategy is to define a *trust region* of diameter δ around $\boldsymbol{\sigma}_t$ for which the quadratic approximation (2.89) is assumed to be valid. The problem is replaced by another, more stable, by approximating the Hessian matrix with $\tilde{\mathbf{H}} = \nabla^2 \Phi(\boldsymbol{\sigma}_t) + \lambda \mathbf{I}$, so that

$$\Phi(\boldsymbol{\sigma}_t + \mathbf{d}_t) \approx \Phi(\boldsymbol{\sigma}_t) + \nabla \Phi(\boldsymbol{\sigma}_t)^T \mathbf{d}_t + \frac{1}{2} \mathbf{d}_t^T \tilde{\mathbf{H}} \mathbf{d}_t. \quad (2.95)$$

where the step size and direction are determined simultaneously

$$\mathbf{d}_t = \min_{\mathbf{d}_t \in \mathbb{R}^N} \Phi(\boldsymbol{\sigma}_t + \mathbf{d}_t) \quad (2.96)$$

and $\|\mathbf{d}_t\| \geq \delta$. If a $\lambda \geq 0$ exists such that

$$\begin{cases} (\nabla^2 \Phi(\boldsymbol{\sigma}_t) + \lambda \mathbf{I}) \mathbf{d}_t + \nabla \Phi(\boldsymbol{\sigma}_t) = 0 \\ \lambda(\delta - \|\mathbf{d}_t\|) = 0 \\ \boldsymbol{\sigma}_t^T \nabla^2 \Phi(\boldsymbol{\sigma}_t) \boldsymbol{\sigma}_t \geq 0 \end{cases} \quad \forall \boldsymbol{\sigma}_t \in \mathbb{R}^N \quad (2.97)$$

then \mathbf{d}_t is the trust region global minimum. Levenberg-Maquardt reduces to the Gauss-Newton method for $\lambda_t \rightarrow 0$, and to steepest descent for $\lambda \rightarrow \infty$. Therefore it can be interpreted as a hybrid method, where λ_t is a steering factor. This method combines the robustness of steepest descent with the fast convergence of Gauss-Newton.

2.5.4.4 Non-linear Conjugate Gradient

The nonlinear variant of the Conjugate Gradient method (NLCG) avoids calculating and inverting the Hessian, with significant computational advantages. In order to maximize efficiency, the search direction \mathbf{d}_t is calculated by Gram-Schmidt conjugation of the previous directions $\mathbf{d}_{t-1}, \dots, \mathbf{d}_0$. The outline of the algorithm is as follows [98]:

initialize *tol* and *maxit*

initialize search direction $\mathbf{d}_0 = \mathbf{r}_0 = -\nabla \phi(\boldsymbol{\sigma}_0)$ (steepest descent)

repeat

 find α_t that minimizes $\Phi(\boldsymbol{\sigma}_t + \alpha_t \mathbf{d}_t)$

 update variable $\boldsymbol{\sigma}_{t+1} = \boldsymbol{\sigma}_t + \alpha_t \mathbf{d}_t$

 calculate $\mathbf{r}_{t+1} = -\nabla \phi(\boldsymbol{\sigma}_{t+1})$ and $\beta = \max \left\{ \frac{\mathbf{r}_{t+1}^T (\mathbf{r}_{t+1} - \mathbf{r}_t)}{\mathbf{r}_t^T \mathbf{r}_t}, 0 \right\}$

update search direction $\mathbf{d}_{t+1} = \mathbf{r}_{t+1} + \beta_{t+1}\mathbf{d}_t$.
 $t \leftarrow t + 1$
until $|\Phi(\boldsymbol{\sigma}^{t+1}) - \Phi(\boldsymbol{\sigma}^t)| \leq \text{tol}$ or $t = \text{maxit}$

This choice of β is known as *Polak-Ribière* scheme, and it guarantees convergence by restarting CG when $\beta < 0$ [81]. This is equivalent to ignoring all precedent search directions and repeating the minimum search along the direction of steepest descent. Convergence of CG is slow because only the first order information is used, and is not guaranteed if the initial guess is too far away from the solution.

2.5.4.5 Line search

Local convergence of non-linear reconstruction methods is guaranteed either by finding a trust-region (as in Levenberg-Marquardt), or by performing a 1D line-search along the update direction. The objective of the latter method is to determine the step size α_t , given the search direction \mathbf{d}_t , by minimizing

$$\alpha_t = \arg \min_{\alpha_t > 0} \Phi(\boldsymbol{\sigma}_t + \alpha_t \mathbf{d}_t). \quad (2.98)$$

For small problems there are several options for solving equation (2.98). Using the quadratic approximation, as in Newton-type methods, the local objective function can be approximated by a parabola. However this requires knowledge of the second-order derivative, which may be computationally expensive. Alternatively, the secant method requires knowledge of the gradient at two points near the minimum.

For large scale problems, the *Brent* method is optimal in that for each iteration it only requires storage of the value of the functional at 6 points along the update direction [15]. First a bounding interval $[a, b]$ is found, for which there exist a step size c such that $a \leq c \leq b$ and

$$\Phi(\boldsymbol{\sigma}_t + c\mathbf{d}_t) \leq \Phi(\boldsymbol{\sigma}_t + a\mathbf{d}_t) \wedge \Phi(\boldsymbol{\sigma}_t + c\mathbf{d}_t) \leq \Phi(\boldsymbol{\sigma}_t + b\mathbf{d}_t). \quad (2.99)$$

Then a parabolic fit is performed between $\Phi(\boldsymbol{\sigma}_t + c\mathbf{d}_t)$, $\Phi(\boldsymbol{\sigma}_t + a\mathbf{d}_t)$, and $\Phi(\boldsymbol{\sigma}_t + b\mathbf{d}_t)$. If the step size m corresponding to minimum of the parabola is in the bounding interval $[a, b]$, then the point is accepted. Otherwise, a golden section step is performed between a , b and $d = \text{mean}(a, b)$: the intervals $[a, d]$ and $[d, b]$ are divided by the golden ratio $(\sqrt{5} - 1)/2 \approx 0.618$ to find e and f , the function is evaluated for step sizes e and f ,

the minimum is re-evaluated, and the brackets are updated accordingly. The process is restarted by fitting a parabola between the the new minimum and brackets. Ideally, the method would switch between parabolic and golden-section steps, so that the minimum is updated according to the former and the brackets converge towards the minimum due to the latter [123].

2.5.5 Nonlinear direct methods

Direct methods attempt to solve the nonlinear inverse problem analytically. These methods could potentially provide a non-iterative nonlinear algorithm, but application is limited to simple problems and the sensitivity to experimental and boundary geometry errors is very high. In most cases, proofs are provided for the continuous electrode model

$$\int_{\delta\Omega} I(\mathbf{x}, \omega) dS = 0, \quad (2.100)$$

which assumes that there is no contact impedance, and that current can be applied and voltages measured anywhere on the boundary. The continuous model does not predict experimental measurements with satisfactory precision, and extension of direct methods to the complete electrode model (2.37) can be problematic.

2.5.5.1 D-bar method

The *d-bar* method is based on Nachman's proof of the global uniqueness of EIT for C^2 conductivity distributions in 2D [75, 100]. A simply connected C^∞ domain Ω is considered, on which a conductivity distribution $\sigma(\mathbf{x})$, such that $\sigma \equiv 1$ in a neighbourhood of $\delta\Omega$, is defined. The transformation $\tilde{u} = \sqrt{\sigma}u$ is applied to the Laplace equation to obtain the Schrödinger equation

$$-\nabla^2 \tilde{u} + q\tilde{u} = 0, \quad \text{in } \Omega \quad (2.101)$$

where $q(\mathbf{x}) = \nabla^2 \sqrt{\sigma} / \sqrt{\sigma}$. If the conductivity is smoothly extended so that $\sigma = 1$ and $q = 0$ on $\mathbb{R}^2 \setminus \Omega$, then for any $\mathbf{k} = (k_1, k_2) \in \mathbb{C}$ such that $\mathbf{k} \cdot \mathbf{k} = 0$, there is a solution $\Psi(\mathbf{x}, \mathbf{k})$ such that

$$-\nabla^2 \Psi(\mathbf{x}, \mathbf{k}) + q\Psi(\mathbf{x}, \mathbf{k}) = 0, \quad \text{in } \mathbb{R}^2, \quad (2.102)$$

where the 2D spatial variables are expressed by complex numbers

$$\mathbf{x} = (x_1, x_2) = x_1 + ix_2,$$

and the product is complex multiplication.

The *scattering transform* is defined as

$$\begin{aligned} t(\mathbf{k}) &= \int_{\mathbb{R}^2} e^{i\bar{\mathbf{k}}\bar{\mathbf{x}}} \Psi(\mathbf{x}, \mathbf{k}) q(\mathbf{x}) \, d\mathbf{x} \\ &= \int_{\mathbb{R}^2} e_k(\mathbf{x}) \mu(\mathbf{x}, \mathbf{k}) q(\mathbf{x}) \, d\mathbf{x}, \end{aligned} \quad (2.103)$$

where $e_k(\mathbf{x}) = \exp i(\bar{\mathbf{k}}\bar{\mathbf{x}} + \mathbf{k}\mathbf{x})$ and $\mu(\mathbf{x}, \mathbf{k}) = \exp -i\mathbf{k}\mathbf{x}\Psi(\mathbf{x}, \mathbf{k})$. It has been shown that $\mu(\mathbf{x}, \mathbf{k})$ tends to 1 for $|\mathbf{x}| \rightarrow \infty$, therefore $t(\mathbf{k})$ approximates the Fourier transform of $q(\mathbf{x})$ in $(-2k_1, 2k_2)$. The scattering transform satisfies the d-bar equation

$$\frac{\partial}{\partial \bar{\mathbf{k}}} \mu(\mathbf{x}, \mathbf{k}) = \frac{1}{4\pi \bar{\mathbf{k}}} t(\mathbf{k}) e_{-\mathbf{k}}(\mathbf{x}) \overline{\mu(\mathbf{x}, \mathbf{k})}, \quad (2.104)$$

which allows for recovering $\mu(\mathbf{x}, \mathbf{k})$ from $t(\mathbf{k})$. Using $q = 0$ on $\mathbb{R}^2 \setminus \Omega$, $\mathbf{k} \cdot \mathbf{k} = 0$, and the Schrödinger equation, the following equivalence is obtained

$$t(\mathbf{k}) = \int_{\delta\Omega} e^{i\bar{\mathbf{k}}\bar{\mathbf{x}}} (\Lambda_\sigma - \Lambda_1) \Psi(\mathbf{x}, \mathbf{k}) \, ds, \quad (2.105)$$

which expresses the scattering transform in terms of the Dirichlet-to-Neumann map, where Λ_1 is defined for the homogeneous domain $\sigma = 1$. Finally the conductivity is recovered using

$$\sqrt{\sigma} = \lim_{\mathbf{k} \rightarrow 0} \mu(\mathbf{x}, \mathbf{k}). \quad (2.106)$$

The d-bar method has been applied successfully to imaging cardiac activity [56] and has been extended to three-dimensional problems in the low frequency limit [28], and more recently to non-smooth 2D conductivities [4].

2.5.5.2 Factorization method

The *factorization* method [21] allows for the localization of inclusions in a known homogeneous background, without reconstructing the conductivity. A domain $\Omega \subset \mathbb{R}^N$ is considered, where $N \geq 2$ and $\delta\Omega$ is C^2 . A conductivity distribution $\sigma(\mathbf{x})$ is defined on Ω such that

$$\sigma(\mathbf{x}) = \begin{cases} \kappa(\mathbf{x}) & \text{in } \overline{\Omega^c} = \bigcup_i \overline{\Omega_i^c} \\ 1 & \text{in } \Omega \setminus \overline{\Omega^c}, \end{cases} \quad (2.107)$$

where $0 \leq \kappa(\mathbf{x}) \leq 1 \in C^2$ on $\overline{\Omega^c}$, and $\Omega \setminus \overline{\Omega^c}$ is simply connected. It follows the properties of $\sigma(\mathbf{x})$ that the operator $\Lambda_\sigma - \Lambda_1$ is self-adjoint, compact, and semipositive definite on Ω . Therefore, $\Lambda_\sigma - \Lambda_1$ has a well defined square root, and admits a basis of eigenfunctions

v_k , with eigenvalues λ_k . The Picard criterion applies, which states that a test function φ belongs to the range of $\{\Lambda_\sigma - \Lambda_1\}^{\frac{1}{2}}$ if and only if

$$\sum_{k=1}^{\infty} \frac{\langle \varphi, v_k \rangle^2}{\lambda_k} < \infty. \quad (2.108)$$

The dipole point source located in position \mathbf{y} with unit direction \mathbf{d} is considered for each $\mathbf{y} \in \Omega$. The dipole potential $G_{y,d}(\mathbf{x})$ satisfies the equations

$$\nabla^2 G_{y,d}(\mathbf{x}) = \mathbf{d} \cdot \nabla_{\mathbf{x}} \delta(\mathbf{x} - \mathbf{y}) \text{ in } \Omega, \quad (2.109)$$

$$\frac{\partial G_{y,d}(\mathbf{x})}{\partial n} = 0 \quad \text{on } \delta\Omega, \quad (2.110)$$

$$\int_{\delta\Omega} G_{y,d}(\mathbf{x}) ds = 0. \quad (2.111)$$

It has been shown that a point \mathbf{y} belongs to the inclusion Ω^c if and only if $g_{y,d}(\mathbf{x}) = G_{y,d}(\mathbf{x})|_{\delta\Omega}$ belongs to the range of $\{\Lambda_\sigma - \Lambda_1\}^{\frac{1}{2}}$. This condition can be tested for each point in the domain using the Picard criterion (2.108) with $\varphi = g_{y,d}(\mathbf{x})$. For proofs and implementation details see [20, 54]. The factorization method has been recently extended to the complete electrode model, but application to numerical phantoms is highly sensitive to noise [65].

2.5.6 Other methods

Layer stripping is a method for recovering conductivity by proceeding layer by layer, from the outside in [103, 8]. In three dimensions, the implementation is highly unstable and cannot be applied in practice, even to noiseless data. A stable algorithm exists only for one-dimensional or radially symmetric 2D conductivities [106].

Level set methods are suitable for reconstructing conductivities with jump discontinuities at the interface between a homogeneous background Ω_e and inclusions Ω_i . A level set function $\Gamma(\mathbf{x})$ is defined so that

$$\sigma(\mathbf{x}) = \begin{cases} \sigma_i & \text{if } \Gamma(\mathbf{x}) < 0, \\ \sigma_e & \text{if } \Gamma(\mathbf{x}) > 0, \end{cases} \quad (2.112)$$

where the conductivity of the background σ_e and inclusions σ_i are known, and $\Gamma(\mathbf{x}) = 0$ on the interface $\delta\Omega_i$. If the mapping $\Gamma \rightarrow \sigma$ defined above is named $\chi(\Gamma)$, then the forward map $A(\sigma)$ can be redefined in terms of Γ as

$$\Sigma(\Gamma) = A(\chi(\Gamma)). \quad (2.113)$$

Using the chain rule, the derivative of Σ is obtained

$$\frac{\partial \Sigma(\Gamma)}{\partial \Gamma} \delta \Gamma = \frac{\partial A}{\partial \chi} \frac{\partial \chi}{\partial \Gamma} \delta \Gamma. \quad (2.114)$$

Linearising $\chi(\Gamma)$ delivers [96]

$$\frac{\partial \chi}{\partial \Gamma} \delta \Gamma = -(\sigma_i - \sigma_e) \frac{\delta \Gamma}{|\nabla \Gamma|} \delta_{\delta \Omega_i}, \quad (2.115)$$

where in practice the delta function on the interface $\delta_{\delta \Omega_i}$ can be substituted with a narrow-band indicator function [102, 101]. The Gauss-Newton update rule for the level set function Γ is thus derived from equations (2.114) and (2.115). The first clinical images of lung ventilation using the level set method and time-difference data have been produced recently [90].

2.5.7 Regularization parameter selection

The role of the regularization parameter is to balance the trade-off between fitting the measurement data and adhering to the prior distribution of the variable. If the regularization parameter is too low, the solution will be contaminated by noise, and if the regularization is too high, the information provided by the data will be lost.

An unknown object $\boldsymbol{\sigma}^{\text{true}}$ is considered, that gives rise to measurements

$$\mathbf{v} = A(\boldsymbol{\sigma}^{\text{true}}) + \mathbf{h},$$

where the noise \mathbf{h} is white Gaussian with covariance $\boldsymbol{\Sigma}_h = \mu^2 \mathbf{I}$

$$\mathbf{h} \sim \mathcal{N}_h(\mathbf{0}, \mu^2 \mathbf{I}).$$

If $\boldsymbol{\sigma}^\tau$ is the solution of the reconstruction problem (2.61) obtained for a certain regularization parameter τ , then the *residual error* is defined as

$$r(\boldsymbol{\sigma}^\tau, \mathbf{v}) = A(\boldsymbol{\sigma}^\tau) - \mathbf{v}. \quad (2.116)$$

If the distribution the measurement noise is known, then it is desirable to equate the norm of the residual and the expected norm of the noise

$$\|r(\boldsymbol{\sigma}^\tau, \mathbf{v})\|^2 = N\mu^2 \Rightarrow \frac{1}{N} \|r(\boldsymbol{\sigma}^\tau, \mathbf{v})\|^2 - \mu^2 = 0, \quad (2.117)$$

this is the *discrepancy principle*.

The discrepancy principle does not account for the statistics of the solution, which, as per the Bayesian formulation (2.13), has a prior distribution

$$\boldsymbol{\sigma} \sim \exp[-\Psi(\boldsymbol{\sigma})]. \quad (2.118)$$

The choice of τ should balance the contribution of the two terms of the objective function, so that

$$\frac{\|r(\boldsymbol{\sigma}^\tau, \mathbf{v})\|^2}{\mu^2} - \tau \Psi(\boldsymbol{\sigma}^\tau) = 0 \quad \Rightarrow \quad \tau = \frac{\|r(\boldsymbol{\sigma}^\tau, \mathbf{v})\|^2}{\mu^2 \Psi(\boldsymbol{\sigma}^\tau)}, \quad (2.119)$$

this is the *Miller criterion* [73, 43].

In most cases the noise variance μ is not known, but a graphical interpretation of the Miller criterion allows for an approximate estimation of τ . The plot $\left\{ \|r(\boldsymbol{\sigma}^\tau, \mathbf{v})\|^2, \Psi(\boldsymbol{\sigma}^\tau) \right\}$ for different values of τ presents a typical L-shaped curve for ill-posed problems. If τ is too small, the solution is under-regularized, and the norm of the residual error tends to zero. If τ is too large, the solution is over-regularized, and the norm of the prior tends to zero. The transition for over to under-regularization is usually quite fast, and the L-curve presents a sharp corner in the log-log scale. The derived τ corresponds to the corner, which is found by maximizing the curvature of the graph. This is known as the *L-curve method* [42].

2.6 Multifrequency EIT

2.6.1 Introduction

Multifrequency EIT (MFEIT) involves varying the modulation frequency of the injected current, and acquiring multiple data sets at two or more frequencies. These are then considered simultaneously to recover a quantitative or qualitative image of the object. The purpose of multifrequency methods is to include more data, and therefore more information, in the imaging process. Often, the goal is to provide an imaging modality that can provide satisfactory images from data acquired at a single time-point. Thus, the main motivation in pursuing multifrequency EIT is diagnostic imaging.

In this section, MFEIT methods available before the publication of the work presented in this thesis are reviewed. The following techniques are frequency-difference methods, which aim to recover the contrast between two frequencies (see section 2.1.3). Particularly important are the assumptions implicit in these methods, which limit their application to simple problems.

2.6.2 Simple frequency-difference

The simple frequency-difference method can be used to resolve one or more small objects or inclusions from a background. Implementation of the algorithm requires the following assumptions:

1. if $\frac{\partial \sigma}{\partial \omega} = 0$ then $\frac{\partial v}{\partial \omega} = 0$;
2. if $\epsilon_0(\omega)$ is the conductivity of the background, then $\frac{\partial \epsilon_0}{\partial \omega} = 0$.

The first assumption is valid if variations across frequency of the stray capacitance and electrode contact impedance are negligible, and the second if $\epsilon_0(\omega) = \epsilon_0$ is constant over frequency. If the object were homogeneous with conductivity ϵ_0 , the resulting voltages would be constant $v^0(\omega) = v^0$. Therefore any variation across frequencies in the voltage measurements $v(\omega)$ is due to the frequency-dependence of the conductivity of the inclusions. Let us consider two measurement frequencies ω_1 and ω_2 . The frequency-difference data is

$$\Delta v_{\text{FD}} = v(\omega_2) - v(\omega_1). \quad (2.120)$$

The Jacobian for the homogeneous case is computed $\mathbf{J}(\sigma^0)$, where $\sigma_0 = \epsilon_0 \cdot \mathbf{1}$. Note that the Jacobian is independent of frequency. Using the linear approximation for the forward map (2.67) delivers

$$\begin{aligned} \Delta_{\text{FD}} v &= v(\omega_2) - v(\omega_1) \\ &= v(\omega_2) - v^0 - (v(\omega_1) - v^0) \\ &\approx \mathbf{J}(\sigma^0) \cdot [\sigma(\omega_2) - \sigma^0] - \mathbf{J}(\sigma^0) \cdot [\sigma(\omega_1) - \sigma^0] \\ &\approx \mathbf{J}(\sigma^0) \cdot [\sigma(\omega_2) - \sigma(\omega_1)], \end{aligned} \quad (2.121)$$

where v^0 are the hypothetical boundary voltages for the homogeneous case.

The simple-frequency difference algorithm has been applied successfully in tank experiments to resolve a frequency dependant anomaly from a saline background using a linear reconstruction scheme. It has been shown that the method breaks down in the case that the conductivity of the background medium changes across frequencies [83].

2.6.3 Weighted frequency difference

The weighted-frequency-difference algorithm [97] extends the simple frequency difference method to the case of a frequency-dependent background. A small perturbation can be resolved from a large background by taking a weighted difference between boundary

voltage data acquired at two frequencies. The weighting constant is chosen in order to suppress the background signal, whilst preserving the contrast of the perturbation. The algorithm is effective if the impedance change of the perturbation over the chosen measurement frequencies is much larger than that of the background, and the perturbation is small and distant from the boundary.

Let us consider an object with conductivity σ , composed of a background and a small anomaly. Boundary voltage measurements are acquired at two frequencies ω_1 and ω_2 . The weighted conductivity difference

$$\Delta\sigma(\omega_1, \omega_2) = \delta \cdot \sigma(\omega_2) - \sigma(\omega_1) \quad (2.122)$$

is considered, where $\delta \in \Re$ is a constant that satisfies the following conditions

1. $\Delta\sigma(\omega_1, \omega_2) \approx 0$ near the boundary $\delta\Omega$
2. $\Delta\sigma(\omega_1, \omega_2) \gg 0$ on the perturbation.

In order to determine δ , the relationship between the measurements $\mathbf{v}(\omega_1)$ and $\mathbf{v}(\omega_2)$ must be investigated. If $\sigma_0(\omega) = \epsilon_0(\omega) \cdot \mathbf{1}$ is a frequency-dependent homogeneous conductivity distribution, then under the linear approximation the corresponding boundary voltage data vectors $\mathbf{v}_0(\omega_1)$ and $\mathbf{v}_0(\omega_2)$ are parallel and related by the equation

$$\mathbf{v}_0(\omega_2) = \frac{\epsilon_0(\omega_1)}{\epsilon_0(\omega_2)} \mathbf{v}_0(\omega_1). \quad (2.123)$$

In the case of a non-homogeneous conductivity $\sigma(\omega)$, decomposing $\mathbf{v}(\omega_2)$ according to the projection on $\mathbf{v}(\omega_1)$ yields

$$\mathbf{v}(\omega_2) = \delta \cdot \mathbf{v}(\omega_1) + \mathbf{h}(\omega_2) \quad (2.124)$$

where δ is defined as

$$\delta = \frac{\langle \mathbf{v}(\omega_2), \mathbf{v}(\omega_1) \rangle}{\langle \mathbf{v}(\omega_1), \mathbf{v}(\omega_1) \rangle}. \quad (2.125)$$

It is evident from (2.123) that in the absence of an anomaly $\mathbf{h}(\omega_2) = 0$. Therefore the residual vector $\mathbf{h}(\omega_2)$ must contain the information regarding the perturbation, while the projection on $\mathbf{v}(\omega_1)$ carries mostly the background influence. For this reason, the weighted frequency-difference algorithm attempts to reconstruct the weighted change in conductivity $\Delta\sigma(\omega_1, \omega_2)$ from the weighted change in boundary voltages $\mathbf{v}(\omega_2) - \delta \cdot \mathbf{v}(\omega_1)$ using a linear method. For full implementation details see [97, 58].

The weighted frequency-difference algorithm has been shown to be superior to the simple frequency-difference method in numerical simulation [97], in 2D tank experiments [58], and more recently in a semi-spherical 3D tank [3].

2.7 Image segmentation

2.7.1 Introduction

Image segmentation is the process of labelling the voxels in an image, so that voxels with the same labels share certain characteristics. Segmentation allows for the easy interpretation of an image, and the extraction of clinically relevant information.

2.7.2 Labelling problem with MRF prior

We consider the problem of assigning a set of binary labels $x_n \in \mathcal{T} = \{0, 1\}$ to a set of image voxels $\mathcal{V} = \{1, \dots, n, \dots, N\}$. A common approach is to treat the labelling problem as an optimization problem; an objective function is defined in the space of all possible labellings $\mathcal{X} = \{\mathcal{X}_1, \dots, \mathcal{X}_n, \dots, \mathcal{X}_N\}$, where \mathcal{X}_n takes values in \mathcal{T} , the minimum of which is the solution. This energy-minimization approach can be justified in the Bayesian formulation:

$$\begin{aligned} \mathbf{x} &= \arg \max_{\mathbf{x}} \left[\prod_{n=1}^N p(y_n | x_n) \right] p(\mathbf{x}) \\ &= \arg \min_{\mathbf{x}} \sum_{n=1}^N \mathcal{L}(x_n, y_n) + \Psi(\mathbf{x}) \end{aligned} \quad (2.126)$$

where y_n is the observed value in the n th site, $\mathcal{L}(x_n, y_n) = -\log(p(y_n | x_n))$ is the likelihood of the image value y_n given the label x_n , and $\Psi(\mathbf{x}) = -\log(p(\mathbf{x}))$ is the regularization term. The likelihood is determined by the choice of an *appearance model* for the image. For example, a greyscale image assuming values between 0 and 255 can be segmented into black (label $y_n = 1$) and white (label $y_n = 2$) regions by taking the likelihood function:

$$\begin{aligned} \mathcal{L}(x_n, 1) &= x_n / 255 \\ \mathcal{L}(x_n, 2) &= 1 - x_n / 255 \end{aligned} \quad (2.127)$$

where $0 \leq x_n \leq 255$ is the value of the image (figure 2.6).

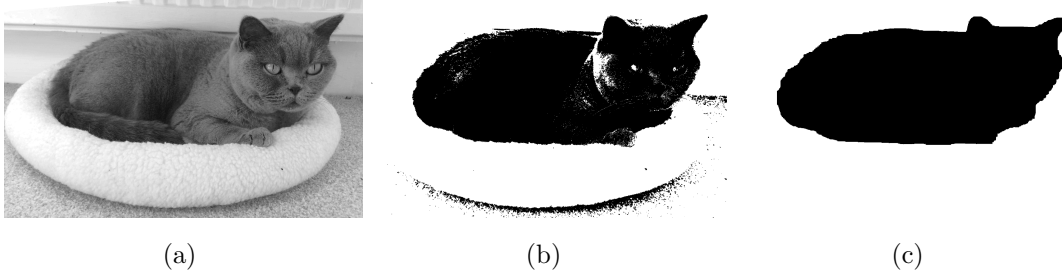


Figure 2.6: Binary image segmentation example: (a) original greyscale image (b) segmentation obtained using likelihood function (2.127) without a spatial prior (c) segmentation obtained via graph cut optimization after the addition of an MRF spatial smoothing term on neighbouring pixels.

The prior $p(\mathbf{x})$ defines a Markov Random Field if

$$p(\mathbf{x}) \geq 0 \quad \forall \mathbf{x} \in \mathcal{X} \quad (2.128)$$

$$p(x_n | x_{\mathcal{V} \setminus \{n\}}) = p(x_n | x_{\mathcal{N}_n}) \quad (2.129)$$

where \mathcal{N}_n defines a neighbourhood of the site $\{n\}$. For a pairwise MRF prior, the objective function can be written as

$$\mathbf{x} = \arg \min_{\mathbf{x}} \sum_{n=1}^N l(x_n, y_n) + \sum_{n=1}^N \sum_{l \in \mathcal{N}_n} \Psi(x_n, x_l). \quad (2.130)$$

2.7.3 Graph cut optimization

Graph cut optimization is a standard technique used to solve binary labelling problems in the field of Computer Vision [63, 11]. The optimum solution is found by minimizing an energy function defined on the labels, such as equation (2.130). Given that the labels are discrete, the minimum is found by combinatorial optimization. The *multiway graph cut method* is an extension of graph cuts to a multivariate labelling problem, where $\mathcal{T} = \{1, 2, \dots, j, \dots, J\}$.

A graphical representation is used to describe the neighbourhood system of the image, and the cost assigned to each labelling. A weighted graph $\mathcal{G} = \langle \mathcal{S}, \mathcal{E} \rangle$ is constructed, where \mathcal{S} are the nodes and \mathcal{E} are the connecting edges. The image voxels $\mathcal{V} \subset \mathcal{S}$ are represented by a subset of the nodes. The remaining nodes, known as terminals, correspond to the set of possible label assignments \mathcal{T} for a single voxel. There are two types of edges: N-links connect pairs of neighbouring voxels, as dictated by the neighbourhood system \mathcal{N}_n ; and T-links connect the voxels to the terminals (labels).

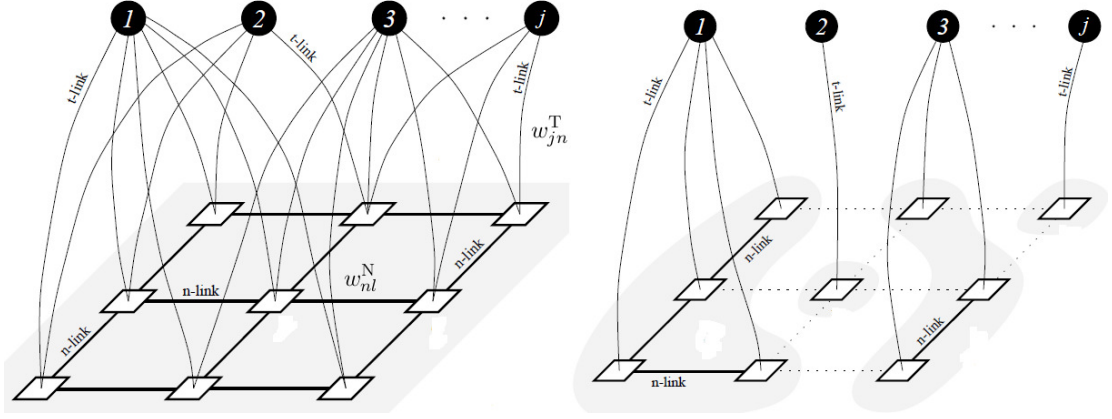


Figure 2.7: Schematic representation of the multiway graph cut optimization method for a 3x3 example: the voxels \mathcal{S} are shown as white squares, and the labels \mathcal{T} as black circles. In the left figure, the graph $\mathcal{G} = \langle \mathcal{S}, \mathcal{E} \rangle$ is shown: each voxel is connected to its neighbours by N-links, and to the labels by T-links (some have been omitted for legibility). In the right figure, the induced graph $\mathcal{G} = \langle \mathcal{S}, \mathcal{E} \setminus \mathcal{C} \rangle$ is shown: the cut corresponds to a labelling where the 1st label is assigned to 4 voxels, the 2nd label to 1 voxel, the 3rd label to 3 voxels and the j th label to 1 voxel. Adapted from [12].

N-links are weighted by the penalty for assigning different labels to the elements, given by the MRF model $w_{nl}^N = \Psi(x_n, x_l)$, where $l(n) \in \mathcal{N}_n$. T-links are weighted by the cost of assigning the relevant label to the pixel, given by the likelihood term $w_{jn}^T = \mathcal{L}(x_j, y_n)$, where $x_j \in \mathcal{T}$.

The key point of the graph cut algorithm is the transformation of the labelling problem into a minimum cut problem. A cut \mathcal{C} is a set of edges such that all the terminals are completely separated in the induced graph $\mathcal{G}(\mathcal{C}) = \langle \mathcal{V}, \mathcal{E} \setminus \mathcal{C} \rangle$, and no subset of \mathcal{C} separates the terminals. The cost of the cut equals the sum of its edge weights:

$$|\mathcal{C}| = \sum_{\{n,l\} \in \mathcal{C}} w_{nl}^N + \sum_{\{j,n\} \in \mathcal{C}} w_{jn}^T, \quad (2.131)$$

where $\{n, l\}$ indicates an N-link, and $\{j, n\}$ a T-link. The minimum cut problem is finding the cheapest amongst all cuts separating the terminals. It is fairly intuitive that each cut represents a potential labelling, by which the voxel is assigned the label corresponding to the terminal to which the voxel is connected (figure 2.7). Furthermore, the value of the energy function (2.130) is equal to the cost of the cut, and the minimum cut uniquely identifies the solution to the labelling problem.

The minimum cut is found by iteratively updating the position of the cut, and calculating the value of the energy function until an approximation of the minimum

is found. Given a label α and subset of voxels $\mathcal{P} \subset \mathcal{V}$, an α -expansion move $x^{\mathcal{P} \leftarrow \alpha}$ is the process by which all voxels in the subset \mathcal{P} acquire the label α . Similarly, an $\alpha\beta$ -swap $x^{\mathcal{P}_{\beta} \leftarrow \alpha}$ is any move by which all voxels with label $\gamma \neq \alpha, \beta$ are left unaltered. The algorithm cycles through the labels and searches for the minimum energy cut within one α -expansion or $\alpha\beta$ -swap move of the current guess. When the minimum is found, it is accepted and the process is repeated for labellings within one move of the new update. The algorithm terminates when the current labelling is a local minimum with respect to α -expansion or $\alpha\beta$ -swap moves: there is no one move that decreases the energy. The efficiency of the algorithm is dependent on the choice of move. The α -expansion algorithm terminates in an order of N iterations (one search per label), whereas the $\alpha\beta$ -swap algorithm terminates in an order of N^2 (one search per pair of labels), therefore the former is more efficient. However, the α -expansion algorithm will find the minimum only if a condition of triangularity (or linearity) is satisfied:

$$\Psi(\alpha, \beta) \leq \Psi(\alpha, \gamma) + \Psi(\gamma, \beta) \quad \forall \alpha, \beta, \gamma \in \mathcal{L}. \quad (2.132)$$

The MRF model, for example, satisfies the linearity condition, and it is more efficient to use the α -expansion algorithm in this case. Details of the implementation, including efficient search of the local minimum and convergence guarantees, are set out in [12].

Chapter 3

Multifrequency EIT using spectral constraints

3.1 Introduction

3.1.1 Overview

In the previous chapter, an introduction to EIT imaging was outlined. Particularly important is the concept of ill-posedness, which explains the difficulty in solving the inverse problem. In order to successfully reconstruct an EIT image, ill-posedness must be overcome via the inclusion of prior information about the solution. Typically, this is achieved by choosing a regularization term defined on the conductivity. Another potential source of information is knowledge of the tissues in the domain and their conductivity. The latter can be obtained, for example, by measuring the conductivity spectrum of tissue samples. In this chapter, a method is developed for including this information in the imaging problem in the form of explicit spectral constraints. The aim is to produce a robust method for static EIT imaging.

3.1.2 Related work

The similarities between imaging modalities allow for the translation to EIT of techniques developed in other fields. Whereas multifrequency EIT is at an early stage of development, an extensive literature has been produced on the related subject of multispectral diffuse optical tomography (DOT). In particular, DOT research has produced methods for directly reconstructing chromophore (light-absorbing substances) concentrations using the wavelength dependence of tissue properties [27]. A similar approach has also been adopted in the field of microwave breast imaging [36].

3.1.3 Purpose

In this chapter, a novel method for using spectral constraints in the inverse problem of MFEIT is formalized, validated and discussed. A *fraction model* for the conductivity is defined, and a nonlinear algorithm for solving the image reconstruction problem is devised. Numerical and experimental results are presented for the case of a cylinder with two tissues. The robustness of the method to errors in the spectral constraints is tested. The performance of the proposed *direct* multifrequency method is compared to an *indirect* approach and to weighted frequency-difference imaging. The case of a four-tissue numerical phantom is considered. Finally, the approximation introduced by the fraction model is investigated and discussed.

3.1.4 Experimental design

3.1.4.1 Fraction reconstruction

A model that relates the conductivity of an object to the conductivity of its component tissues and their relative concentration was defined. The concentration, or *fraction*, values are frequency independent and describe the physical distribution of the tissues. By expressing the inverse problem in terms of the fractions, these can be reconstructed directly. This brings two advantages: 1) all multifrequency data can be used simultaneously, and 2) frequency-difference data can be used. This allows for a more efficient use of the data and the suppression of modelling errors. Images of the fraction values for each tissue were reconstructed using a bounded nonlinear method. Two-tissue numerical and experimental phantoms were constructed and used to validate the method.

3.1.4.2 Robustness to spectral errors

The devised fraction reconstructed is susceptible to uncertainty in the assumed spectral constraints. A numerical study was performed to investigate the robustness of the method to varying degrees of error. The results were compared by an objective image quality evaluation measure. The same comparison method was used throughout.

3.1.4.3 Comparison with existing static EIT methods

A phantom experiment was designed to compare the proposed fraction-based approach to absolute and weighted frequency-difference (WFD) imaging. The purpose of the comparison with absolute imaging was to highlight the advantage in terms of robustness to modelling errors brought by the use of frequency-difference data. The purpose of the comparison with WFD was to highlight the advantage brought by the simultaneous use of all multifrequency data, and to justify the choice of a nonlinear reconstruction

scheme. Success of the WFD algorithm is dependant on the possibility of isolating the contribution on an anomaly from a homogeneous background. A numerical experiment was designed specifically to compare the performance of WFD and fraction imaging in the nonlinear domain, and demonstrate that the application of the fraction reconstruction algorithm is not limited to simple phantoms in the same way as WFD.

3.1.4.4 Comparison with an indirect method

The proposed method involves imaging the fractions directly from all the multifrequency data, without reconstructing the conductivity. An alternative course of action is to reconstruct the absolute conductivity images for each frequency, and then estimate the fractions by fitting the conductivity images to the fraction model. In this case, an optimization problem must be solved for each frequency to reconstruct the conductivity images, and then again to estimate the fractions. Furthermore, the regularization parameter must be estimated separately for each conductivity image, and then again for the fraction image. The proposed fraction reconstruction method was compared to this alternative *indirect* method. A phantom study was designed to investigate the robustness of the respective methods to noise and modelling errors.

3.1.4.5 Multiple tissues case

In order to test the performance of the method in the case of multiple tissues, a four-tissue numerical example was considered.

3.1.4.6 Evaluation of the approximation error

The fraction model, which describes the conductivity in terms of fractions and spectral constraints, introduces an error for all voxels which are occupied by multiple tissues. A numerical experiment was designed to investigate the approximation involved in the fraction model, and determine how the error depends on the number of mixed elements in the mesh.

3.2 Methods

3.2.1 Fraction model

The fraction model is a representation of the conductivity of an object. The model is employed in conjunction with the finite element method (FEM) to approximate a discrete conductivity distribution. It is assumed that the object is composed of a limited number of tissues, and that a volume fraction, or concentration value, can be determined for each component and element of the mesh. The spatial distribution of the tissues is then described by the corresponding fraction distributions. The assumption that

the tissues are homogeneous and have characteristic spectral properties allows for the expression of the conductivity of the object in terms of the conductivity of individual components. For the purpose of generality, the 3D case is examined in the following.

Let us consider a 3D domain on which a frequency dependent conductivity distribution $\sigma(\mathbf{x}, \omega)$ is defined, where \mathbf{x} denotes the spatial coordinates, and ω the frequency. The conductivity is assumed to be static: this is equivalent to assuming that the physical distribution and spectral properties of the object and its components are constant throughout the recording of measurements. A discretization of the domain is performed, and the conductivity is approximated using the FEM to represent an element based, piecewise constant distribution. As a result, the conductivity can be represented by a mesh and a frequency dependent $N \times 1$ vector that determines the value of each element and frequency

$$\boldsymbol{\sigma}(\omega) = [\sigma_n(\omega); n = 1, \dots, N],$$

where N is the number of elements. Time-harmonic currents are injected at the boundary at M frequencies

$$\omega_1, \dots, \omega_i, \dots, \omega_M$$

and K real boundary voltage measurements

$$\mathbf{v}(\omega) = [v_k(\omega); k = 1, \dots, K]$$

are acquired for each frequency.

The following assumptions are made:

1. the domain is composed of a known number J of tissues $t_1, \dots, t_j, \dots, t_J$ with distinct conductivity,
2. the conductivity of each tissue is known for all measurement frequencies

$$\epsilon_{ij} = \sigma^{t_j}(\omega_i),$$

3. the conductivity of the n th element is given by the linear combination of the conductivities of the component tissues

$$\sigma_n(\omega_i) = \sum_{j=1}^J f_{nj} \cdot \epsilon_{ij}, \quad (3.1)$$

where $0 \leq f_{nj} \leq 1$ and $\sum_{j=1}^J f_{nj} = 1$.

Each weighting value f_{nj} of the linear combination is the volume fraction, or concentration, of the j th tissue in the n th voxel. If the n th voxel is occupied only by the j th tissue, then the conductivity is that of the tissue $\sigma(\omega_i) = \epsilon_{ij}$. In this case, $f_{nj} = 1$ and $f_{nl} = 0 \forall l \neq j$. In the case that the voxel lies along a tissue boundary, or is otherwise occupied by a mixture of tissues, the conductivity is approximated by the linear combination of the conductivities of the components, weighted by their fraction values.

Under these assumptions the relationship between conductivity and boundary voltages can be expressed in terms of the matrix $\mathbf{F} = \{\mathbf{f}_1, \dots, \mathbf{f}_j, \dots, \mathbf{f}_J\}$, of dimensions $N \times J$:

$$A(\sigma(\omega_i)) = A\left(\sum_{j=1}^J \mathbf{f}_j \epsilon_{ij}\right) = A(\mathbf{F}). \quad (3.2)$$

The fraction values are independent of frequency and constant across all measurements. Using the chain rule we obtain, for $j = 1, \dots, J$,

$$\frac{\partial A(\sigma_i)}{\partial \mathbf{f}_j} = \frac{\partial A}{\partial \sigma_i} \frac{\partial \sigma_i}{\partial \mathbf{f}_j} = \frac{\partial A}{\partial \sigma_i} \epsilon_{ij} = \mathbf{J}(\sigma_i) \cdot \epsilon_{ij} \quad (3.3)$$

where $\sigma_i = \sigma(\omega_i)$ and $\mathbf{J}(\sigma_i)$ is the Jacobian of the forward map at the frequency ω_i .

3.2.2 Fraction image reconstruction

In analogy with conductivity imaging (2.61), the fraction distributions are reconstructed by minimizing a regularized objective function of the form:

$$\frac{1}{2} \left[\left\| A\left(\sum_j \mathbf{f}_j \epsilon_{ij}\right) - \mathbf{v}(\omega_i) \right\|^2 + \tau \Psi(\mathbf{F}) \right]. \quad (3.4)$$

Using difference data, referred to a chosen frequency ω_0 , the norm of the residual error becomes

$$\frac{1}{2} \left\| A\left(\sum_j \mathbf{f}_j \epsilon_{ij}\right) - A\left(\sum_j \mathbf{f}_j \epsilon_{0j}\right) - (\mathbf{v}(\omega_i) - \mathbf{v}(\omega_0)) \right\|^2. \quad (3.5)$$

If the data is normalized by the reference frequency, which can be advantageous in the case of proportional data noise, then

$$\frac{1}{2} \left\| \frac{A\left(\sum_j \mathbf{f}_j \epsilon_{ij}\right) - A\left(\sum_j \mathbf{f}_j \epsilon_{0j}\right)}{A\left(\sum_j \mathbf{f}_j \epsilon_{0j}\right)} - \frac{\mathbf{v}(\omega_i) - \mathbf{v}(\omega_0)}{\mathbf{v}(\omega_0)} \right\|^2. \quad (3.6)$$

A Markov random field (MRF) regularization term (2.66) of the form

$$\Psi(\mathbf{F}) = \frac{1}{2} \sum_{j=1}^J \sum_{n=1}^N \sum_{l(n)} |f_{nj} - f_{l(n)j}|^2, \quad (3.7)$$

was chosen, where $l(n)$ runs over all neighbours of the n th voxel. A convenient expression for $\Psi(\mathbf{F})$ is obtained by defining the matrix \mathbf{L} as

$$[\mathbf{L}]_{nl} = \begin{cases} N(n) & \text{if } n = l, \\ -1 & \text{if the } n\text{th and } l\text{th elements are neighbours,} \\ 0 & \text{otherwise,} \end{cases} \quad (3.8)$$

where $N(n)$ is the number of neighbours of the n th element. Therefore the regularization term becomes

$$\Psi(\mathbf{F}) = \frac{1}{2} \sum_{j=1}^J \mathbf{f}_j^J \mathbf{L} \mathbf{f}_j. \quad (3.9)$$

Finally, considering all multifrequency measurements simultaneously yields

$$\Phi(\mathbf{F}) = \frac{1}{2} \left[\sum_{i=1}^M \left\| A(\sum_j \mathbf{f}_j \epsilon_{ij}) - A(\sum_j \mathbf{f}_j \epsilon_{0j}) - (\mathbf{v}(\omega_i) - \mathbf{v}(\omega_0)) \right\|^2 + \tau \sum_{j=1}^J \mathbf{f}_j^J \mathbf{L} \mathbf{f}_j \right], \quad (3.10)$$

or for normalized data

$$\Phi(\mathbf{F}) = \frac{1}{2} \left[\sum_{i=1}^M \left\| \frac{A(\sum_j \mathbf{f}_j \epsilon_{ij}) - A(\sum_j \mathbf{f}_j \epsilon_{0j})}{A(\sum_j \mathbf{f}_j \epsilon_{0j})} - \frac{\mathbf{v}(\omega_i) - \mathbf{v}(\omega_0)}{\mathbf{v}(\omega_0)} \right\|^2 + \tau \sum_{j=1}^J \mathbf{f}_j^J \mathbf{L} \mathbf{f}_j \right]. \quad (3.11)$$

The fraction distributions \mathbf{F} are recovered using

$$\mathbf{F} = \arg \min_{\mathbf{F}} \Phi(\mathbf{F}). \quad (3.12)$$

The objective function $\Phi(\mathbf{F})$ is differentiable and the gradient is obtained via the chain rule (3.3).

The constraint $\sum_{j=1}^J f_{nj} = 1 \forall n$ is enforced by substituting $\mathbf{f}_1 = \mathbf{1} - \sum_{j=2}^J \mathbf{f}_j$ in the objective function. The $J - 1$ fraction images, are reconstructed using

$$[\mathbf{f}_2, \dots, \mathbf{f}_J] = \arg \min_{\mathbf{f}_2, \dots, \mathbf{f}_J} \Phi(\mathbf{1} - \sum_{j=2}^J \mathbf{f}_j, \mathbf{f}_2, \dots, \mathbf{f}_J), \quad (3.13)$$

where $0 \leq f_{nj} \leq 1$, and remaining fraction is simply $\mathbf{f}_1 = \mathbf{1} - \sum_{j=2}^J \mathbf{f}_j$.

The reconstruction of $[\mathbf{f}_2, \dots, \mathbf{f}_J]$ was constrained to the closed interval $[0, 1]$ and performed using a two-step algorithm. The initial guess is set to $\mathbf{f}_1 = \mathbf{1}$ and $\mathbf{f}_j = \mathbf{0} \forall j = 2, \dots, J$.

3.2.2.1 Step 1: Gradient projection

Gradient projection [81] is a method for optimizing an objective function with bounded variables. Initially the minimization is set to follow the negative gradient direction $\mathbf{q} = -\nabla\Phi(\mathbf{f}_2^t, \dots, \mathbf{f}_J^t)$, but the search path is projected onto the boundary whenever an upper or lower constraint is encountered. At iteration t , the corners are found by computing the step size values for which each variable reaches a constraint for $j \geq 2$:

$$\bar{\alpha}_{nj} = \begin{cases} \frac{1-f_{nj}^t}{q_{nj}} & q_{nj} > 0, \\ \frac{f_{nj}^t}{q_{nj}} & q_{nj} < 0, \\ \infty & q_{nj} = 0, \end{cases} \quad (3.14)$$

where $\mathbf{F}^t = \{f_{nj}^t\}$ is the previous solution. The step sizes are considered in ascending order. If $\alpha = \{\alpha_m; m = 1, \dots, N \cdot (J-1)\}$ is the sorted vector of positive values of $\bar{\alpha}$, then the intervals $(0, \alpha_1) \dots (\alpha_{m-1}, \alpha_m) \dots (\alpha_{N \cdot (J-1)-1}, \alpha_{N \cdot (J-1)})$ identify the straight sections of the search path. The corners $\tilde{\mathbf{F}}(\alpha_m)$ (points where the search path changes direction) are given by

$$\tilde{\mathbf{f}}_j(\alpha_m) = \tilde{\mathbf{f}}_j(\alpha_{m-1}) + (\alpha_m - \alpha_{m-1}) \mathbf{p}_j^{m-1} \quad 2 \leq j \leq J, \quad (3.15)$$

where

$$\mathbf{p}_{nj}^{m-1} = \begin{cases} q_{nj} & \text{if } \alpha_m < \bar{\alpha}_{nj}, \\ 0 & \text{otherwise,} \end{cases} \quad (3.16)$$

defines the piecewise-linear descent direction. The objective function is approximated along the straight section $[\tilde{\mathbf{F}}(\alpha_{m-1}), \tilde{\mathbf{F}}(\alpha_m)]$ by the quadratic form

$$\begin{aligned} \Phi(\tilde{\mathbf{F}}_2(\alpha)) &= \nabla\Phi(\mathbf{F}^t)^J \cdot (\tilde{\mathbf{F}}_2(\alpha_{m-1}) + \Delta\alpha \mathbf{p}^{m-1}) + \\ &+ \frac{1}{2}(\tilde{\mathbf{F}}_2(\alpha_{m-1}) + \Delta\alpha \mathbf{p}^{m-1})^J \cdot \nabla^2\Phi(\mathbf{F}^t) \cdot (\tilde{\mathbf{F}}_2(\alpha_{m-1}) + \Delta\alpha \mathbf{p}^{m-1}), \end{aligned} \quad (3.17)$$

where $\tilde{\mathbf{F}}_2 = \{\tilde{\mathbf{f}}_2, \dots, \tilde{\mathbf{f}}_J\}$, $0 < \Delta\alpha < \alpha_m - \alpha_{m-1}$, and the Hessian matrix $\nabla^2\Phi(\mathbf{F}^t)$ is approximated using the Gauss-Newton form by disregarding the second order derivative

of the residual error (section 2.5.4.2). The minimum point is found by differentiating (3.17) with respect to $\Delta\alpha$ along each straight interval of the search path in sequence, and equating to zero. If the result $\Delta\alpha^*$ is included in the interval $[\alpha_{m-1}, \alpha_m)$ then the minimum,

$$\tilde{\mathbf{F}}_2 = \tilde{\mathbf{F}}_2(\alpha_{m-1}) + \Delta\alpha^* \mathbf{p}^{m-1}, \quad (3.18)$$

is accepted. Otherwise the next interval is considered, and the process is repeated until the minimum is found. The result of the gradient projection step is the Cauchy point $\tilde{\mathbf{F}} = [\tilde{\mathbf{f}}_1, \tilde{\mathbf{f}}_2, \dots, \tilde{\mathbf{f}}_J]$.

3.2.2.2 Step 2: Damped Gauss-Newton using a Krylov solver

The components of the Cauchy point that coincide with the constraints define the inactive sets for the second step. These are fixed to the boundary value (0 or 1) and the subproblem of solving for all other components is considered. Initially the constraints are ignored, one step of a damped Gauss-Newton method is performed, then the solution is projected back onto the boundary.

The search direction \mathbf{d}^t at iteration t is calculated by solving

$$\nabla^2\Phi(\tilde{\mathbf{f}}_2, \dots, \tilde{\mathbf{f}}_J) \cdot \mathbf{d}^t = -\nabla\Phi(\tilde{\mathbf{f}}_2, \dots, \tilde{\mathbf{f}}_J) \quad (3.19)$$

for the components with non-active sets. Given the size of the problem, the approximated Hessian is never formulated explicitly and equation (3.19) is solved using generalized minimal residuals (GMRes) [95] (section 2.5.4.2). The minimization step size β^t is computed using the Brent line-search method [15], and the Brent abscissae are found via a gold-section bracketing loop [123] (section 2.5.4.5). The result of the damped Gauss-Newton step is

$$\mathbf{F}^+ = \begin{cases} \mathbf{1} - \sum_{j=2}^J (\tilde{\mathbf{f}}_j + \beta^t \cdot \mathbf{d}_j^t) & j = 1 \\ \tilde{\mathbf{f}}_j + \beta^t \cdot \mathbf{d}_j^t & 2 \leq j \leq J \end{cases} \quad (3.20)$$

and the proposed solution is given by

$$\mathbf{f}_{nj}^{t+1} = \begin{cases} 0 & \text{if } \tilde{\mathbf{f}}_{nj} = 0 \text{ or } \mathbf{f}_{nj}^+ \leq 0, \\ 1 & \text{if } \tilde{\mathbf{f}}_{nj} = 1 \text{ or } \mathbf{f}_{nj}^+ \geq 1, \\ \mathbf{f}_{nj}^+ & \text{otherwise.} \end{cases} \quad (3.21)$$

The solution is accepted if $\Phi(\mathbf{F}^{t+1}) \leq \Phi(\tilde{\mathbf{F}}) \leq \Phi(\mathbf{F}^t)$. If only $\Phi(\tilde{\mathbf{F}}) \leq \Phi(\mathbf{F}^t)$ then the Cauchy point is accepted.

3.2.2.3 Fraction reconstruction algorithm outline

```

Initialize  $t = 0$ ,  $\mathbf{f}_1 = \mathbf{1}$ ,  $\mathbf{f}_j = \mathbf{0} \ \forall j = 2, \dots, J$ 
set  $tol$  and  $maxit$ 
repeat
  find Cauchy point  $\tilde{\mathbf{F}}$  using gradient projection (3.18)
  solve (3.19) to find  $\mathbf{d}^t$ 
  find  $\beta_t$  that minimizes  $\Phi(\tilde{\mathbf{f}}_j + \beta^t \mathbf{d}_j^t; j = 2, \dots, J)$ 
  compute  $\mathbf{F}^+$  using (3.20)
  set  $\mathbf{F}^{t+1}$  using (3.21)
   $t = t + 1$ 
until  $|\Phi(\mathbf{F}^{t+1}) - \Phi(\mathbf{F}^t)| \leq tol$  or  $t = maxit$ 
return  $\mathbf{F}$ 

```

3.2.3 Fraction image reconstruction: indirect method

An alternative method for estimating the tissue fractions indirectly is by fitting the absolute conductivity images (Figure 3.1). First, the conductivity images at each frequency $\{\sigma_i; i = 1, \dots, M\}$ are obtained by minimizing,

$$\sigma_i = \arg \min_{\sigma_i} \frac{1}{2} \left[\|A(\sigma_i) - \mathbf{v}_i\|^2 + \tau_i \sum_{n=1}^N \sum_{l(n)} |\sigma_{ni} - \sigma_{l(n)i}|^2 \right], \quad (3.22)$$

using a non-linear Gauss-Newton-Krylov algorithm [53] (section 2.5.4.2). The regularization parameters τ_i are optimized for each frequency.

An *indirect* fraction image $\hat{\mathbf{F}} = [1 - \sum_{j=2}^J \hat{\mathbf{f}}_j, \hat{\mathbf{f}}_2, \dots, \hat{\mathbf{f}}_J]$ is computed by minimizing

$$\frac{1}{2} \left[\sum_{i=1}^M \left\| \sigma_i - \left(\mathbf{1} \cdot \epsilon_{i1} + \sum_{j=2}^J \hat{\mathbf{f}}_j \cdot (\epsilon_{ij} - \epsilon_{i1}) \right) \right\|^2 + \xi \sum_{j=1}^J \sum_{n=1}^N \sum_{l(n)} |\hat{f}_{nj} - \hat{f}_{l(n)j}|^2 \right], \quad (3.23)$$

where ξ is the regularization parameter. The minimization is performed, as for the proposed direct method, by alternating steps of gradient projection and damped Gauss-Newton.

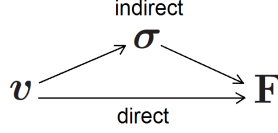


Figure 3.1: Schematic comparison between direct and indirect fraction reconstruction methods.

3.2.4 Image quantification

In evaluating experimental results, image quality was assessed on the basis of an objective quantification method. The case is considered of resolving a perturbation tissue t_2 from a homogeneous background tissue t_1 , by reconstructing an image of the fraction f_2 . The reconstructed perturbation was identified as the largest connected cluster of voxels with values larger than 50% of the maximum displacement from the mean value of the image [35, 83]. Three measures of image quality were devised.

1. Image noise: inverse of the contrast-to-noise ratio (CNR) between the real perturbation Σ and the background

$$\frac{\sqrt{\frac{1}{N^B-1} \sum_{n \notin \Sigma} (f_{n2} - \bar{f}_2^B)^2}}{|\bar{f}_2^P - \bar{f}_2^B|}, \quad (3.24)$$

where \bar{f}_2^P and \bar{f}_2^B are the mean intensities of the real perturbation and background, and N^B is number of elements of the background.

2. Localization error: ratio between the norm of the x-y displacement of the centre of mass of the reconstructed perturbation Σ' from the real position (x, y) , and the diameter of the mesh d

$$\frac{\|\sum_{n \in \Sigma'} f_{n2} \cdot (x_n, y_n) - (x, y)\|}{d}, \quad (3.25)$$

where (x_n, y_n) is the x-y position of the centre of the n th tetrahedron.

3. Shape error: mean ratio of the difference between the dimensions of the real and reconstructed perturbations, respectively (l_x, l_y, l_z) and (l'_x, l'_y, l'_z) , and the diameter of the mesh

$$\frac{1}{3} \left(\frac{|l_x - l'_x|}{d} + \frac{|l_y - l'_y|}{h} + \frac{|l_z - l'_z|}{h} \right), \quad (3.26)$$

where h is the height of the mesh. The size of the simulated and reconstructed perturbation was estimated by taking the maximum coordinate difference be-

tween voxels coinciding with the perturbation. In the experimental case, the real dimensions of the perturbation were measured using a calliper.

3.3 Results

3.3.1 Tissue impedance spectra

The conductivity spectra of the test tissues were obtained empirically from tissue samples. Resistance measurements were acquired with a Hewlett-Packard 42847A (Hewlett-Packard, CA, USA) impedance analyser for 48 frequencies in the range 20 Hz – 1 MHz using Ag-AgCl electrodes.

Biological test objects with frequency dependent conductivities were used to mimic the properties of live tissues [83, 3, 58]. The background medium was a mixture of 0.1% concentration NaCl solution and carrot cubes of approximately 4 mm per side. Two samples were measured using Perspex tubes of fixed diameter (1.6 cm) and variable length (4.6 and 7.5 cm). A perturbation was obtained from a potato segment of diameter approximately 4.6 cm. The resistivities of the full length (10.6 cm) and partial length (5.4 cm) were measured. The test object was immersed in saline for 45 minutes before starting the recordings in order to reduce drift. The electrode resistance was estimated and subtracted by plotting resistance against length for each tissue and evaluating the offset of the line passing through the measurement points. The conductivities of the carrot-saline background and potato perturbation rose monotonically from 0.1 S/m and 0.02 S/m at 20 Hz to 0.3 S/m and 0.4 S/m at 1 MHz.

These results were used to simulate realistic data and to reconstruct fraction images from experimental EIT recordings made with the UCLH Mk. 2.5 EIT system. The conductivity values for 16 amongst the output frequencies of the UCLH system in the range 640 Hz – 1.29 M Hz were estimated from the spline of the sample measurements (figure 3.2).

3.3.2 Numerical Validation

Numerical validation of the fraction reconstruction method was performed on synthetic data. Boundary voltages were simulated using a cylindrical mesh of diameter 19 cm and height 10 cm, with 62 784 elements and a ring of 32 electrodes around the centre. A current of peak amplitude 133 μ A, injected through polar electrodes, was simulated. For each injection pair, the difference between voltages on all adjacent pairs of electrodes not involved in delivering the current was considered, for a total of 448 measurements per frequency. The ground point was fixed at the centre of the bottom of the mesh. The

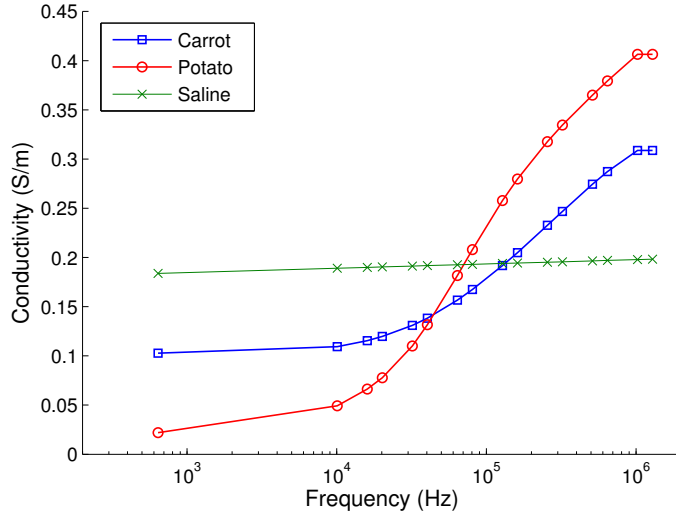


Figure 3.2: Conductivity values of test tissues obtained from sample measurements at 16 output frequencies of the UCLH Mk 2.5 multifrequency EIT system in the range 640 Hz – 1.29 M Hz.

electrode impedance was set to 1 k Ω and the complete electrode model was employed [104] (section 2.4.4).

A cylindrical perturbation of diameter 4.6 cm and height 10 cm was placed in (-4 cm 0 cm 0 cm) (position 1) and (0 cm +4 cm 0 cm) (position 2), where the origin is the centre of the tank (figure 3.3). The background and perturbation conductivities were set to the values for saline-carrot and potato obtained empirically for 16 output frequencies of the UCLH Mk 2.5 system. Frequency-difference data normalized to the lowest frequency (640 Hz) was used. Proportional 0.1% white Gaussian noise was added to the absolute boundary voltages. The noise level was chosen under consideration that the expected change across frequencies in boundary voltages is in the order of 1%, therefore a high level of precision must be achieved in measuring the absolute values with an EIT system. The regularization parameter was set using the L-curve method [42] (section 2.5.7). Fraction images were reconstructed using all multifrequency data by performing four iterations of the proposed nonlinear fraction reconstruction method (figure 3.4).

3.3.3 Robustness to spectral errors

A simulation study was performed to determine the robustness of the fraction reconstruction method to errors in the assumed tissue spectra $\epsilon_j = \{\epsilon_{ij}; i = 1, \dots, M\}$. The same mesh, electrodes, measurement protocol and perturbation were chosen as in the previous section. A random error was added to the tissue spectra of carrot (ϵ_1) and

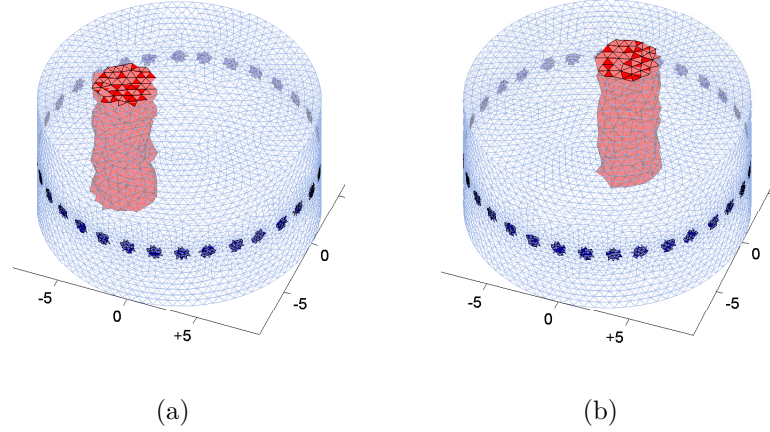


Figure 3.3: Numerical validation model: (a) position 1 (-4 cm 0 cm 0 cm), (b) position 2 (0 cm +4 cm 0 cm).

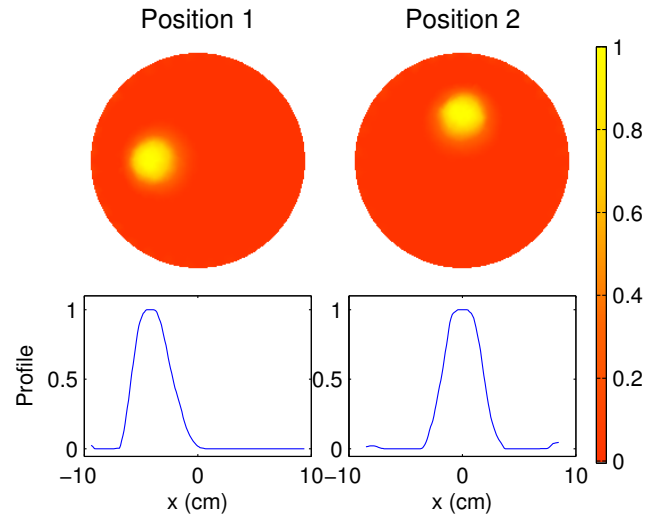


Figure 3.4: Numerical validation results: perturbation fraction images of positions 1 and 2. In all images the raster of the central slice ($z = 0$, thickness 2 cm) is displayed and, where relevant, profile plots at $y = 0$ cm for position 1 and $y = +4$ cm for position 2 were plotted. The scale is the volume fraction value (between 0 and 1).

potato (ϵ_2), before producing a conductivity model:

$$\sigma_{ni}^* = \begin{cases} \epsilon_{i1} + h_{i1} & \text{on the background,} \\ \epsilon_{i2} + h_{i2} & \text{on the perturbation,} \end{cases} \quad (3.27)$$

where $h_{ij} \sim \mathcal{N}(\epsilon_{ij}, \epsilon_{ij} \cdot \Sigma)$ is a random number drawn from the normal distribution \mathcal{N} with mean ϵ_{ij} and variance $\epsilon_{ij} \cdot \Sigma$. The values $\epsilon_{ij} + h_{ij}$ represent the real, unknown conductivities of the tissues, and the mean conductivities ϵ_{ij} the inexact measurements

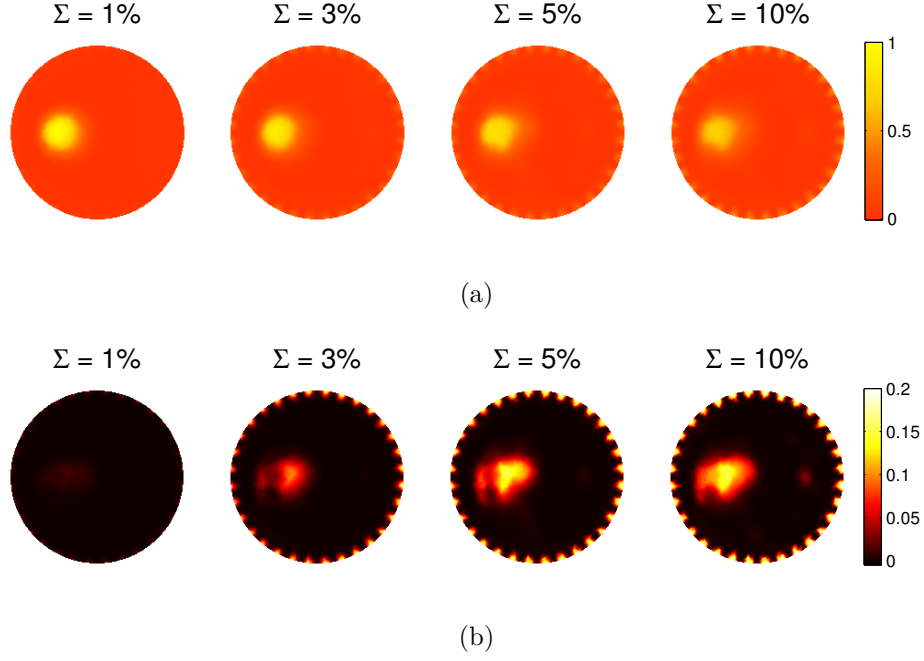


Figure 3.5: Robustness to spectral errors: (a) mean and (b) standard deviation of the reconstructed fraction images for each choice of the spectral variance Σ . The scale is the volume fraction value (between 0 and 1).

obtained from the samples.

Boundary voltage data was simulated using the model σ^* , and fraction images were reconstructed using the original measured spectra. The process was repeated 20 times for each choice of $\Sigma = 1\%$, 3% , 5% , 10% . The regularization parameter was set to $\tau = 10^{-3}$, and the number of iterations was 4 in all cases.

The results were evaluated by computing the ratio of the L^2 -norm of the distance between the reconstructed image and the true solution, and the L^2 -norm of the true solution. To make the error measure independent of the number of tissues, the mean was taken:

$$\text{Err}_{L^2} = \frac{1}{T} \sum_{j=1}^T \frac{\|\mathbf{f}_j^{\text{recon}} - \mathbf{f}_j^{\text{true}}\|}{\|\mathbf{f}_j^{\text{true}}\|}, \quad (3.28)$$

where

$$\mathbf{f}_2^{\text{true}} = \begin{cases} 0 & \text{on the background,} \\ 1 & \text{on the perturbation,} \end{cases} \quad (3.29)$$

and $\mathbf{f}_1^{\text{true}} = \mathbf{1} - \mathbf{f}_2^{\text{true}}$.

The mean and the standard deviation of the reconstructed images (Figures 3.5a and 3.5b), and the mean image quantification measures (Figure 3.6) were computed.

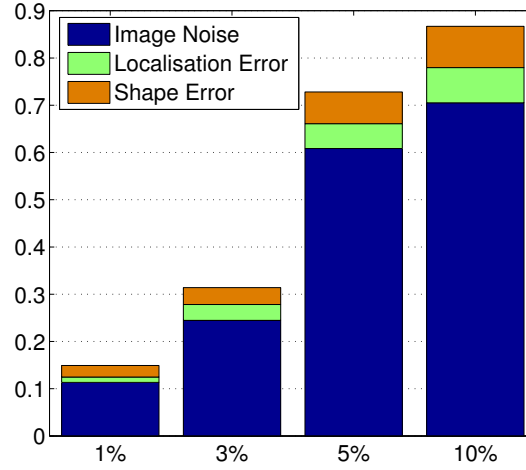


Figure 3.6: Robustness to spectral errors: mean image quantification results over 20 repetitions for each choice of Σ .

Σ	1%	3%	5%	10%
$mean(\text{Err}_{L^2})$	1.17%	1.88%	2.87%	3.09%
$var(\text{Err}_{L^2})$	$4.4 \cdot 10^{-6}$	$7.2 \cdot 10^{-5}$	$2.6 \cdot 10^{-4}$	$2.3 \cdot 10^{-4}$

Table 3.1: Robustness to spectral errors: mean and standard deviation over 20 repetitions of image error Err_{L^2} for several choices of spectral variance Σ .

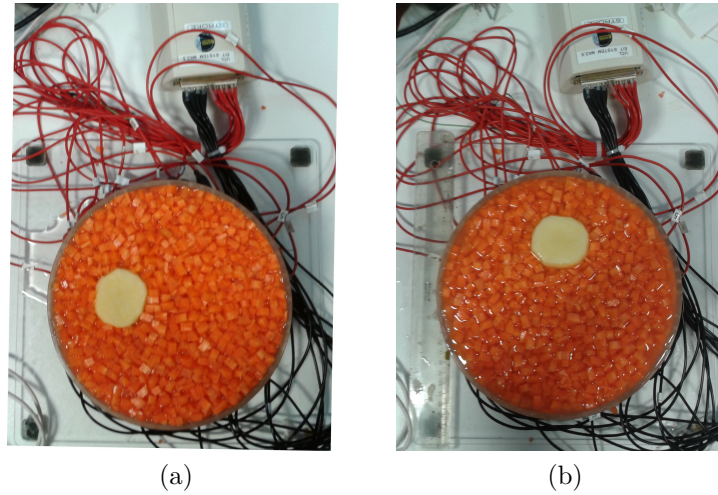


Figure 3.7: Phantom experiment setup: (a) position 1 (-4 cm 0 cm 0 cm), (b) position 2 (0 cm $+4$ cm 0 cm).

3.3.4 Phantom study

A phantom study was designed to reproduce the experimental setup rendered previously in simulation. The phantom was built using the test tissues measured with the impedance analyser, and a perspex cylindrical tank of diameter 19 cm and height 10 cm. The

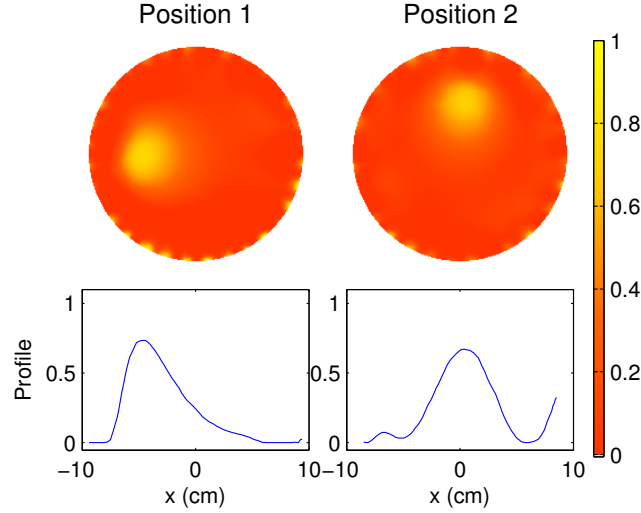


Figure 3.8: Phantom experiment fraction images: perturbation fraction images of positions 1 and 2. The scale is the volume fraction value (between 0 and 1).

tank was filled with a mixture of 0.1% concentration saline solution and carrot cubes of approximately 4 mm side. A potato with a diameter of approximately 4.6 cm and length 10 cm was placed first in position $(-4 \text{ cm } 0 \text{ cm } 0 \text{ cm})$ (figure 3.7a), and then in $(0 \text{ cm } +4 \text{ cm } 0 \text{ cm})$ (figure 3.7b). A ring of thirty-two silver electrodes with 1 cm diameter was placed around the tank and a 33rd electrode was used to fix the ground at the centre of the base. Measurements were recorded using the UCLH Mark 2.5 MFEIT system at 16 frequencies in the range 640 Hz – 1.29 MHz. A current of amplitude 133 μA was injected at polar electrode pairs and voltages were acquired at all adjacent channels not involved in the current injection. The data was averaged over 10 frames and referred to the lowest frequency (640 Hz). Images were reconstructed using the same mesh employed in validating the method. In the following, unless otherwise specified, the regularization parameter was selected using the L-curve method, and the number of iterations for nonlinear methods was set to 4. The electrode contact impedance was assumed to be 1 k Ω , which is the upper limit of the real value, and constant across all electrodes and frequencies.

Fraction images were reconstructed using the proposed method from all multifrequency data (figure 3.8).

3.3.5 Comparison with indirect multifrequency imaging

Fraction images were obtained from the multifrequency phantom data using the indirect method described previously (section 3.2.3). Absolute conductivity values were recovered for each measurement frequency (figures 3.9a and 3.9b) and fraction images were

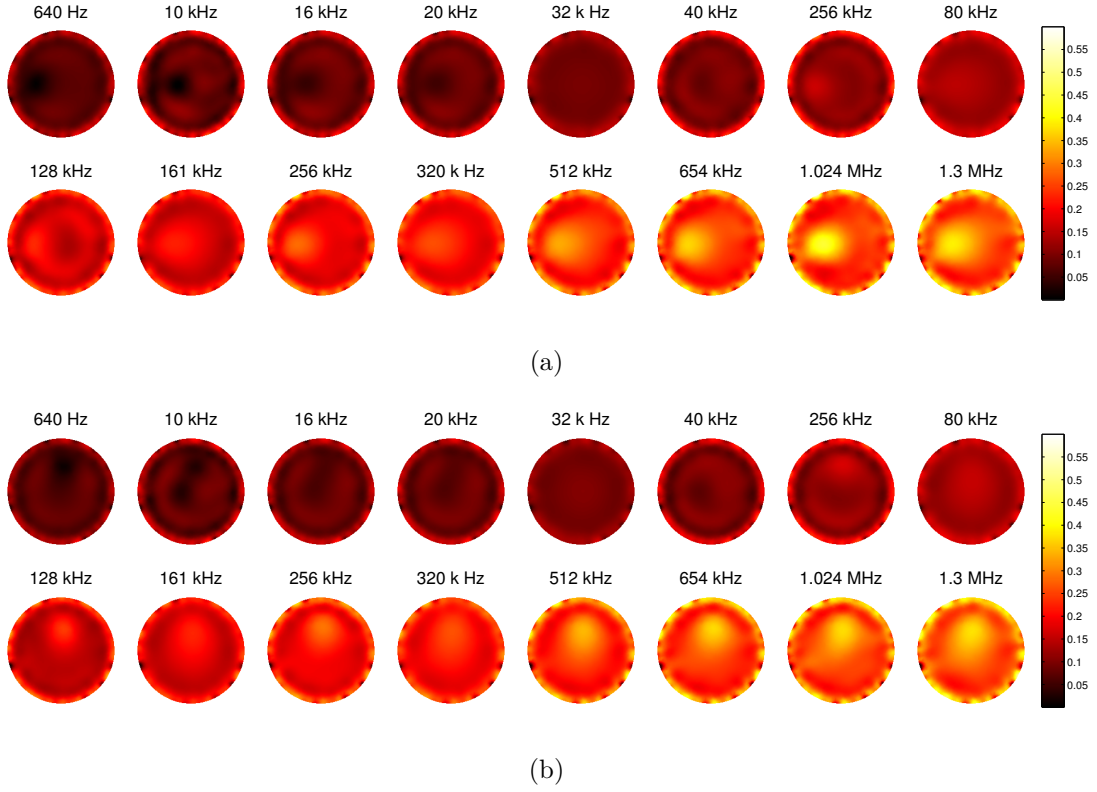


Figure 3.9: Absolute conductivity images of the experimental phantom for each measurement frequency: (a) position 1 and (b) position 2. The scale is conductivity (S/m).

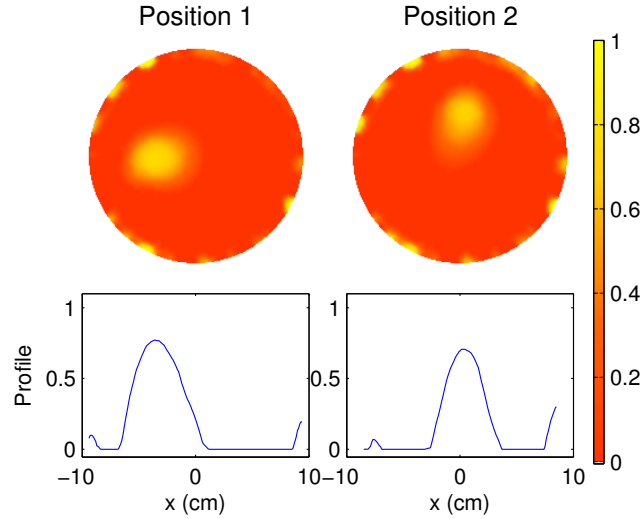


Figure 3.10: Indirect multifrequency imaging results: indirect fraction images of the experimental phantom for positions 1 and 2. The scale is the volume fraction value (between 0 and 1).

obtained from these (figure 3.10). The fraction images obtained with the direct and indirect method and the conductivity images were compared using an objective image quantification method (Figures 3.11a and 3.11b).

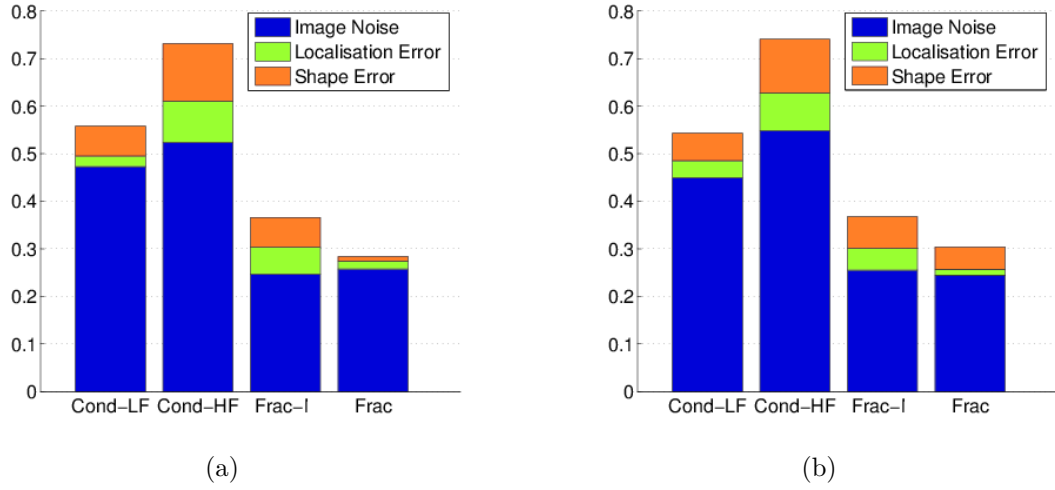


Figure 3.11: Comparison of image quantification results for absolute conductivity images at 640 Hz (Cond-LF) and 1.2 MHz (Cond-HF), indirect (Frac-I) and direct (Frac) fraction images: (a) position 1, (b) position 2.

3.3.6 Comparison with weighted frequency-difference conductivity imaging

The weighted frequency-difference (WFD) algorithm uses a weighted difference in boundary voltages between two frequencies $\mathbf{v}_i - \delta_i \mathbf{v}_0$ and a linear method to reconstruct a weighted conductivity difference $\sigma_0 - \delta_i \sigma_i$, where $\delta_i = \frac{\langle \mathbf{v}(\omega_i), \mathbf{v}(\omega_0) \rangle}{\langle \mathbf{v}(\omega_0), \mathbf{v}(\omega_0) \rangle}$ (section 2.6.3). WFD conductivity images were reconstructed from the tank data for each frequency and compared to fraction images (figures 3.12a and 3.12b). The lowest frequency ($\omega_0 = 640$ Hz) was used as a reference and the reconstruction was performed using generalized tSVD and MRF regularization (section 2.5.3.1), and the image quantification measures were computed (figures 3.13a and 3.13b).

3.3.7 Spectral constraints method for nonlinear case

In order to investigate further applications of WFD and the fraction method, two conductivity distributions that violate the assumptions of WFD were simulated (figure 3.14a and 3.14b). As before, the measured spectral values of the saline-carrot and potato samples were used to simulate boundary voltage measurements, and 0.1% white Gaussian noise was added to the data. The lowest frequency (640 Hz) was used as a reference. Fraction and WFD conductivity images were reconstructed (figures 3.15, 3.16a and 3.16b).

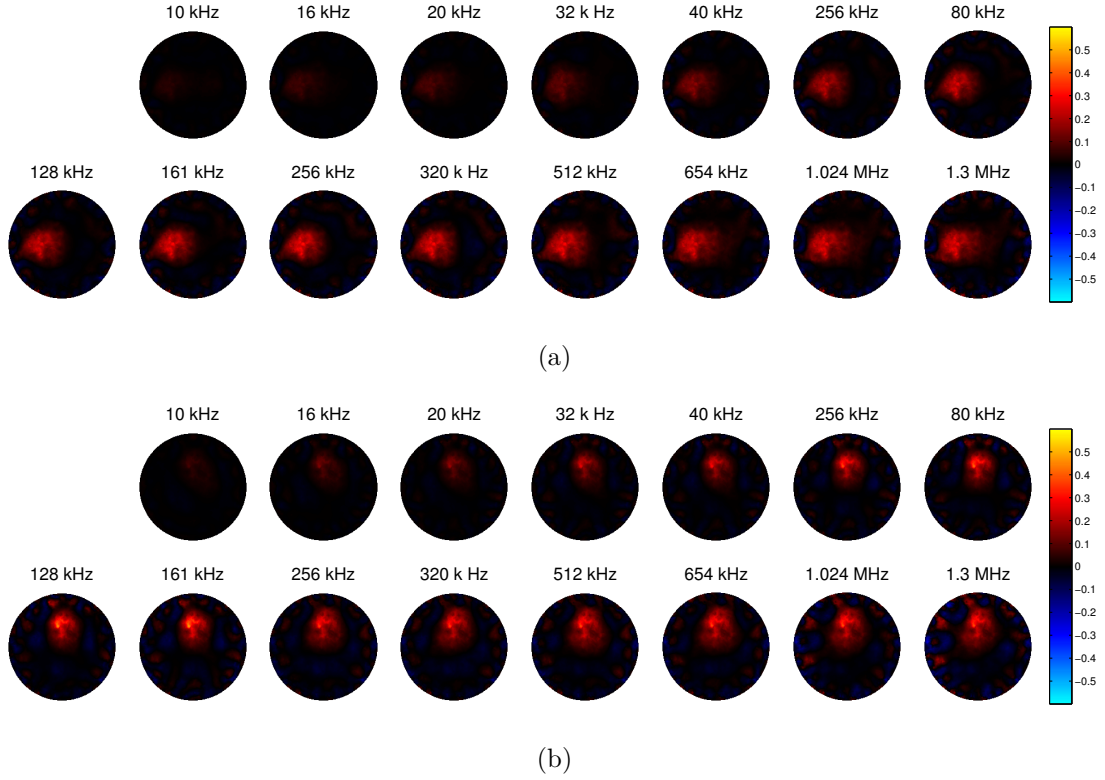


Figure 3.12: WFD conductivity images of the experimental phantom for each measurement frequency: (a) position 1 and (b) position 2. The scale is weighted conductivity difference (S/m).

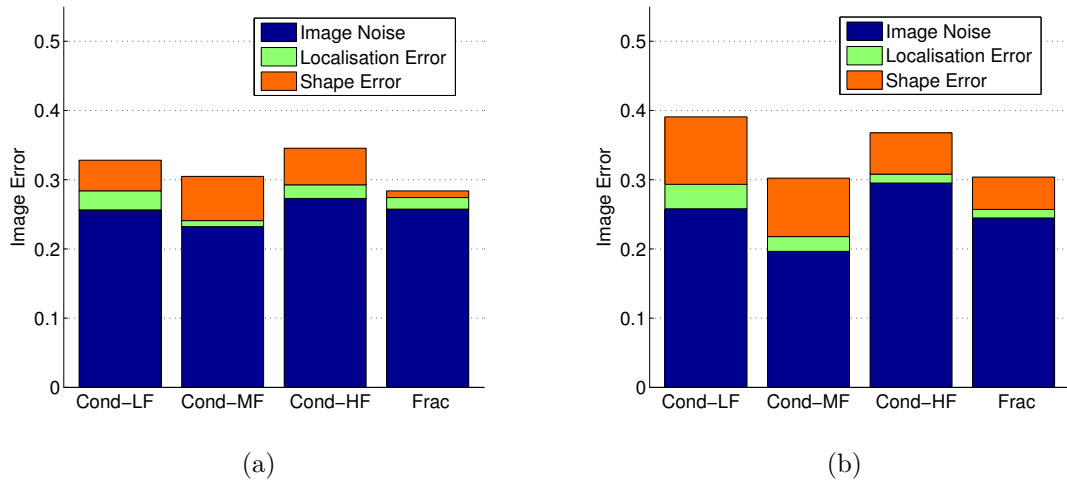


Figure 3.13: Comparison of image quantification results for WFD conductivity images at 640 Hz (Cond-LF), 128 kHz (Cond-MF) and 1.2 MHz (Cond-HF), and fraction image (Frac): (a) position 1 and (b) position 2.

3.3.8 Multiple tissue case

A numerical phantom with 4 tissues was constructed. The inclusions were positioned in (0.87 cm 4.92 cm), (-4.7 cm -1.71 cm), and (3.83 cm -3.21 cm). The background tissue

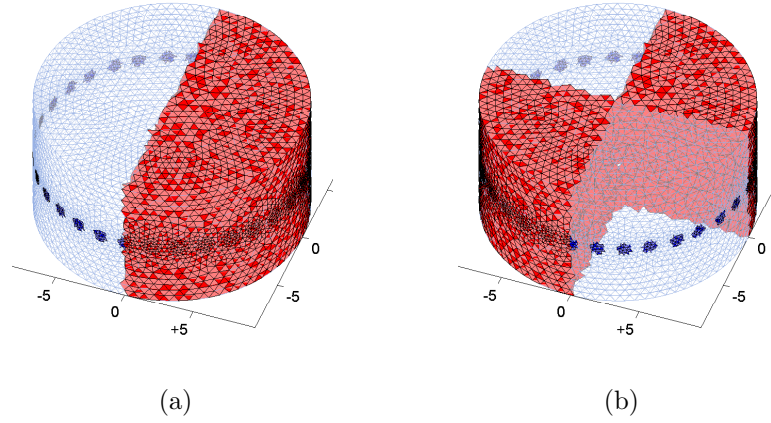


Figure 3.14: WFD comparison simulation model: (a) position A, (b) position B.

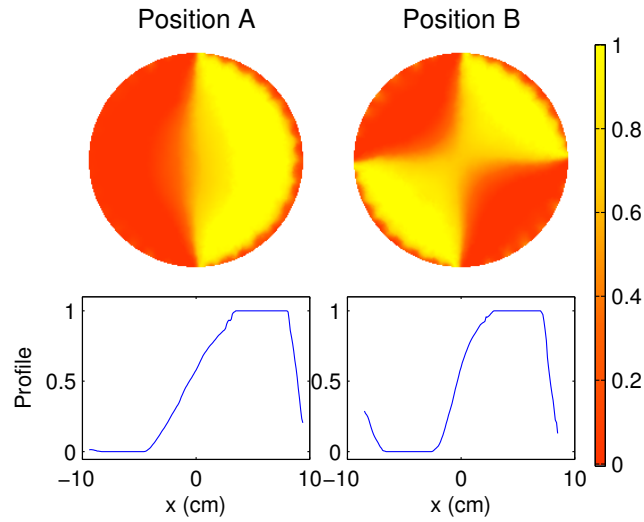


Figure 3.15: WFD comparison simulation fraction images: perturbation fraction images of position A and B. The scale is the volume fraction value (between 0 and 1).

was a mixture of 0.1% concentration saline and carrot pieces, and the inclusions were composed of, respectively, potato, banana and cucumber (figure 3.18). The tissue spectra were obtained using the method and instrumentation described in section 3.3.1 (figure 3.17). Data was simulated using the same mesh, electrode positions, measurement protocol and frequencies as in 3.3.2. Fraction images were reconstructed for each tissue (figure 3.19) using the proposed method. The regularization parameter was chosen by visual inspection, and the number of iterations was set to 10.

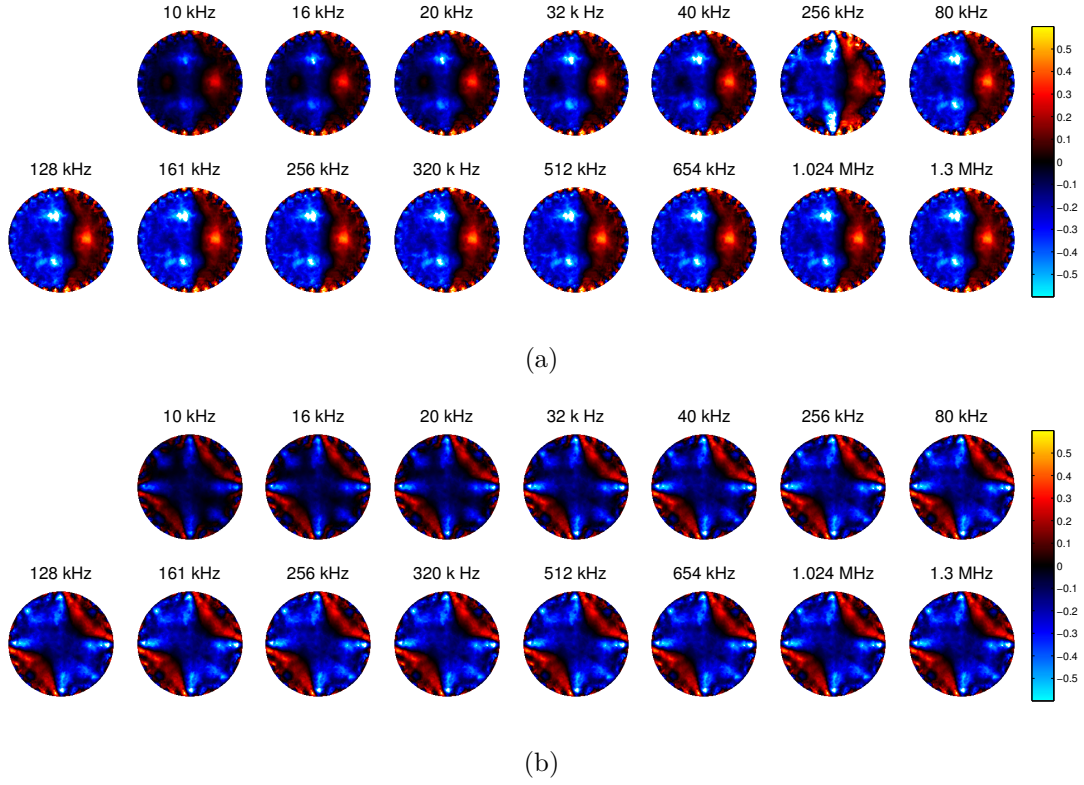


Figure 3.16: WFD comparison simulation conductivity images: (a) WFD conductivity image of position A, (b) WFD conductivity image of position B. The scale is weighted conductivity difference (S/m).

3.3.9 Approximation error evaluation

A simulation study was performed to investigate the approximation introduced by the fraction model in representing the conductivity of an object. A sphere was simulated using a fine tetrahedral mesh of diameter 10 cm with 130 144 tetrahedral elements (figure 3.20b). A conductivity distribution σ^f was drawn from the binomial distribution $p(\sigma^f) \sim \mathcal{B}(\epsilon_1, \epsilon_2)$, where $\epsilon_1 = 0.11$ and $\epsilon_2 = 0.05$ are approximately the conductivities of saline-carrot mixture and potato at 10 kHz.

A conformal mesh with 16 268 ($=130\,144/8$) elements (figure 3.20a) was used to define a second conductivity distribution σ^c . The two meshes were chosen so that each tetrahedra of the coarse mesh would contain 8 tetrahedra of the fine mesh, and each surface triangle of the coarse mesh would contain 4 triangles of the fine mesh. The conductivity of each element of the coarse mesh was obtained via linear combination of

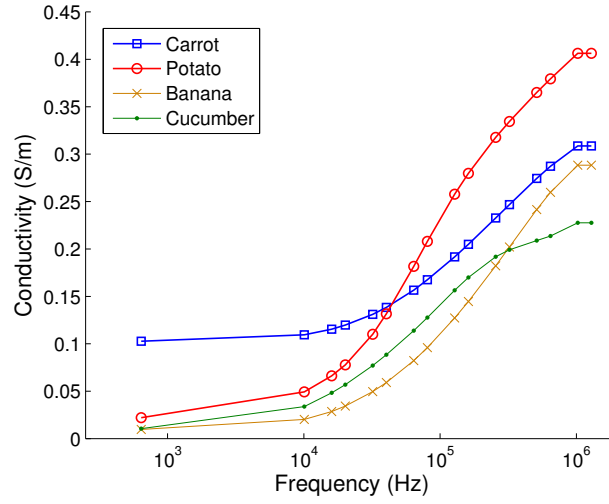


Figure 3.17: Four-tissue case model: conductivity values of carrot-saline, potato, banana and cucumber obtained from sample measurements.

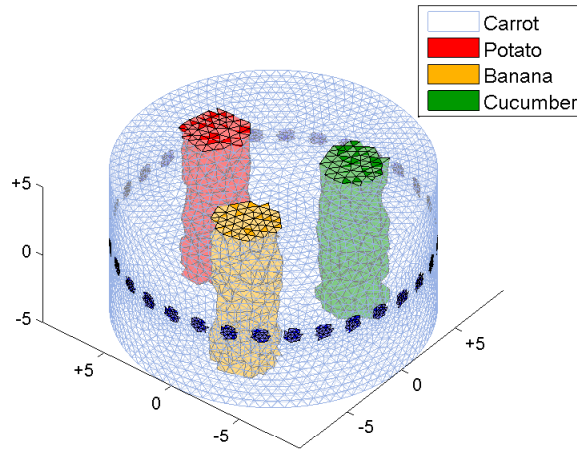


Figure 3.18: Four-tissue case model: numerical phantom model, scale is cm.

the values of the corresponding elements of the fine mesh using the fraction model:

$$[\sigma^c]_n = \frac{\sum_{l=1}^8 \sigma_{n_l}^f \cdot \Gamma_{n_l}}{\Gamma_n}, \quad (3.30)$$

where Γ indicates the volume of the element. The volume fraction of each tissue is consequently

$$\mathbf{f}_j = \sum \Phi_{n_l}^{(j)} / \Phi_n \quad (3.31)$$

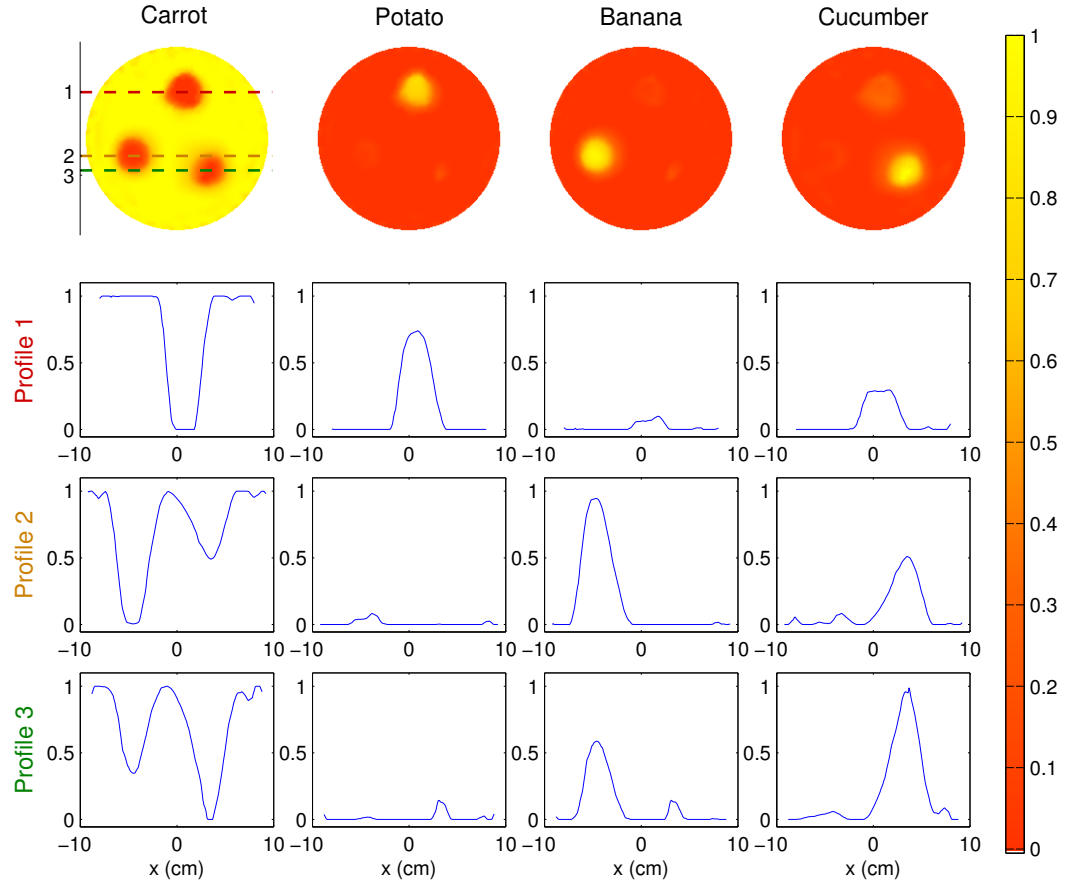


Figure 3.19: Four-tissue case fraction images: reconstructed fraction images and profile plots at $y = +4.92$ cm (1), $y = -1.71$ cm (2) and $y = -3.21$ cm (3). The scale is the volume fraction value (between 0 and 1).

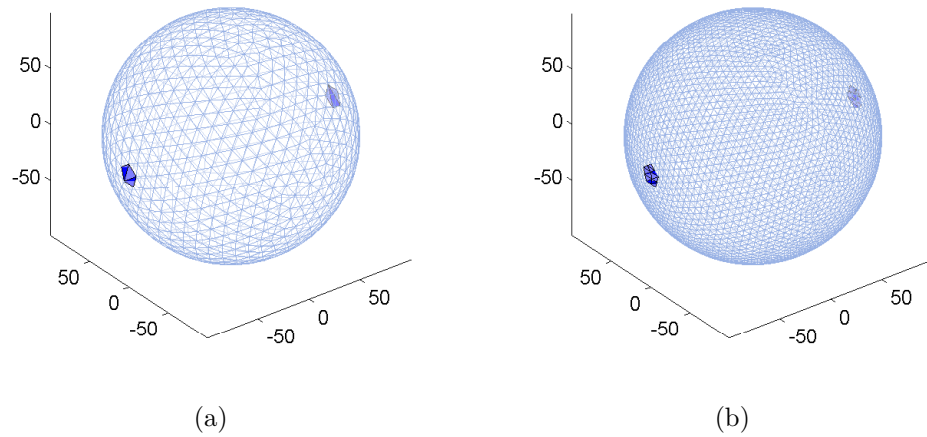


Figure 3.20: Approximation error evaluation model: (a) coarse mesh, 16,268 elements, (b) fine mesh, 130,144 elements. Units mm, diameter 10 cm.

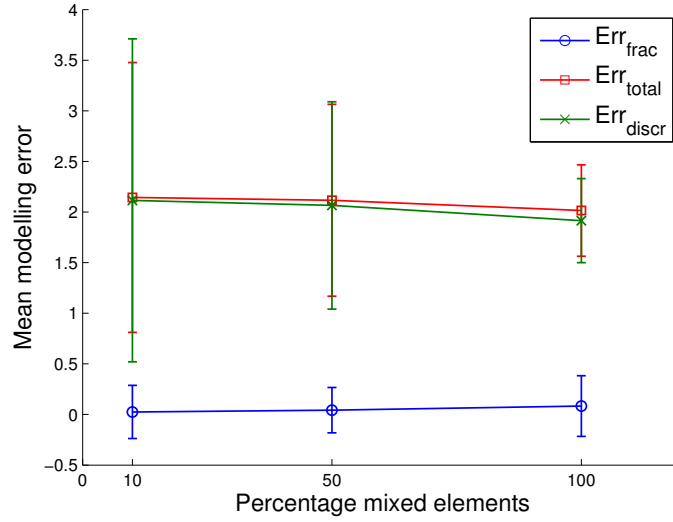


Figure 3.21: Mean approximation error introduced by the fraction model (Err_{frac}), the FEM ($\text{Err}_{\text{discr}}$) and both methods ($\text{Err}_{\text{total}}$) in estimating boundary voltages for 10 %, 50 % and 100 % mixed elements in a coarse mesh.

where the sum is over the elements in the fine mesh assigned to the tissue j and for which $\sigma_{n_l} = \epsilon_j$. The indexes n_1, \dots, n_8 of the elements of the fine mesh that make up each element of the coarse mesh were found using the Matlab function `inhull(testpnts, xyz)`, which determines if the points `testpnts` are inside the convex hull of vertices `xyz`.

Finally, the values of σ^c were distributed on the fine mesh to generate a third conductivity distribution

$$\sigma^{f*} = \{\sigma_{n_l} : \sigma_{n_l} = [\sigma^c]_n, l = 1, \dots, 8\}. \quad (3.32)$$

The boundary conditions were set by simulating two electrodes in polar position. The electrode shape was chosen in order to maintain the same electrode area in the coarse and fine mesh. The radius of the circle circumscribing each electrode was 1 cm. A current of peak amplitude $+133\mu\text{A}$ was simulated on one electrode, and the other was used as ground. The electrode contact impedance was set at 1 k Ω and the complete electrode model was employed.

The boundary voltages v^c , v^f were generated, and v^{f*} was obtained from the conductivity distributions defined above. The total modelling error $\text{Err}_{\text{total}} = |v^f - v^c|$ between the representations of σ^f and σ^c , and the discretization error $\text{Err}_{\text{discr}} = |v^{f*} - v^c|$ between the representations of σ^{f*} and σ^c were considered. In order to evaluate the error introduced by the fraction model in estimating v_c , the percentile difference between

the total and discretization error was considered

$$\text{Err}_{\text{frac}} = \frac{\text{Err}_{\text{total}} - \text{Err}_{\text{discr}}}{v^c} \cdot 100. \quad (3.33)$$

The random distribution σ^f was drawn and the fraction error was calculated 100 times. The procedure was repeated after reducing the proportion of mixed elements in the coarse mesh from 100% to 50% and 10% (Figure 3.21). In order to achieve this, the values of the correct proportion of elements of the fine mesh were assigned at random and the remaining were considered in homogeneous groups of 8, each corresponding to an element of the coarse mesh.

3.4 Discussion

3.4.1 Robustness to spectral errors

The fraction model assumes exact knowledge of the impedance spectra of all tissues in the domain. For the purposes of this study, these were evaluated by measuring the conductivity of tissue samples with an impedance analyser, as described in section 3.3.1. It is unavoidable that these measurements are affected by noise and experimental error, and the tissue spectra employed in the reconstruction scheme are to a certain degree, incorrect.

It was observed that for an error of variance $\Sigma = 1\%$ added to the tissue spectra, the images were similar to the result obtained using the exact spectra (Figure 3.4). In the latter case, in which the same spectra are used to generate the data and reconstruct the image, $\text{Err}_{L^2} = 1.06\%$ (see Table 3.1). For $\Sigma = 3\%$ and $\Sigma = 5\%$ the shape and position of the perturbation were generally reconstructed with sufficient accuracy, but a reduction in contrast was observed in most images. For $\Sigma = 10\%$ the image quality was affected, and in some cases the perturbation could not be identified. The mean relative contrast between the tissues was

$$C^{\%} = \frac{1}{M} \sum_{i=1}^M \frac{(\epsilon_{i2} - \epsilon_{i1})}{\epsilon_{i1}} \approx 34\%, \quad (3.34)$$

therefore it is reasonable to expect that a 10% error added to the spectra would affect the ability of the method to distinguish between the tissues.

3.4.2 Comparison with indirect multifrequency imaging

The results suggest that the proposed fraction reconstruction method is more robust than absolute conductivity imaging and the indirect method. The conductivity images

present an area of high conductivity area around the edge of the tank, which is caused by inaccurate modelling of the boundary geometry, electrode placement, shape and size, and contact impedance. In the fraction images this artefact is reduced because frequency invariant errors are subtracted from the data. The conductivity images obtained in the frequency range 30 – 80 kHz present very low contrast. This is in agreement with the tissue sample conductivity measurements in that the spectra of potato and carrot-saline are very similar in the same frequency range. It is evident by visual comparison that the use of spectral constraints can result in a significant improvement in image quality, when compared to absolute conductivity imaging. If the boundary voltage data is employed directly, then a single optimization problem is solved. To image the fractions indirectly, first an optimization problem is solved for each frequency to reconstruct the conductivity images, then the fitting parameters are computed. The direct reconstruction algorithm uses all multifrequency data to estimate the regularization prior, whereas the indirect method requires that the regularization is first optimized independently for each frequency and then again for computing the fractions.

3.4.3 Comparison with WFD conductivity imaging

Application of the weighted frequency-difference algorithm is limited by the following assumptions (section 2.6.3):

1. $\sigma_0 - \delta_i \sigma_i \approx 0$ on a large background area and on the boundary,
2. $\sigma_0 - \delta_i \sigma_i \neq 0$ on a small anomaly.

Furthermore, use of a linear reconstruction scheme requires the additional assumption that linear changes in conductivity result in linear changes in boundary voltages. In the case of the phantom experiment these assumptions are reasonable because the object consists in a small, low-contrast perturbation immersed in a large homogeneous background. The image quantification results (figures 3.13a and 3.13b) are comparable to fraction imaging in this case. However, the results obtained for the nonlinear case (figures 3.15, 3.16a and 3.16b) show that the fraction method can produce significantly better images than WFD in the case that the assumptions of WFD are violated.

3.4.4 Multiple tissue case

The algorithm was successful in distinguishing between multiple tissues, and returning high contrast. The L^2 -norm error of the solution, defined by equation (3.29), was $\text{Err}_{L^2} = 2.16\%$, which was approximately double the error found in the 2 tissue case (figure 3.4).

3.4.5 Approximation error evaluation

In the example considered, the approximation error given by the fraction model was significantly smaller than the error introduced by the coarsening of the mesh. Furthermore, the error is present only in the representation of mixed elements and thus depends on the proportion of mixed-to-homogeneous elements. If tissues occupy distinct areas of the image and mixed elements are limited to those lying across the boundaries, the approximation error is small. If a large area is occupied by a mixture of tissues, the approximation error could be reduced by modelling the mixture rather than the individual tissues.

3.5 Conclusion

A nonlinear fraction reconstruction method for performing multifrequency EIT using spectral constraints has been formalized, validated and applied. The robustness of the method to errors in the assumed spectra has been investigated and, in the case examined, the method is resistant to a small amount of uncertainty. It has been shown using experimental phantom data that the proposed method can result in improved image quality when compared to absolute and weighted frequency-difference conductivity imaging. The direct use of multifrequency data has proved more robust than fitting multifrequency conductivity images. The proposed method is demonstrably superior to weighted frequency-difference imaging when the assumptions of the latter are violated. The method was applied to a numerical phantom with 4 tissues. It was possible to distinguish between multiple tissues and accurately reconstruct the fraction image of each one. These results suggest that fraction imaging may be suitable for producing one-off clinical diagnostic images using EIT.

The advantages of using spectral constraints in multifrequency EIT are twofold. First, the choice to reconstruct the fraction values, which are frequency independent, allows for the direct and simultaneous use of all multifrequency data. The dimensionality of the problem depends on the number of elements and tissues, and not on the number of frequencies. Therefore it is preferable to use data acquired at all measurement frequencies. As long as the number of frequencies is larger than the number of tissues, implementation of the fraction method increases the number of constraints to the reconstruction and results in a reduction in the degrees of freedom of the problem. Secondly, knowledge of the tissue spectra allows for the use of difference data in the objective function, thus resulting in the subtraction of modelling and frequency independent instrumentation errors in a

nonlinear reconstruction scheme. In conductivity imaging this would require simultaneous estimation of the measurement and reference conductivities, thus increasing the degrees of freedom of the problem. The fraction images could be improved by modelling the change in contact impedance over frequencies. This would result in a further reduction of the edge artefact.

The fraction reconstruction method requires prior knowledge of the impedance spectra of tissues. These can be obtained from the literature, or estimated empirically. Accurate modelling of biological tissues is crucial for clinical applications. The number J of tissue types could be inferred by iteratively applying the algorithm with increasing values of J until a certain criterion is met (e.g., no sharp increase in model likelihood). Alternatively, all possible or expected distinct tissues could be modelled, so that if t is the actual number of tissues, $J \geq t$. The reconstructed fraction values of the tissues that are not present would then be zero. However, a reduction in image quality is to be expected if $J \gg t$. Further studies are necessary to determine how image quality varies with the number of tissues and frequencies.

Chapter 4

Stroke type differentiation using spectrally constrained MFEIT

4.1 Introduction

4.1.1 Overview

The advances in the imaging methodology presented in the previous chapter suggest that the use of spectral constraints could allow for the reconstruction of one-shot images. In particular, MFEIT could enable early diagnosis and thrombolysis of ischaemic stroke, and therefore improve the outcome of treatment. In this chapter, MFEIT using spectral constraints is investigated as a method for imaging the brain in stroke patients. The first application of the fraction reconstruction algorithm to an anatomically realistic three-dimensional model of the human head with skull and scalp is demonstrated. The influence of imprecise modelling is evaluated in three cases: uncertain electrode positions, electrode contact impedance and tissue conductivity spectra. The aim of this study is to demonstrate that the new imaging method might be used to differentiate between stroke types in clinical experiments.

4.1.2 Related work

The application of MFEIT to stroke type differentiation has been investigated at UCL for a number of years [52, 92]. The most recent published study was performed by Packham *et. al* in 2012 [83]. Packham compared the application of linear frequency-difference reconstruction techniques to experimental data obtained from a homogeneous head-shaped tank. In this case, the assumptions of the WFD algorithm are valid, and imaging with WFD was successful. However, if a skull is included in the experimental model, then the assumptions of WFD are violated and, as shown in section 3.3.7, linear imaging fails. The nonlinear fraction reconstruction method is designed to overcome

these limitations, and allow, for the first time, for the imaging of a head model which includes the skull.

The effect of modelling errors has recently been investigated in the case of 2D time-difference EIT imaging [13]. The results indicate that errors in the shape of the electrodes and boundary and in the contact impedance can produce artefacts in the reconstructed images. These effects are likely to be more severe in 3D multifrequency imaging.

4.1.3 Purpose

The purpose of this study is to evaluate the robustness of the fraction imaging method to various sources of error. In order to assess if the method is suitable for application to human subjects, the conditions of a real experiment are reproduced. Specifically, the following questions are addressed:

- What is the effect of the discretization error?
- What is the effect of adding errors to the position of the electrodes (thereby also changing the area and shape)?
- What is the effect of adding errors to the assumed spectral information?
- What is the effect of adding errors to the contact impedance of the electrodes?

4.1.4 Experimental design

A numerical head phantom with homogeneous layers for the brain, skull and scalp was constructed. The meshes and surfaces were obtained from a CT scan of a human head. The CT image was obtained from a patient undergoing treatment for epilepsy at Queen Square Hospital in London. The size of the scan was $512 \times 512 \times 196$, and the resolution was approximately 1 mm in the z direction (bottom-top of the head) and 0.4 mm in the xy plane. The skull and head surface were segmented and post-processed with Seg3D and meshed with the CGAL [24, 118]. The model did not include the cerebro-spinal fluid, a common simplification in head EIT research. The electrodes were placed in the same configuration used to acquire EEG measurements on the scalp. The advantage of this setup is that electrode caps and other equipment intended for EEG applications can be used in experiments. Realistic conductivities for all tissues were taken from the literature for a range of frequencies [92, 52]. In order to avoid the inverse crime [66], two tetrahedral finite element meshes with different resolution were generated, one coarse and one very fine. The fine mesh was used to simulate the boundary voltage data, and the coarse mesh to reconstruct the images (including solution of the forward

problem). The current pattern was chosen to maximize the distance between injecting pairs of electrodes: this was achieved by finding the maximum spanning tree of the electrodes, weighted by the distance between the electrodes. The measurement pattern was optimized to acquire the maximum number of independent measurements. Errors that simulate the most common sources of artefact in an experimental setup were added to the model [71]. For each case, an EIT image was reconstructed using the fraction reconstruction method. The images were evaluated and compared using an objective image quality quantification method.

- The instrumentation noise level was chosen to match that of measurements acquired using the KHU Mark 2.5 EIT system [82] in a saline filled tank, averaged over 64 frames. This noise level is achievable with most EIT measurement systems and can be reduced by use of better instrumentation. The standard deviation of the proportional noise was $\varsigma_p = 0.02\%$ and the standard deviation of the additive noise was $\varsigma_a = 5 \mu\text{V}$ (the additive noise is dominant).
- Electrode positions can be measured to around 1 mm precision using photogrammetry [89]. Other technologies, such as the commercial MicroScribe, laser 3D scanners, or electrode helmets, can achieve an even higher precision in electrode localisation. To demonstrate the importance of using accurate localisation technologies, electrode position errors of around 1 mm and 2 mm were simulated. These relatively small errors resulted in a remarkable degree of image degradation. Given that the electrodes were represented on a discrete mesh, the shape and size of the electrodes changed when an error was added to the position of the centre. This could have been accounted for by refining the mesh, however a coarse representation of the electrodes constituted an unpredictable source of errors, and thus provided a greater similarity between simulation and experiment [62, 13]. Errors were added to the (x, y, z) positions of all electrodes before simulating the data. Deviations of up to 3 times the standard deviation ς of the error are expected in the majority of cases. Therefore the overall shift of the centre of each electrode will normally be less than or equal to

$$\|(\tilde{x}, \tilde{y}, \tilde{z}) - (x, y, z)\| = \sqrt{(3\varsigma)^2 + (3\varsigma)^2 + (3\varsigma)^2} = 3\sqrt{3}\varsigma, \quad (4.1)$$

where $(\tilde{x}, \tilde{y}, \tilde{z})$ is the position of the shifted electrode. For the errors chosen, the corresponding shift is

- $\sqrt{3}(3 \cdot 0.25) \approx 1.3$ mm for a standard deviation of 0.25 mm;
 - $\sqrt{3}(3 \cdot 0.5) \approx 2.6$ mm for a standard deviation of 0.5 mm.
- Knowledge of prior spectral information is affected by tissue anisotropy, inhomogeneity and temperature. Because the combined effect of these factors is difficult to predict, errors based on the literature were simulated that roughly represented frequency-dependent contribution of the errors [33, 50]. To test the limitations of the reconstruction method, a reasonable and a worst-case level of error were considered: respectively 1% and 5%. The errors were added independently to each frequency and each tissue type. It is important to note that the multifrequency reconstruction algorithm used in this study is insensitive to conductivity changes with a flat frequency-spectrum. Therefore only frequency-dependent errors, which constitute a small fraction of the above mentioned error sources, must be considered.
 - The contact impedance errors were chosen on the basis of typical experimental levels. It was assumed that all electrodes had sufficiently low contact impedance. In an experimental setup, this is equivalent to discarding any electrodes with near-infinite impedance that may have detached from the head, or any broken measurement channels. Typically, if the variance of the contact impedance across electrodes is approximately 20%, the setup is considered suboptimal. If the variance of the contact impedance is larger than 50%, then the electrodes have to be re-applied. Therefore these two levels of error were chosen.

4.2 Methods

4.2.1 Model and tissue impedance spectra

A three-dimensional model of a human head was used to simulate the EIT data. The model comprised of three layers, corresponding to the scalp, skull, and brain. A fine mesh with ~ 5 million elements was used to simulate the boundary voltages, and a coarse mesh with ~ 180 thousand elements was used to reconstruct the images. A spherical perturbation of diameter 3 cm was placed in two different positions inside the brain: lateral and posterior (figure 4.2a and 4.2b). In order to simulate an ischaemic stroke, the conductivity of the perturbation was set to the conductivity of ischaemic brain approximately one hour after onset. In order to simulate a haemorrhagic stroke, the conductivity of the perturbation was set to the conductivity of blood. The conductivity

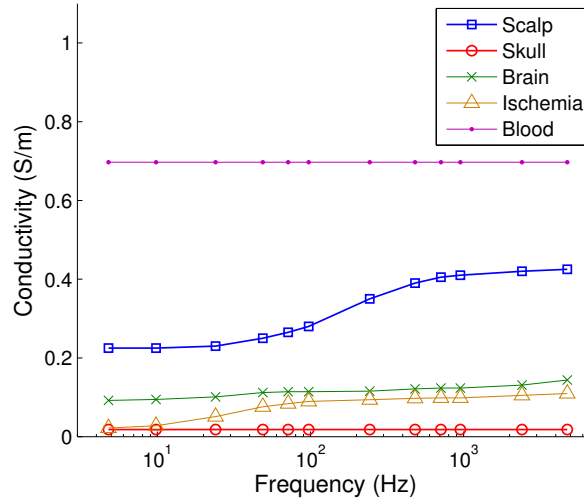


Figure 4.1: Model: conductivity spectra of tissues in the head for the measurement frequencies.

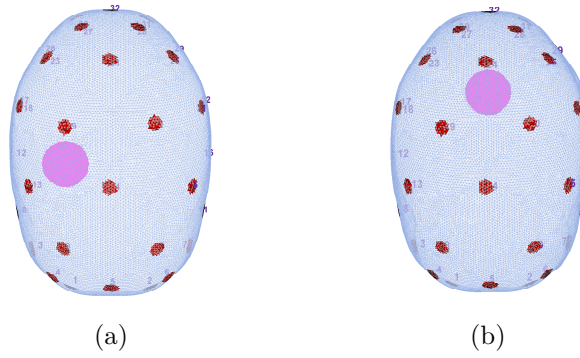


Figure 4.2: Model: top view of the 3D head model, (a) lateral stroke position and (b) posterior stroke position (back of the head is up).

spectra of the tissues (scalp, skull, brain, ischaemic brain, blood) were obtained from the literature [92, 52] (figure 4.1). Twelve frequencies were chosen in the range 5Hz—5kHz because the slopes of the tissue spectra are most different in this region (figure 4.1). Boundary voltages were simulated for each frequency.

4.2.2 Data simulation

32 electrodes of diameter 10 mm were placed on the surface of the model. The electrodes were modelled using the CEM, and the contact impedance was set to $1\text{ k}\Omega$ for all electrodes. The peak-to-peak amplitude of the current was set to $140\text{ }\mu\text{A}$. Voltage measurements were made on all adjacent pairs not involved in delivering the current. The total number of measurements acquired for each frequency was 869.

The boundary voltages were computed using a parallel EIT solver recently developed

at UCL. The PEITS solver [57] is written in C++ and uses the DUNE-FEM package [32]. PEITS is a finite element solver specifically written for EIT using the CEM. It was designed to perform well on multi-core machines and clusters using MPI, and thus reduce the computation time for solving the forward problem. Using PEITS, the mesh was partitioned into largely independent parts on which the weak formulation of the CEM was assembled. The system was then solved iteratively using a conjugate gradient solver, preconditioned by the algebraic multigrid implementation ML [39]. Using PEITS on all 16 cores of a workstation with two 2.4GHz Intel Xeon CPUs with eight cores and 20MB cache each, returned a computation time of less than 2 minutes for 31 forward solutions on the fine (5 million element) mesh.

4.2.3 Image reconstruction

The fractions were recovered simultaneously for all tissues and elements by minimizing the objective function

$$\Phi(\mathbf{F}) = \frac{1}{2} \left[\sum_{i=1}^M \left\| A(\sum_j \mathbf{f}_j \epsilon_{ij}) - A(\sum_j \mathbf{f}_j \epsilon_{0j}) - (\mathbf{v}(\omega_i) - \mathbf{v}(\omega_0)) \right\|^2 + \tau \Psi(\mathbf{F}) \right]. \quad (4.2)$$

A Markov random field (MRF) regularization term of the form

$$\Psi(\mathbf{F}) = \frac{1}{2} \sum_{j=1}^T \sum_{n=1}^N \sum_{l(n)} |f_{nj} - f_{l(n)j}|^2 \quad (4.3)$$

was chosen, where $l(n)$ runs over all neighbours of the n th voxel. Details of the implementation are included in section 3.2.2.

4.2.4 Numerical validation

In order to validate the method, images were reconstructed from simulated data without the addition of modelling errors (except those due to mesh discretisation and measurement noise). The data were simulated using the fine mesh and the images were reconstructed using the coarse mesh. In order to simulate instrumentation error, both proportional and additive noise were added to the data:

$$\text{proportional noise} \quad \mathbf{v}^{\text{with noise}} = \mathbf{v}^{\text{no noise}} (1 + \mathbf{h}_p) \quad (4.4)$$

$$\text{additive noise} \quad \mathbf{v}^{\text{with noise}} = \mathbf{v}^{\text{no noise}} + \mathbf{h}_a, \quad (4.5)$$

where $h \sim \mathcal{N}(0, \varsigma)$ indicates a random number drawn from a Gaussian distribution with zero mean and standard deviation ς . The standard deviation of the proportional noise was $\varsigma_p = 0.02\%$ and the standard deviation of the additive noise was $\varsigma_a = 5 \mu\text{V}$. The skull and scalp were known and fixed in place in the reconstruction, and it was assumed that the area inside the skull was occupied by either the brain, or the stroke. The initial guess was the healthy brain.

The optimal regularization parameter was approximated by computing the L-curve for one step of Gauss-Newton descent. The corner of the L-curve was selected for the first step of the reconstruction, and the value was divided at each step by a factor of 2 for the ischaemic stroke and, given that the contrast was lower, of 3 for the haemorrhagic stroke [115]. The automatic selection of the regularization parameter was repeated in all the following cases, and the maximum number of steps was fixed to ten.

4.2.5 Error simulation

Modelling errors were simulated by altering the model used to simulate the voltages. The position errors were added to the (x, y, z) coordinates of the electrodes separately. The conductivity errors were added to each tissue at frequency individually. The contact impedance errors were added to each electrode separately.

The study was repeated for normally distributed errors with two different levels of variance. The following cases were considered,

- electrode positions: standard deviation 0.25 mm and 0.5 mm, mean the original (x, y, z) positions;
- tissue conductivities: standard deviation 1% and 5%, mean ϵ_{ij} (literature values);
- contact impedance: standard deviation 20% and 50%, mean 1 k Ω .

In addition, proportional and additive noise was added to each data set.

4.2.6 Image quantification

The image quantification method presented in section 3.2.4 was adapted to a head shaped mesh. Three measures of quality were considered: image noise, localization error, and shape error. In order to quantify the ability of the method to distinguish an anomaly (the stroke) from a background (the brain), the fraction \mathbf{f}_s corresponding to the tissue making up the anomaly was assessed.

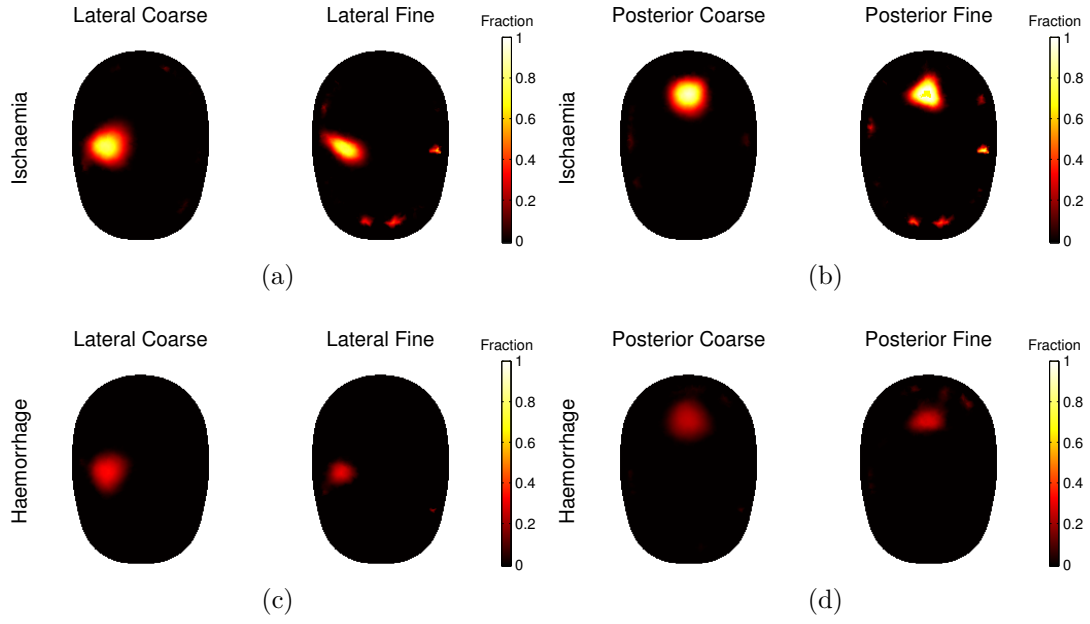


Figure 4.3: Numerical validation images reconstructed from data simulated on the coarse and fine meshes: (a) lateral ischaemic stroke, (b) posterior ischaemic stroke, (c) lateral haemorrhagic stroke, (d) posterior haemorrhagic stroke. Slice through the centre of the head. The scale is the volume fraction value (between 0 and 1).

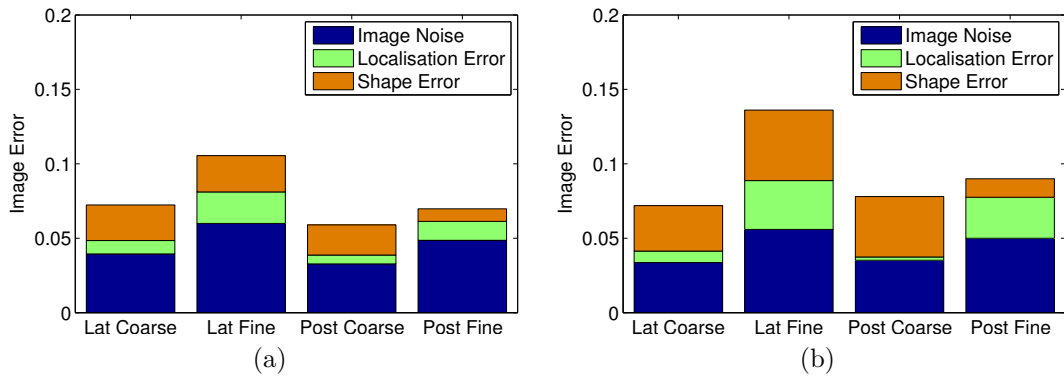


Figure 4.4: Numerical validation results image quality quantification for images reconstructed from data simulated on the coarse and fine meshes: (a) ischaemic stroke, (b) haemorrhagic stroke.

4.3 Results

4.3.1 Numerical validation

The data were simulated on the fine mesh, noise was added to the data, and the images were reconstructed on the coarse mesh. For comparison, the process was repeated using data simulated on the coarse mesh (figure 4.3). The discretization errors introduced differences in the area of each electrode between the fine (5 million elements) and coarse (180 thousand elements) meshes. The average difference in the area of the electrodes

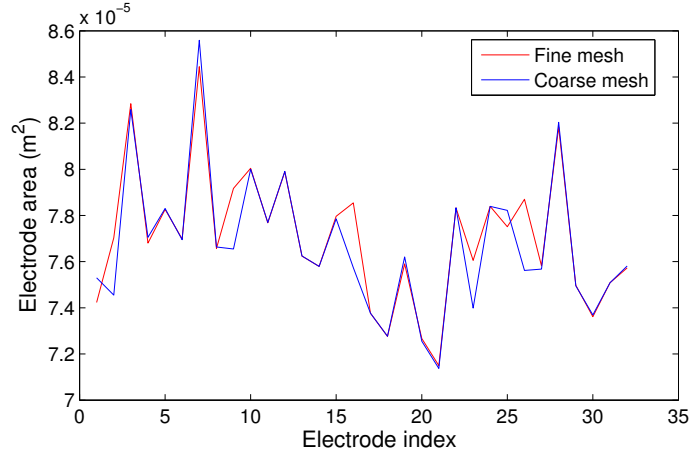


Figure 4.5: Electrode area for the fine (5 million elements) and coarse (180 thousand elements) meshes. The data were simulated on the fine mesh, and the images were reconstructed on the coarse mesh.

between the fine and coarse mesh was $5.6 \cdot 10^{-7} \text{ m}^2$ over an average electrode area of $7.7 \cdot 10^{-5} \text{ m}^2$, i.e. about 1.4% (figure 4.5). Image quantification measures were computed for each of the reconstructed images (figure 4.4). The images obtained from data simulated and reconstructed on the same mesh were superior in terms of the previously defined measure of image quality (section 4.2.6) to those obtained from data simulated on the fine mesh. The contrast recovered in the images of ischaemic strokes was greater than in the images of haemorrhagic strokes. The image quality obtained for the posterior position was in most cases superior than for the lateral position.

4.3.2 Erroneous electrode positions

Images were reconstructed assuming that the electrodes were fixed in the original position (figure 4.6), and image quality measures were computed for each image (figure 4.7). The perturbation was recovered only in the case of 0.25 mm standard deviation error added to ischaemic stroke data. In all other cases the images quality is deteriorated to the point that the imaging must be considered unsuccessful.

4.3.3 Erroneous tissue spectra

Images were reconstructed using the original values for the conductivities of the brain and stroke (figure 4.8), and image quality measures were computed for each image (figure 4.9). The perturbation was recovered successfully in all cases for 1% error, but in the case of 5% error only the lateral ischaemic stroke was identified correctly. Figures 4.10a and 4.10b display the frequency-difference spectra for brain, ischaemic brain and blood, with the associated error bars. The variance of the error on the relative spectra is given by the sum of the variance of the errors added to the absolute values, and the error bars

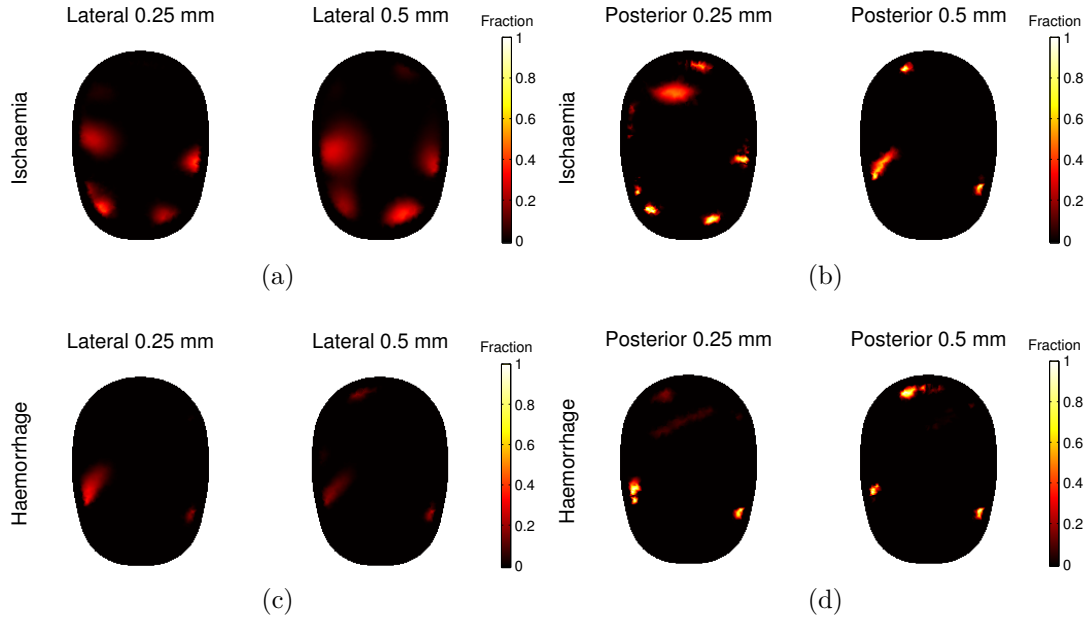


Figure 4.6: Erroneous electrode positions results images reconstructed with errors of 0.25 mm and 0.5mm standard deviation added to the electrode position: (a) lateral ischaemic stroke, (b) posterior ischaemic stroke, (c) lateral haemorrhagic stroke, (d) posterior haemorrhagic stroke. The scale is the volume fraction value (between 0 and 1).

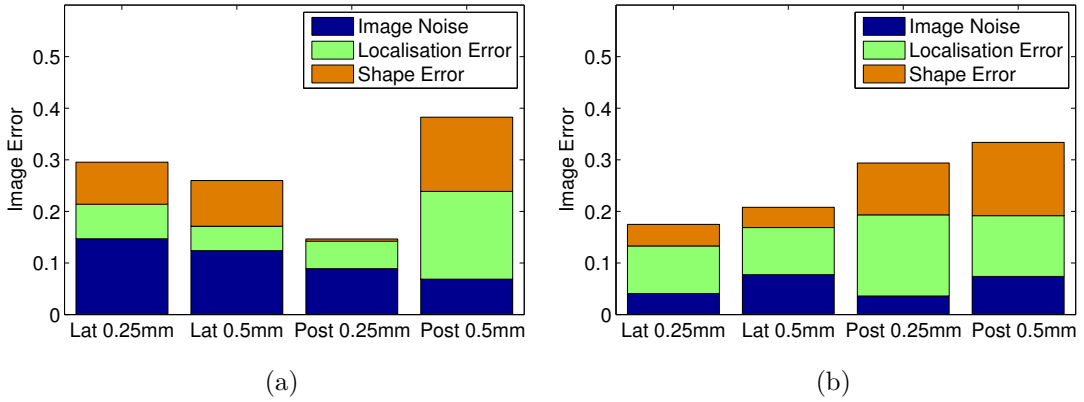


Figure 4.7: Image quantification results for images reconstructed with errors of 0.25 mm and 0.5mm standard deviation added to the electrode position: (a) ischaemic stroke, (b) haemorrhagic stroke.

indicate the minimum and maximum limit within the majority of the errors are drawn, given by ± 3 times the standard deviation.

4.3.4 Erroneous electrode impedances

Images were reconstructed assuming a value of $1\text{ k}\Omega$ for the contact impedance of all electrodes (figure 4.11), and image quality measures were computed for each image (figure 4.12). The images are nearly unchanged by the introduction of 20% errors on the

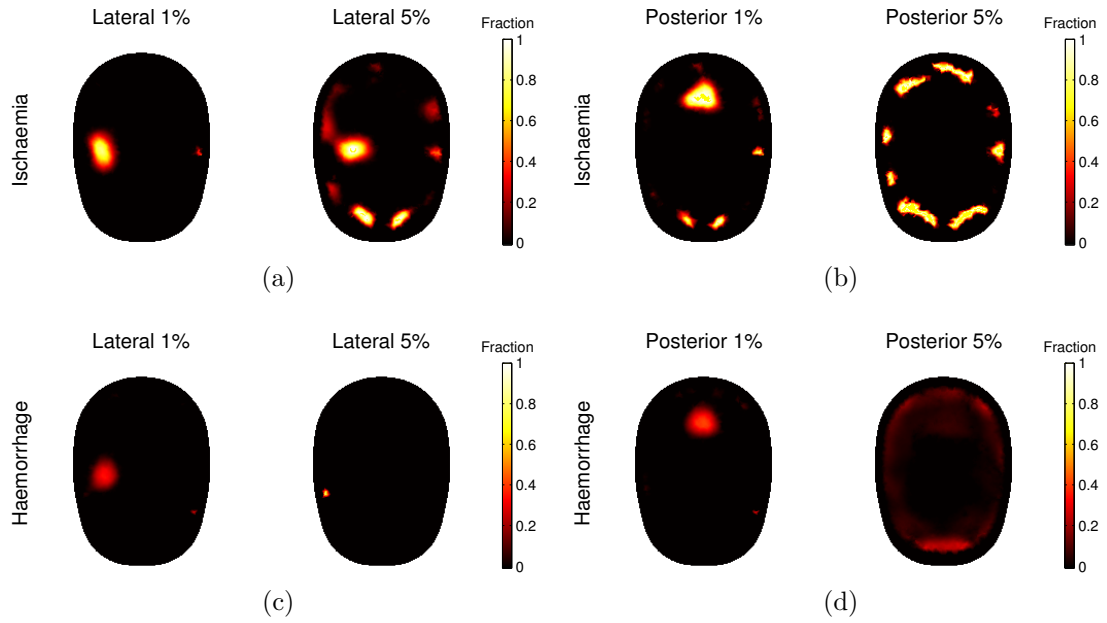


Figure 4.8: Erroneous tissue spectra results, images reconstructed with errors of 1% mm and 5% standard deviation added to the tissue conductivities: (a) lateral ischaemic stroke, (b) posterior ischaemic stroke, (c) lateral haemorrhagic stroke, (d) posterior haemorrhagic stroke. The scale is the volume fraction value (between 0 and 1).

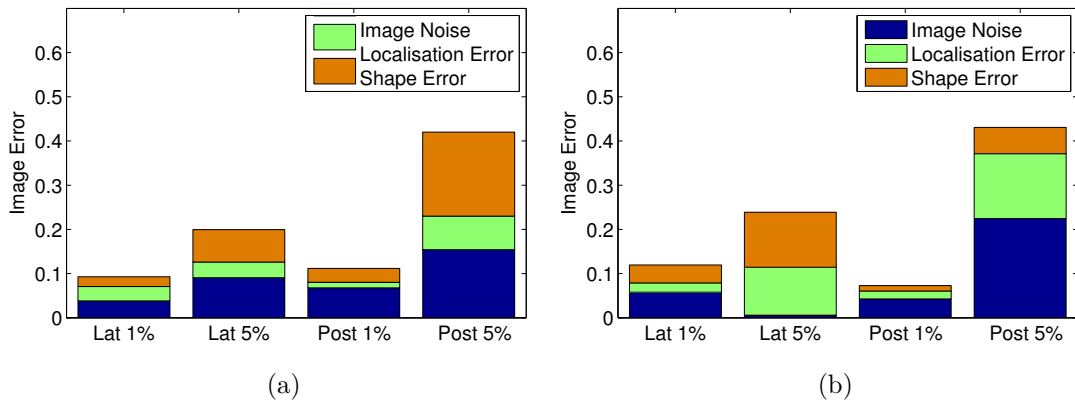


Figure 4.9: Image quantification results for images reconstructed with errors of 1% mm and 5% standard deviation added to the tissue conductivities: (a) ischaemic stroke, (b) haemorrhagic stroke.

contact impedance, and image quality is slightly diminished for 50% errors.

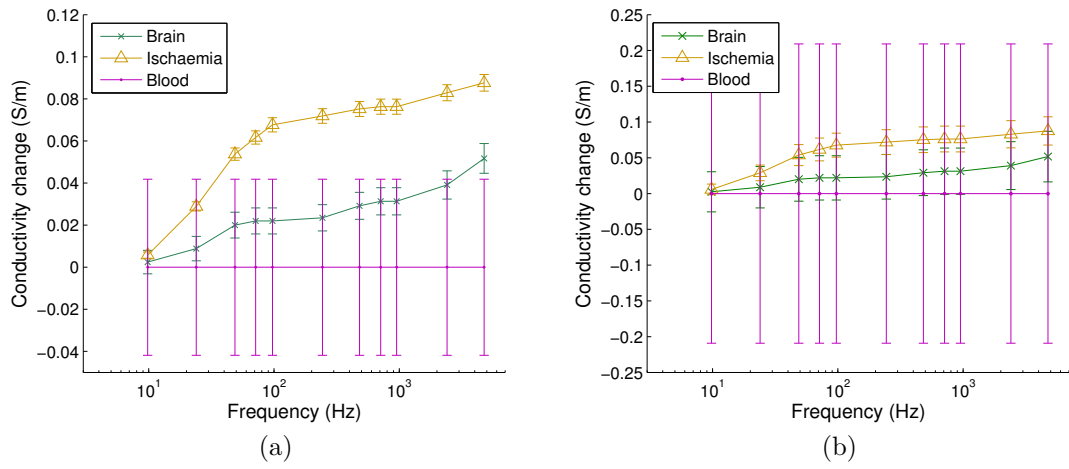


Figure 4.10: Conductivity difference with respect to the lowest frequency for each tissue and associated error bars for (a) 1% and (b) 5% errors added to the absolute spectra. The error bars represent the minimum and maximum limits within which the errors on the relative spectra are drawn. The errors were added to the absolute values of the conductivity, therefore the tissues with highest absolute conductivity have higher variance.

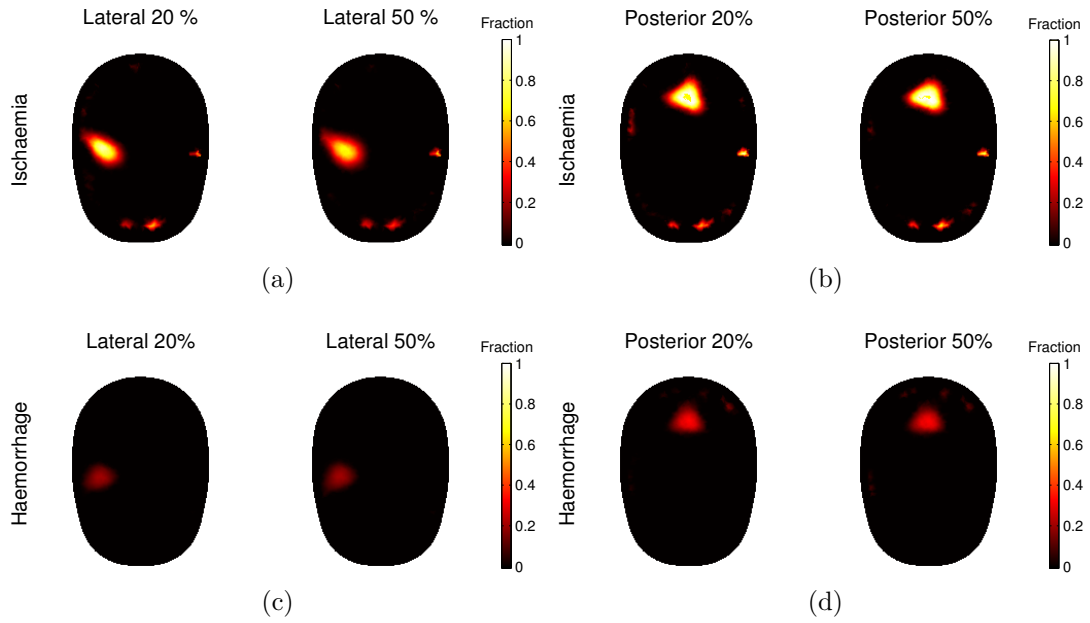


Figure 4.11: Erroneous contact impedance results, images reconstructed with errors of 20% and 50% standard deviation added to the electrode contact impedances: (a) lateral ischaemic stroke, (b) posterior ischaemic stroke, (c) lateral haemorrhagic stroke, (d) posterior haemorrhagic stroke. The scale is the volume fraction value (between 0 and 1).

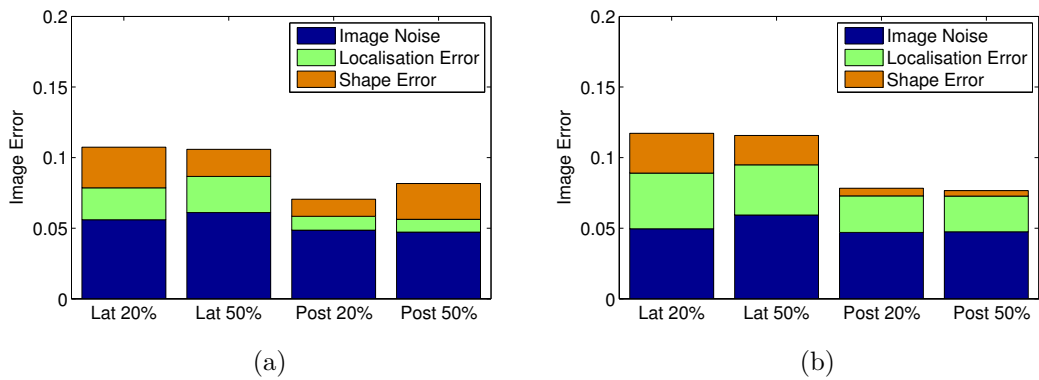


Figure 4.12: Image quantification results for images reconstructed with errors of 20% and 50% standard deviation added to the electrode contact impedances: (a) ischaemic stroke, (b) haemorrhagic stroke.

4.4 Discussion

4.4.1 Numerical validation

The contrast obtained in the images of ischaemic stroke was higher than in the images of haemorrhagic stroke. This can be attributed to variations in the impedance spectra of ischaemic brain and blood. The difference between the slope of the conductivity spectrum of ischaemic brain and healthy brain (figure 4.1) is greater than the difference between blood and healthy brain. Therefore, given that the method uses data referred to the lowest frequency, the signal given by an ischaemic stroke is greater than that of a haemorrhagic stroke of the same size and in the same location.

The reduction in image quality between the case of data simulated on the fine and coarse meshes was primarily caused by the discretization error on the modelling of the electrodes and skull. Given the different resolutions, the shape and size of the electrodes and the skull differ between the two meshes. The purpose of using a fine mesh to simulate the data, and a coarse mesh to reconstruct the image, is to make the simulation study more realistic (figure 4.4). In the case of imaging a real human head, the size and thickness of the skull will not be known exactly. Furthermore, the discrete representation of the electrodes and skull on the mesh will not represent the real position precisely. If the same mesh is used to simulate and reconstruct the data, the problem is over-simplified with respect to the real-case scenario, and conclusions drawn from simulation results may not be applicable in practice (figure 4.3). Therefore it was necessary to consider these discrepancies in order to obtain a realistic simulation.

4.4.2 Erroneous electrode positions

Errors added to the electrode positions severely affected image quality. This highlights the importance of registering the position of the electrodes accurately. These results suggest that the error on the electrode positions must be ≤ 1 mm. Photogrammetry allows for the recovery of electrode positions to a precision of approximately 1 mm [89]. Higher precision could be achieved using the commercial instrument MicroScribe, a laser 3D scanner, or a rigid electrode helmet. Furthermore, in order to preserve the shape and size of the electrodes, the mesh must be sufficiently refined at the boundary (figure 4.5).

4.4.3 Erroneous tissue spectra

The fraction reconstruction method requires knowledge of the conductivity spectra of all tissues, and these are assumed to be fixed and exact. The performance of the algorithm is therefore diminished if the assumed spectral constraints are incorrect (figure

4.9). Furthermore, the confidence with which the reconstruction algorithm distinguishes between different tissues depends on the difference between the conductivity spectra of the tissues. Specifically, given that frequency difference data was used, the tissues were distinguished on the basis of their respective change in conductivity between the lowest and the other frequencies. If a random error is added to the absolute spectrum, then the error on the difference in the spectrum with respect to the lowest frequency is given by the sum of the absolute errors. For 1% error, all the spectra are distinct, but for 5% error, the spectra overlap for some or all frequencies (figures 4.10a and 4.10b). For this reason it was not possible to locate the haemorrhagic stroke in the case of 5% error added to the conductivities (figure 4.8c), and the ischaemic stroke was only identified in the lateral position (figure 4.8a). In the case of haemorrhagic stroke the addition of a proportional 5% error caused a large degree of uncertainty because the absolute value of the conductivity of blood is large. In the case of ischaemic stroke, the uncertainty was caused by the similarity in the spectra of healthy and ischaemic brain.

4.4.4 Erroneous electrode impedances

The effect of the errors added to the contact impedance is very limited. A change in the contact impedance will cause a change in the current distribution around the electrode. However, given that the conductivity of the electrode is very high relative to the conductivity of the object, changes in the electrode impedance have a small effect on the current flow inside the object. For this reason the images obtained after adding errors to the contact impedance are similar to the original images without modelling errors.

4.4.5 Technical remarks

Ideally, several images would have been created for each noise level in order to characterise the effect of modelling errors over a very large number of samples. The computational expense of multiple repetitions was prohibitive, in that reconstruction of a single image took 5-6 hours. The run time could be reduced by parallelizing the solution of the forward problem in the image reconstruction, or applying a memory-efficient (matrix free) inversion scheme. Given that the electrode specific errors (contact impedance and position) were sampled on the 32 electrodes individually, this provides a sufficiently large number of samples to give a reasonable characterization of the influence of the noise. Likewise, in the case of errors added to the tissue spectra, the noise was added independently to each tissue and at each frequency, and this allows us to describe the

effect of the spectral error reasonably well. Thus, the conclusions derived from this relatively small number of images appear to be valid in principle. Examination of more permutations in simulation and tank studies may allow for the identification of quantitative limits to the acceptable variation of each parameter.

4.5 Conclusion

The fraction reconstruction method using spectral constraints was applied to a numerical head phantom with realistic conductivity. The first images of a human head model including a skull have been produced by use of spectral constraints. Noise and modelling errors were added to investigate the robustness of the imaging method. The results demonstrate a varying degree of sensitivity to different sources of error:

- the method is highly sensitive to errors in the position and shape of the electrodes, and these must be modelled with the highest achievable level of accuracy;
- the fraction reconstruction method allows tissues to be distinguished if the respective spectra are sufficiently distinct;
- the method is highly robust to errors in the assumed contact impedance.

Further work is needed to improve image quality in the presence of modelling errors. The artefact caused by errors in the geometric model of the skull in the case that different models are used to simulate and reconstruct the data may be reduced by simultaneously reconstructing the brain and the skull. This may allow to distinguish between the stroke and the skull artefact. Further investigation into the level of accuracy necessary to model the electrodes is required. This would determine an upper limit for the level of precision required in measuring the position of the electrodes, and a lower limit for the resolution of the mesh at the boundary.

This work is part of a wider project on stroke imaging using EIT. This feasibility study is a first step towards demonstrating that the use spectral constraints can provide the first images of ischaemic and haemorrhagic stroke in the human head using MFEIT. The methods developed in this thesis are currently being applied to tank phantom and animal model data. There are plans to proceed to clinical trials in 2015.

Chapter 5

A reconstruction-classification method for MFEIT

5.1 Introduction

5.1.1 Overview

The multifrequency EIT method presented in chapter 3 exploits prior knowledge of the conductive properties of tissues by allowing for the inclusion of explicit spectral constraints in the image reconstruction problem. The disadvantage of the fraction reconstruction method is that exact prior knowledge of the tissue spectra is required. This limits the application of the method to cases in which the conductivity of the tissues involved are known with a high level of accuracy. Approximate values for the tissue spectra can be obtained from the literature or *in vivo* empirical measurements, however these values are subject to variability. For example, unpredictable variations may be caused by changes in temperature, cell count, or flow-rate of bodily fluids. The fraction method treats the conductivity of a tissue at a certain frequency as a point-value, which is assumed to be known exactly and is fixed throughout the reconstruction. In this chapter, a more realistic representation of the prior is obtained by associating a probability distribution to the tissue spectra. Further, a method is developed to use the multifrequency boundary voltage data to inform the spectral model, in addition to reconstructing the conductivity.

5.1.2 Related work

A similar problem in the field of diffuse optical tomography (DOT) was studied by Hiltunen *et al.* [45]. In DOT imaging, two physical quantities are recovered: light absorption and scattering. The authors proposed to exploit the covariance between the absorption and scattering parameters to produce an algorithm which alternated

reconstruction and classification steps. If the result of the reconstruction step is visualized in a 2D scatter plot where the axes are the absorption and the scattering parameters, then the values form a number of clusters that is equal to the number of tissues in the domain. The voxels can therefore be classified by the clustering, and the mean and standard deviation of the tissue properties can be updated on the basis of the image. This idea can not be applied directly to EIT because there is only one reconstructed parameter, the conductivity. However, the covariance between the conductivity recovered at different frequencies can be treated in a similar way to distinguish between the tissues. The voxels can therefore be classified on the basis of the clustering of the spectra in a scatter plot of dimensions the number of frequencies.

5.1.3 Purpose

In this chapter, a method is presented for estimating the real spectra of the tissues in the domain, whilst simultaneously reconstructing an image of conductivity for each frequency. It is assumed that the domain is occupied by a finite number of tissues with distinct spectral properties, and the conductivity spectrum of each tissue is modelled by a Gaussian distribution. The proposed *reconstruction-classification* method is validated on simulated data, and the robustness of the method to errors in the initial guess of the tissue conductivities is tested for increasing levels of variance. Results obtained with and without introducing spatially smoothing regularization are compared. The use of frequency-difference data in the reconstruction-classification method is investigated and the method is validated using simulated data. The images obtained in simulation are evaluated and compared by an objective measure of quality. Finally, the proposed method is applied to experimental phantom data and the use of absolute and frequency-difference data are compared.

5.1.4 Experimental design

5.1.4.1 Reconstruction-classification method

A combined imaging method was devised which attempts to simultaneously solve the problems of reconstructing an image using spectral information and classifying the image per tissue type. The number of tissues, or classes, will be equal to the number of tissues that have distinct spectra, and can therefore be differentiated by MFEIT. The classification problem can be interpreted as a binary labelling problem, where the aim is to assign to each voxel a set of labels that identifies a single tissue. These labels constitute a hidden variable that determines the conductivity. The probability that a

voxel is occupied by a certain tissue is obtained by "fuzzy labelling" the reconstructed conductivity image [88]. The result of the labelling step is used to update the initial guess of the mean and covariance of the spectra at each iteration of the reconstruction algorithm.

Two variants of the reconstruction-classification method were formalized, one using absolute and one using frequency-difference data. These were validated on simulated data.

5.1.4.2 Robustness to spectral errors

The purpose of the classification step is to update the properties of the tissue classes on the basis of information provided by the data. The aim is to account for uncertainty in the initial guess of the mean and variance of the tissue spectra. If, for example, the real tissue conductivities differ from the literature values used in the first reconstruction step, then the classification process will compensate for the mismatch by shifting the mean of the classes. The updated parameters are then used in the successive reconstruction step. In order to test the efficacy of this technique, a simulation study was performed. Errors were added to the initial guess of the tissue spectra, and images were reconstructed using the original values as the initial guess. Multiple repetitions were performed for increasing levels of error.

5.1.4.3 Reconstruction-classification with spatial smoothing

The use of spatial smoothing in addition to the spectral prior in the reconstruction step was investigated. Spatial smoothness information provides an additional mean for improving the ill-posedness of the problem, however blurring across tissue boundaries deteriorates the clustering of the tissue classes. Results obtained using homogeneous MRF regularization were compared to results obtained with no spatial smoothing and with a label-dependent MRF.

5.1.4.4 Comparison with other methods

Images were reconstructed using absolute and a weighted frequency-difference EIT imaging, and compared with results obtained with the reconstruction-classification method.

5.1.4.5 Phantom experiment

A phantom experiment was performed to compare the use of absolute and frequency-difference data in the reconstruction-classification method. The disadvantage of using absolute data is that the algorithm is highly sensitive to modelling errors. This may

affect the performance of the method when applied to experimental data. For this reason, a method which uses data referred to a low frequency, or frequency-difference data, may bring advantages in terms of the reduction of boundary artefacts. On the other hand, the number of data points is decreased from the absolute case, whereas the number of unknowns is unchanged. Furthermore, the reconstruction problem is no longer unique. It is expected, however, that the tissues can still be identified uniquely from the *difference* images, of the conductivity difference with respect to the reference frequency.

5.2 Method

5.2.1 Multinomial model

The Finite Element Model of a conductive object is considered. It is assumed that the object is composed of a finite number of tissues, and that each element of the mesh is assigned to a single tissue. A set of binary variables $\zeta_n = \{\zeta_{n1}, \dots, \zeta_{nj}, \dots, \zeta_{nJ}\}$ is defined for each element, where J is the number of tissues,

$$\zeta_{nj} = \begin{cases} 1 & \text{if the } j\text{th tissue is assigned to the } n\text{th element;} \\ 0 & \text{otherwise;} \end{cases} \quad (5.1)$$

The values

$$\zeta_n = \{\zeta_{n1}, \dots, \zeta_{nj}, \dots, \zeta_{nJ}\}$$

are drawn from a multinomial distribution $p(\zeta_n) \sim \text{Multin}(1, \lambda_j)$, where λ_j is the overall probability that an element is occupied by the tissue t_j . The values of λ_j are drawn from a Dirichlet distribution $\lambda_j \sim \text{Dir}(\alpha_j)$, where α_j is the expected number of elements in the j th class. The probability that the set $\zeta_n = \{\zeta_{n1}, \dots, \zeta_{nj}, \dots, \zeta_{nJ}\}$ is assigned to the n th element, given $\lambda = \{\lambda_j; j = 1, \dots, J\}$, is

$$p(\zeta_n | \lambda) = \prod_j \lambda_j^{\zeta_{nj}}. \quad (5.2)$$

If the tissue t_j is assigned to the n th voxel, then it is assumed that the conductivity of the voxel at all frequencies $\sigma_n = \{\sigma_n(\omega_i); i = 1, \dots, M\}$, where M is the number of

frequencies, is given by a multivariate normal distribution

$$\begin{aligned} p(\boldsymbol{\sigma}_n|\theta_j) &= \frac{1}{\sqrt{(2\pi)^J |\boldsymbol{\Sigma}_j|}} \exp\left(-\frac{1}{2}(\boldsymbol{\sigma}_n - \mathbf{m}_j)^T \boldsymbol{\Sigma}_j^{-1} (\boldsymbol{\sigma}_n - \mathbf{m}_j)\right) \\ &= \mathcal{N}_\sigma(\mathbf{m}_j, \boldsymbol{\Sigma}_j), \end{aligned} \quad (5.3)$$

where $\theta_j = \{(\mathbf{m}_j, \boldsymbol{\Sigma}_j)\}$ specifies the mean $\mathbf{m}_j = \{m_{ij}; i = 1, \dots, M\}$ and covariance matrix $\boldsymbol{\Sigma}_j \in \mathbb{R}^{M \times M}$ of the spectrum of the j th tissue. Therefore, if the indicator variables ζ_{nj} are known, the probability distribution of the conductivities of the n th voxel is

$$p(\boldsymbol{\sigma}_n|\boldsymbol{\zeta}_n, \boldsymbol{\theta}) = \prod_j (p(\boldsymbol{\sigma}_n|\theta_j))^{\zeta_{nj}}. \quad (5.4)$$

The joint probability of recovering $(\boldsymbol{\sigma}_n, \boldsymbol{\zeta}_n)$ is

$$p(\boldsymbol{\sigma}_n, \boldsymbol{\zeta}_n|\boldsymbol{\theta}, \boldsymbol{\lambda}) = p(\boldsymbol{\sigma}_n|\boldsymbol{\zeta}_n, \boldsymbol{\theta})p(\boldsymbol{\zeta}_n|\boldsymbol{\lambda}) = \prod_j [\lambda_j p(\boldsymbol{\sigma}_n|\theta_j)]^{\zeta_{nj}}. \quad (5.5)$$

By marginalizing over all possible values of the indicator variables ζ_{nj} the *mixture of Gaussians* model for the conductivity is obtained

$$p(\boldsymbol{\sigma}_n|\boldsymbol{\theta}, \boldsymbol{\lambda}) = \int_{\boldsymbol{\zeta}_n} p(\boldsymbol{\sigma}_n, \boldsymbol{\zeta}_n|\boldsymbol{\theta}, \boldsymbol{\lambda}) d\boldsymbol{\zeta}_n = \sum_j \lambda_j p(\boldsymbol{\sigma}_n|\theta_j). \quad (5.6)$$

Using a non-informative prior for the means $p(\mathbf{m}_j) \propto 1$, the conjugate prior distribution for the covariances is given by the *normal inverse Wishart distribution*

$$NIW(\nu_j, \boldsymbol{\Gamma}_j) = |\boldsymbol{\Sigma}_j|^{-(\nu+d+1)/2} \exp\left[-\frac{1}{2}\text{Tr}(\boldsymbol{\Gamma}_j \boldsymbol{\Sigma}_j^{-1})\right], \quad (5.7)$$

where d is the dimension of the domain, ν_j indicates the number of degrees of freedom, and $\boldsymbol{\Gamma}_j$ is a scaling matrix. If the prior is non-informative, $\nu_j = 0$ and $\boldsymbol{\Gamma}_j = 0$, so that

$$p(\boldsymbol{\Sigma}_j) = |\boldsymbol{\Sigma}_j|^{-(d+1)/2}, \quad (5.8)$$

which is known as Jeffreys prior [45].

5.2.2 Combined reconstruction-classification outline

A set of boundary voltage measurements $\mathbf{v}_i = \{v_{ki}; k = 1, \dots, K\}$ is acquired at each frequency $\{\omega_i; i = 1, \dots, M\}$. The conductivity distribution can be recovered iteratively by alternating a reconstruction and a classification step

1. Reconstruction:

$$\boldsymbol{\sigma}^{t+1} = \arg \min_{\boldsymbol{\sigma}} \frac{1}{2} \|\mathbf{L}_v(A(\boldsymbol{\sigma}) - \mathbf{v})\|^2 - \frac{1}{2} \log p(\boldsymbol{\sigma}|\boldsymbol{\zeta}^t, \boldsymbol{\theta}^t), \quad (5.9)$$

where $\boldsymbol{\sigma} \in \mathbb{R}^{N \cdot M}$ accounts for N voxels and M frequencies, $\|\cdot\|$ indicates the Frobenious norm, and \mathbf{L}_v is a weighting matrix.

2. Classification:

$$\text{E-step: } \boldsymbol{\zeta}^{t+1} = \arg \max_{\boldsymbol{\zeta}} p(\boldsymbol{\zeta}|\boldsymbol{\sigma}^t, \boldsymbol{\theta}^t, \boldsymbol{\lambda}^t) \quad (5.10)$$

$$\text{M-step: } (\boldsymbol{\theta}^{t+1}, \boldsymbol{\lambda}^{t+1}) = \arg \max_{(\boldsymbol{\theta}, \boldsymbol{\lambda})} p(\boldsymbol{\sigma}^t|\boldsymbol{\theta}, \boldsymbol{\lambda})p(\boldsymbol{\theta}, \boldsymbol{\lambda}). \quad (5.11)$$

5.2.3 Reconstruction

Substituting equation (5.4) into equation (5.9) and assuming that the elements are independent, the objective function becomes

$$\boldsymbol{\sigma} = \arg \min_{\boldsymbol{\sigma}} \frac{1}{2} \|\mathbf{L}_v(A(\boldsymbol{\sigma}) - \mathbf{v})\|^2 - \frac{1}{2} \sum_{n,j} \zeta_{nj} \log p(\boldsymbol{\sigma}_n|\theta_j), \quad (5.12)$$

where

$$\mathbf{v} = \{\mathbf{v}_1; \dots; \mathbf{v}_i; \dots; \mathbf{v}_M\} \in \mathbb{R}^{K \cdot M}$$

$$A(\boldsymbol{\sigma}) = \{A(\boldsymbol{\sigma}_1); \dots; A(\boldsymbol{\sigma}_i); \dots; A(\boldsymbol{\sigma}_M)\} \in \mathbb{R}^{K \cdot M}.$$

The weighting matrix \mathbf{L}_v , of dimensions $\mathbb{R}^{K \cdot M \times K \cdot M}$, holds the values

$$1/(\sqrt{2M} \|A(\boldsymbol{\sigma}_i^0) - \mathbf{v}_i\|)$$

on the diagonal, where $\boldsymbol{\sigma}^0$ is the initial guess for the conductivity, and serves the purpose of equilibrating the contribution of each frequency to the reconstruction. The measurement noise is assumed to be uncorrelated across frequencies, therefore the off-diagonal values are all zero.

The regularization term is found by fixing the value of the indicator parameters $\boldsymbol{\zeta}$ to the *maximum-a-posteriori* estimate recovered by the previous classification step

$$\text{MAP}(\boldsymbol{\zeta}) = \arg \max_{\boldsymbol{\zeta}} p(\boldsymbol{\zeta}|\boldsymbol{\sigma}^{t-1}, \boldsymbol{\theta}^{t-1}, \boldsymbol{\lambda}^{t-1}). \quad (5.13)$$

The result of the MAP estimate is a binary image with only 0 or 1 values, where for each voxel the label corresponding to the tissue that has highest probability of occupying the voxel is set to one, and all other labels are set to 0. The expected spectrum of the n th element becomes

$$\bar{\sigma}_n = \sum_j \zeta_{nj} \cdot m_{ij} \Big|_{\text{MAP}(\zeta)} = m_{ij'} \quad i = 1, \dots, M \quad (5.14)$$

if the j' th tissue has maximum probability of being assigned to the n th element. Therefore (5.4) becomes

$$p(\sigma | \zeta, \theta) = \prod_n \prod_j p(\sigma_n | \theta_j)^{\zeta_{nj}} = \mathcal{N}_\sigma(\bar{\sigma}, \Sigma_{\bar{\sigma}}), \quad (5.15)$$

where $\bar{\sigma} \in \mathbb{R}^{N \cdot M}$ and $\Sigma_{\bar{\sigma}} \in \mathbb{R}^{N \cdot M \times N \cdot M}$ is a sparse matrix of which the n th $M \times M$ block along the diagonal is $\Sigma_{j'}$ if the n th elements belongs to the j' th class.

The conductivity at all frequencies is thus obtained from equation (5.9) by minimizing,

$$\sigma = \arg \min_{\sigma} \frac{1}{2} \|\mathbf{L}_v(A(\sigma) - \mathbf{v})\|^2 + \frac{\tau}{2} \underbrace{\|L_{\bar{\sigma}}(\sigma - \bar{\sigma})\|^2}_{\Psi_{\bar{\sigma}}(\sigma)}, \quad (5.16)$$

where τ is a regularization parameter and $L_{\bar{\sigma}} \in \mathbb{R}^{N \cdot M \times N \cdot M}$ is the Cholesky decomposition of $\Sigma_{\bar{\sigma}}^{-1}$.

Positivity is enforced by introducing an auxiliary variable ρ such that $\rho_{ni} = \log(\sigma_{ni}) \ \forall n, i$. The objective function is expressed in terms of the variable ρ , and the derivatives are computed using the chain rule. At the reconstruction step t , the problem is initialized to the result of the previous classification step $\bar{\sigma}^t$, the corresponding auxiliary variable is computed, and one step of damped Gauss-Newton descent [53] is performed to obtain ρ^{t+1} . Finally, the result of the reconstruction step is

$$\sigma_{ni}^{t+1} = \exp(\rho_{ni}^{t+1}) > 0 \quad \forall n, i.$$

5.2.4 Classification

The classification step computes the expected values for the labels (E-step), and updates the tissue-class spectral parameters (θ, λ) (M-step), given the conductivity image σ^t .

5.2.4.1 E-step

The *responsibility* r_{nj}^t is a measure of the probability that the n th voxel is occupied by the j th tissue

$$\begin{aligned} p(\zeta_{nj} = 1 | \boldsymbol{\sigma}_n, \boldsymbol{\theta}^t, \boldsymbol{\lambda}^t) &= \frac{p(\boldsymbol{\sigma}_n | \zeta_{nj} = 1, \boldsymbol{\theta}^t) p(\zeta_{nj} = 1)}{p(\boldsymbol{\sigma}_n | \boldsymbol{\theta}^t, \boldsymbol{\lambda}^t)} = \\ &= \frac{\lambda_j^t p(\boldsymbol{\sigma}_n^t | \theta_j^t)}{\sum_j \lambda_j^t p(\boldsymbol{\sigma}_n^t | \theta_j^t)} = \\ &= r_{nj}^t \end{aligned} \quad (5.17)$$

The expectation for the indicator values is

$$\begin{aligned} E(\zeta_{nj} | \boldsymbol{\sigma}_n, \boldsymbol{\theta}^t, \boldsymbol{\lambda}^t) &= \int \zeta_{nj} p(\zeta_{nj} | \boldsymbol{\sigma}_n, \boldsymbol{\theta}^t, \boldsymbol{\lambda}^t) d\zeta_{nj} = \\ &= 0 * p(\zeta_{nj} = 0 | \boldsymbol{\sigma}_n, \boldsymbol{\theta}^t, \boldsymbol{\lambda}^t) + 1 * p(\zeta_{nj} = 1 | \boldsymbol{\sigma}_n, \boldsymbol{\theta}^t, \boldsymbol{\lambda}^t) = \\ &= r_{nj}^t \end{aligned} \quad (5.18)$$

Therefore the MAP estimate for the labels, and the solution to equation (5.13), is

$$\zeta_{nj}^{t+1} = \begin{cases} 1 & \text{if } r_{nj}^t \text{ is maximum } \forall j, \\ 0 & \text{otherwise.} \end{cases} \quad (5.19)$$

5.2.4.2 M-step

The parameters $(\boldsymbol{\theta}, \boldsymbol{\lambda})$ are chosen in order to maximize the log posterior (5.11)

$$(\boldsymbol{\theta}^{t+1}, \boldsymbol{\lambda}^{t+1}) = \arg \max_{(\boldsymbol{\theta}, \boldsymbol{\lambda})} \log p(\boldsymbol{\sigma}^t | \boldsymbol{\theta}, \boldsymbol{\lambda}) + \log p(\boldsymbol{\theta}, \boldsymbol{\lambda}) \quad (5.20)$$

Averaging over all possible values of $\boldsymbol{\zeta}$ gives

$$\log p(\boldsymbol{\sigma}^t | \boldsymbol{\theta}, \boldsymbol{\lambda}) + \log p(\boldsymbol{\theta}, \boldsymbol{\lambda}) = \int_{\boldsymbol{\zeta}} \log p(\boldsymbol{\sigma}^t, \boldsymbol{\zeta} | \boldsymbol{\theta}, \boldsymbol{\lambda}) d\boldsymbol{\zeta} + \log p(\boldsymbol{\theta}, \boldsymbol{\lambda}) \quad (5.21)$$

Using *Jensen's inequality* [88] and ignoring terms which do not depend on $(\boldsymbol{\theta}, \boldsymbol{\lambda})$, a lower bound for the log-prior is obtained

$$\begin{aligned}\mathcal{B}(\boldsymbol{\theta}, \boldsymbol{\lambda}) &= \sum_n \sum_j r_{nj}^t \log(\lambda_j p(\boldsymbol{\sigma}_n | \theta_j)) + \log p(\boldsymbol{\lambda}) + \log p(\boldsymbol{\theta}) = \\ &= \sum_n \sum_j r_{nj}^t \left[\log(\lambda_j) - \log(|\boldsymbol{\Sigma}_j|) - \frac{1}{2}(\boldsymbol{\sigma}_n - \mathbf{m}_j)' \boldsymbol{\Sigma}_j^{-1} (\boldsymbol{\sigma}_n - \mathbf{m}_j) \right] \\ &\quad + \sum_j \left[(\alpha_j - 1) \log(\lambda_j) - \frac{\nu_j + d + 1}{2} \log |\boldsymbol{\Sigma}_j| \right]\end{aligned}\quad (5.22)$$

Maximizing $\mathcal{B}(\boldsymbol{\theta}, \boldsymbol{\lambda})$ for $\sum_j \lambda_j = 1$ and using the mode of the Dirichlet distribution for λ_j , returns the update rules for the parameters,

$$\lambda_j^{t+1} = \frac{\sum_n r_{nj}^t + (\alpha_j - 1)}{N + \sum_j \alpha_j - J} \quad (5.23)$$

In the case of a non-informative priors $\alpha_j = 1$ and $p(\mathbf{m}_j) \propto 1$

$$\lambda_j^{t+1} = \frac{\sum_n r_{nj}^t}{N}, \quad (5.24)$$

$$\mathbf{m}_j^{t+1} = \frac{\sum_n r_{nj}^t \boldsymbol{\sigma}_n}{\sum_n r_{nj}^t}, \quad (5.25)$$

$$\boldsymbol{\Sigma}_j^{t+1} = \frac{\sum_n r_{nj}^t (\boldsymbol{\sigma}_n - \mathbf{m}_j)(\boldsymbol{\sigma}_n - \mathbf{m}_j)^T + \boldsymbol{\Gamma}_j}{\sum_n r_{nj}^t + \nu_j + d + 1}. \quad (5.26)$$

5.2.5 Frequency-difference reconstruction-classification outline

The class parameters $\theta_j^{\text{fd}} = \{(\mathbf{m}_j^{\text{fd}}, \boldsymbol{\Sigma}_j^{\text{fd}})\}$ specify the mean and covariance matrix of the *relative* spectrum of the j th tissue:

$$\mathbf{m}_j^{\text{fd}} \equiv \{m_{2j} - m_{1j}; \dots, m_{ij} - m_{1j}; \dots, m_{Mj} - m_{1j}\} \quad \forall j,$$

where the lowest frequency ω_1 is chosen as reference.

The conductivity distribution is recovered by performing a reconstruction step using frequency-difference data, calculating the frequency-difference conductivity images, and following with a classification step

1. Frequency-difference reconstruction:

$$\boldsymbol{\sigma}^{t+1} = \arg \min_{\boldsymbol{\sigma}} \frac{1}{2} \left\| \mathbf{L}_v^{\text{fd}} (A^{\text{fd}}(\boldsymbol{\sigma}) - \mathbf{v}^{\text{fd}}) \right\|^2 - \frac{1}{2} \log p(\boldsymbol{\sigma}^{\text{fd}} | \boldsymbol{\zeta}^t, \boldsymbol{\theta}^{\text{fd}, t}), \quad (5.27)$$

where \mathbf{v}^{fd} is the set of frequency-difference data. The frequency-difference conductivity images are given by:

$$\boldsymbol{\sigma}^{\text{fd}} = \{\boldsymbol{\sigma}_i - \boldsymbol{\sigma}_1 \mid \forall i = 2, \dots, M\} \quad (5.28)$$

2. Frequency-difference classification:

$$\text{E-step: } \zeta^{t+1} = \arg \max_{\zeta} p(\zeta | \boldsymbol{\sigma}^{\text{fd},t}, \boldsymbol{\theta}^{\text{fd},t}, \boldsymbol{\lambda}^t) \quad (5.29)$$

$$\text{M-step: } (\boldsymbol{\theta}^{\text{fd},t+1}, \boldsymbol{\lambda}^{t+1}) = \arg \max_{(\boldsymbol{\theta}^{\text{fd}}, \boldsymbol{\lambda})} p(\boldsymbol{\sigma}^{\text{fd},t} | \boldsymbol{\theta}^{\text{fd}}, \boldsymbol{\lambda}) p(\boldsymbol{\theta}^{\text{fd}}, \boldsymbol{\lambda}). \quad (5.30)$$

5.2.6 Frequency-difference reconstruction

The reconstruction problem is modified from the absolute case to use data referred to a baseline frequency. If data is normalized by the reference the norm of the residual error becomes

$$\sum_{i=2}^M \frac{1}{2} \left\| \mathbf{L}_v^i \left(\frac{A(\boldsymbol{\sigma}_i) - A(\boldsymbol{\sigma}_1)}{A(\boldsymbol{\sigma}_1)} - \frac{\mathbf{v}_i - \mathbf{v}_1}{\mathbf{v}_1} \right) \right\|^2 = \frac{1}{2} \left\| \mathbf{L}_v^{\text{fd}} (A^{\text{fd}}(\boldsymbol{\sigma}) - \mathbf{v}^{\text{fd}}) \right\|^2, \quad (5.31)$$

where \mathbf{L}_v^{fd} hold the values

$$\mathbf{L}_v^i = 1 / \left(\sqrt{2(M-1)} \left\| \frac{A(\boldsymbol{\sigma}_i^0) - A(\boldsymbol{\sigma}_1^0)}{A(\boldsymbol{\sigma}_1^0)} - \frac{\mathbf{v}_i - \mathbf{v}_1}{\mathbf{v}_1} \right\| \right) \quad \forall i = 2, \dots, M$$

on the diagonal,

$$\mathbf{v}^{\text{fd}} = \left\{ \frac{\mathbf{v}_2 - \mathbf{v}_1}{\mathbf{v}_1}; \dots, \frac{\mathbf{v}_i - \mathbf{v}_1}{\mathbf{v}_1}; \dots, \frac{\mathbf{v}_M - \mathbf{v}_1}{\mathbf{v}_1} \right\} \in \mathbb{R}^{K \cdot (M-1)},$$

and

$$A^{\text{fd}}(\boldsymbol{\sigma}) = \left\{ \frac{A(\boldsymbol{\sigma}_2) - A(\boldsymbol{\sigma}_1)}{A(\boldsymbol{\sigma}_1)}; \dots, \frac{A(\boldsymbol{\sigma}_i) - A(\boldsymbol{\sigma}_1)}{A(\boldsymbol{\sigma}_1)}; \dots, \frac{A(\boldsymbol{\sigma}_M) - A(\boldsymbol{\sigma}_1)}{A(\boldsymbol{\sigma}_1)} \right\} \in \mathbb{R}^{K \cdot (M-1)}.$$

The result of the previous classification step provides an approximated prior for the

difference of the conductivity with respect to the reference frequency:

$$\Psi_{\bar{\sigma}}(\boldsymbol{\sigma}) = \tau \|L_{\bar{\sigma}}^{\text{fd}}(\boldsymbol{\sigma}^{\text{fd}} - \bar{\boldsymbol{\sigma}}^{\text{fd}})\|^2. \quad (5.32)$$

where

$$\begin{aligned} \boldsymbol{\sigma}^{\text{fd}} &= \{\boldsymbol{\sigma}_2 - \boldsymbol{\sigma}_1; \dots; \boldsymbol{\sigma}_i - \boldsymbol{\sigma}_1; \dots; \boldsymbol{\sigma}_M - \boldsymbol{\sigma}_1\} \\ &\in \mathbb{R}^{N \cdot (M-1)}, \end{aligned} \quad (5.33)$$

and

$$\bar{\boldsymbol{\sigma}}^{\text{fd}} = \sum_j \zeta_{nj} \cdot m_{ij}^{\text{fd}} \Bigg|_{\text{MAP}(\zeta)} = m_{ij'}^{\text{fd}} \quad i = 2, \dots, M. \quad (5.34)$$

5.2.7 Frequency-difference classification

The reconstruction problem using difference data is no longer unique, however tissue-based clustering is observed in difference images given by $\boldsymbol{\sigma}_i - \boldsymbol{\sigma}_1 \ \forall i = 2, \dots, M$. Therefore the classification algorithm is performed on the set of images $\boldsymbol{\sigma}^{\text{fd}}$ (5.33) and the parameters of the relative spectra are updated. The implementation is otherwise the same as for the case of using absolute data.

5.2.8 Spatial smoothing

Spatial smoothing is introduced by adding a regularization term to the objective function (5.16),

$$\boldsymbol{\sigma} = \arg \min_{\boldsymbol{\sigma}} \frac{1}{2} \|\mathbf{L}_v(A(\boldsymbol{\sigma}) - \mathbf{v})\|^2 + \frac{\tau_1}{2} \Psi_s(\boldsymbol{\sigma}) + \frac{\tau_2}{2} \|L_{\bar{\sigma}}(\boldsymbol{\sigma} - \bar{\boldsymbol{\sigma}})\|^2, \quad (5.35)$$

where $\Psi_s(\boldsymbol{\sigma})$ assumes the general form of a Markov Random field

$$\Psi_s(\boldsymbol{\sigma}) = \sum_{i,n,m} w_{nl(n)} R(|\sigma_{ni} - \sigma_{l(n)i}|), \quad (5.36)$$

where $l(n)$ runs over the neighbours of the n th voxel, $w_{nl(n)}$ is a weighting factor, and R indicates a function of $|\sigma_{ni} - \sigma_{l(n)i}|$. In this chapter $R = |\sigma_{ni} - \sigma_{l(n)i}|^2$ is chosen, and either $w_{nl(n)} = 1$ (homogeneous MRF) or $w_{nl(n)} = \boldsymbol{\zeta}_n^T \cdot \boldsymbol{\zeta}_{l(n)}$ (label-dependent MRF).

5.2.9 Image quality evaluation

Three measures of error were considered in order to evaluate the quality of images recovered from simulated data. The first is the L_2 -norm of the difference between the recovered conductivity $\boldsymbol{\sigma}^{\text{recon}}$ and the numerical phantom $\boldsymbol{\sigma}^{\text{true}}$, expressed as a ratio of

the norm of the model and divided by the number of frequencies:

$$\text{Err}_{L_2} = \frac{1}{M} \sum_{i=1}^M \frac{\|\sigma_i^{\text{recon}} - \sigma_i^{\text{true}}\|}{\|\sigma_i^{\text{true}}\|}. \quad (5.37)$$

The second is the classification error $\text{Err}_{\text{class}}$, given by the percentage of misclassified elements in the mesh. The third is the mean error committed in approximating the spectra of the tissue classes:

$$\text{Err}_{\text{spectr}} = \frac{1}{M} \frac{1}{J} \sum_{i,j} \frac{|m_{ij} - \epsilon_{ij}|}{\epsilon_{ij}}, \quad (5.38)$$

where ϵ indicates the simulated conductivities of the tissues and m the means of the tissue conductivities recovered by the last classification step.

To evaluate images recovered from experimental data or obtained with other methods, the mean across frequencies of the contrast-to-noise ratio (CNR) was considered. Given a tissue t_j , $\text{CNR}(j)$ is defined as

$$\text{CNR}(j) = \frac{1}{M} \sum_{i=1}^M \frac{[\sigma_i^{p(j)} - \sigma_i^b]^2}{\text{std}(\sigma_i^b)^2}, \quad (5.39)$$

where std indicates the standard deviation, and $\sigma_i^{p(j)}$ and σ_i^b are the mean values of the image across the areas corresponding to, respectively, the perturbation made of the tissue t_j and the background. In the case of simulated data, the positions of the background and the perturbations were known exactly, and in the case of experimental data, the positions were estimated by measuring the location of the perturbations.

5.3 Results

5.3.1 Numerical phantom and data simulation

The numerical phantom described in section 3.3.8 was considered. The measured tissue spectra (figure 3.17) were assigned to the phantom (figure 3.18) to obtain the conductivity model (figure 5.1).

5.3.2 Reconstruction-classification method with homogeneous MRF regularization: numerical validation

Images were reconstructed by performing 6 iteration of the reconstruction-classification method (figures 5.2). Homogeneous Markov Random Field (hMRF) smoothing was

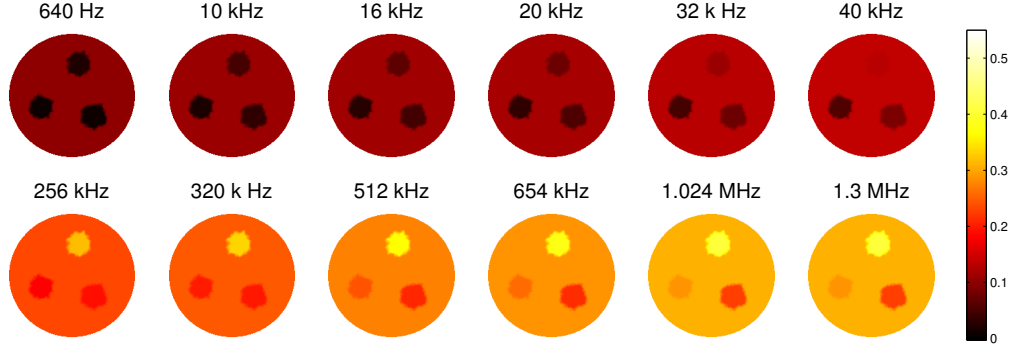


Figure 5.1: Numerical phantom: model of conductivity for all frequencies. Colorbar units are S/m .

applied (see equation (5.36))

$$\Psi_s(\boldsymbol{\sigma}) = \tau_1 \sum_{i,n,l(n)} |\sigma_{ni} - \sigma_{l(n)i}|^2. \quad (5.40)$$

The initial mean values of the spectra were set to the real simulated spectra ϵ (figure 3.17), and the covariance was set to $\boldsymbol{\Sigma}_j = 10^{-3}\mathbf{I}$ for all four tissues. The parameters of the inverse Wishart distribution were set to $\nu_1 = 20000$ and $\boldsymbol{\Gamma}_j = 10^{-2}\mathbf{I}$ for the background, and $\nu_j = 5000$ and $\boldsymbol{\Gamma}_j = 10^{-1}\mathbf{I}$ for the other tissues. The regularization parameters were set to $\tau_1 = 10^{-4}$ and $\tau_2 = 10^{-8}$. In all cases, conductivity images are displayed alongside scatter plots and responsibility images. The axis of the scatter plots are the projections onto the primary and secondary basis vectors of the conductivity images, which are obtained by taking the SVD decomposition of the matrix $\boldsymbol{\sigma} \in \mathbb{R}^{N \cdot M}$ (see section 2.5.3.1). Each point on the scatter plots corresponds to the projections a_1 and a_2 of the vector of conductivity values assumed for all frequencies by each voxel $\boldsymbol{\sigma}_{ni} = \{\sigma_{ni}; i = 1, \dots, M\}$. The responsibility images display the probability that each voxel is assigned to a certain tissue, as defined by equation (5.17).

5.3.3 Robustness to spectral errors

Errors were added to the conductivity value of each tissue before simulating the boundary voltage data at each frequency. Gaussian distributed errors were chosen with mean the value of the actual spectra used in the reconstruction ϵ (figure 3.17), and the study was repeated for increasing variance values: 1%, 5%, 10% and 20%. For each variance, the errors were sampled and the reconstruction was repeated 20 times. The parameters of the reconstruction-classification algorithm were set to those used in the numerical validation. Results for the voxel-wise variance of the MAP estimate of the labels are

presented (figure 5.3).

5.3.4 Reconstruction-classification with independent elements

Images were reconstructed without spatial smoothing. The initial covariance was set to $\Sigma_j = 10^{-3}\mathbf{I}$ for all tissues. The parameters of the inverse Wishart distribution were set to the same values as in section 5.3.1. The regularization parameter was $\tau_2 = 10^{-8}$ (and, obviously, $\tau_1 = 0$, $\Psi_s = 0$), and 6 iterations were performed (figure 5.4).

5.3.5 Reconstruction-classification with label-dependant MRF regularization

Images were reconstructed using the result of the classification step to qualify the regularization in the successive reconstruction step. The Markov Random Field regularization term is modified so that only neighbours with the same expected tissue labels, as given by (5.13), are considered. The MRF term becomes (equation (5.36))

$$\Psi_s(\boldsymbol{\sigma}) = \tau_1 \sum_{i,n,l(n)} \left(\zeta_n^{t^T} \cdot \zeta_{l(n)}^t \right) |\sigma_{ni} - \sigma_{l(n)i}|^2,$$

where ζ_n^t indicates the labels assigned at the previous iteration, and

$$\zeta_n^{t^T} \cdot \zeta_{l(n)}^t = \begin{cases} 1 & \text{if } \zeta_{nj}^t = \zeta_{l(n)j}^t \quad \forall j, \\ 0 & \text{otherwise.} \end{cases} \quad (5.41)$$

The parameters of the reconstruction-classification algorithm were set to the same values used in 5.3.1. Images of the numerical phantom were reconstructed by performing 6 iterations of reconstruction-classification (figure 5.5).

5.3.6 Frequency-difference reconstruction-classification: numerical validation

The first classification step was set up using the result of the first reconstruction step: the initial guess for the mean and variance of the classes was set to that of the region of the image corresponding to each tissue. The parameters of the inverse Wishart distribution were set to $\nu_1 = 20\,000$ and $\Gamma_j = 10^{-2}\mathbf{I}$ for the background, and $\nu_j = 5000$ and $\Gamma_j = 10^{-1}\mathbf{I}$ for perturbation. Label-dependent MRF regularization was applied, and the regularization parameters were set to $\tau_1 = 10^{-4}$ and $\tau_2 = 10^{-8}$, and 6 iterations were performed (figure 5.7).

5.3.7 Image quality evaluation

The results obtained using the reconstruction classification method with homogeneous MRF regularization (section 5.3.2, figure 5.2), independent elements (section 5.3.4, figure 5.4), label-dependent MRF regularization (section 5.3.5, figure 5.5), and frequency-difference data with label-dependent MRF regularization (section 5.7, figure 5.7) were evaluated by our image quantification method (section 5.2.9) and compared (figure 5.8).

5.3.8 Comparison with other methods

The reconstruction-classification images were compared to pre-existing static EIT imaging methods. Absolute conductivity images were obtained using the damped Gauss-Newton algorithm [53]. An image of the conductivity was obtained independently for each frequency by minimizing

$$\sigma_i = \arg \min_{\sigma_i} \frac{1}{2} \|A(\sigma_i) - \mathbf{v}_i\|^2 + \frac{\tau}{2} \sum_{n, l(n)} |\sigma_{ni} - \sigma_{l(n)i}|^2, \quad (5.42)$$

where MRF regularization was chosen and the regularization parameter was set to the same value used for the reconstruction-classification algorithm $\tau = 10^{-8}$. Six iterations were performed (figure 5.9a).

Images were obtained using the linear weighted frequency-difference method [97, 58, 3, 83]. An image of weighted frequency-difference conductivity

$$\Delta \sigma(\omega_1, \omega_i) = \delta \cdot \sigma(\omega_i) - \sigma(\omega_1) \quad (5.43)$$

was reconstructed $\forall i = 2, \dots, M$, where $\delta = \frac{\langle \mathbf{v}(\omega_2), \mathbf{v}(\omega_1) \rangle}{\langle \mathbf{v}(\omega_1), \mathbf{v}(\omega_1) \rangle}$ and the following conditions must be satisfied:

1. $\Delta \sigma(\omega_1, \omega_i) \approx 0$ near the boundary $\delta\Omega$
2. $\Delta \sigma(\omega_1, \omega_i) \gg 0$ on the perturbation.

MRF regularization was applied, and the pseudo-inverse of the Jacobian was found using modified tSVD [44]. The optimum number of singular values was selected via the L-curve method [42] (figure 5.9b). The absolute (DGN) and weighted frequency-difference (WFD) images were evaluated and compared to the label-dependent MRF (ldMRF) case by calculating the mean contrast-to-noise ratio (5.39) for each tissue (Table 5.1).

	ldMRF	DGN	WFD
Potato	22.63	12.88	9.11
Banana	23.03	19.82	5.78
Cucumber	20.28	13.95	7.05

Table 5.1: Table of contrast values obtained using label-dependent MRF (ldMRF) with reconstruction-classification, absolute (DGN), and weighted frequency-difference (WFD) imaging.

5.3.9 Phantom experiment

The tank phantom and experimental setup are described in section 3.3.4. The initial mean of the spectra was set to values measured with the impedance analyser (section 3.3.1), and the covariance was set to $\Sigma_j = 10^{-2}\mathbf{I}$ for the background, and $\Sigma_j = 10^{-3}\mathbf{I}$ for the perturbation. The parameters of the inverse Wishart distribution were set to $\nu_1 = 10^6$ and $\mathbf{\Gamma}_j = 10^{-1}\mathbf{I}$ for the background, and $\nu_j = 20000$ and $\mathbf{\Gamma}_j = 10^{-3}\mathbf{I}$ for perturbation. Images were reconstructed using absolute (figure 5.10) and frequency-difference (figure 5.11) data using label-dependent MRF regularization. The regularization parameters were set to $\tau_1 = 10^{-4}$, $\tau_2 = 10^{-8}$ for absolute data and $\tau_1 = 10^{-3}$, $\tau_2 = 10^{-8}$ for frequency-difference data. Six iterations of both reconstruction and classification steps were performed in all cases. The images were evaluated objectively by calculating the average over frequencies of the contrast-to-noise ratio of the perturbation in the conductivity images. Using absolute data the mean CNR was 9.3 and 9.61 respectively for positions (−4 cm 0 cm 0 cm) and (0 cm +4 cm 0 cm), and using frequency-difference data the CNR was significantly lower at 3.22 and 5.

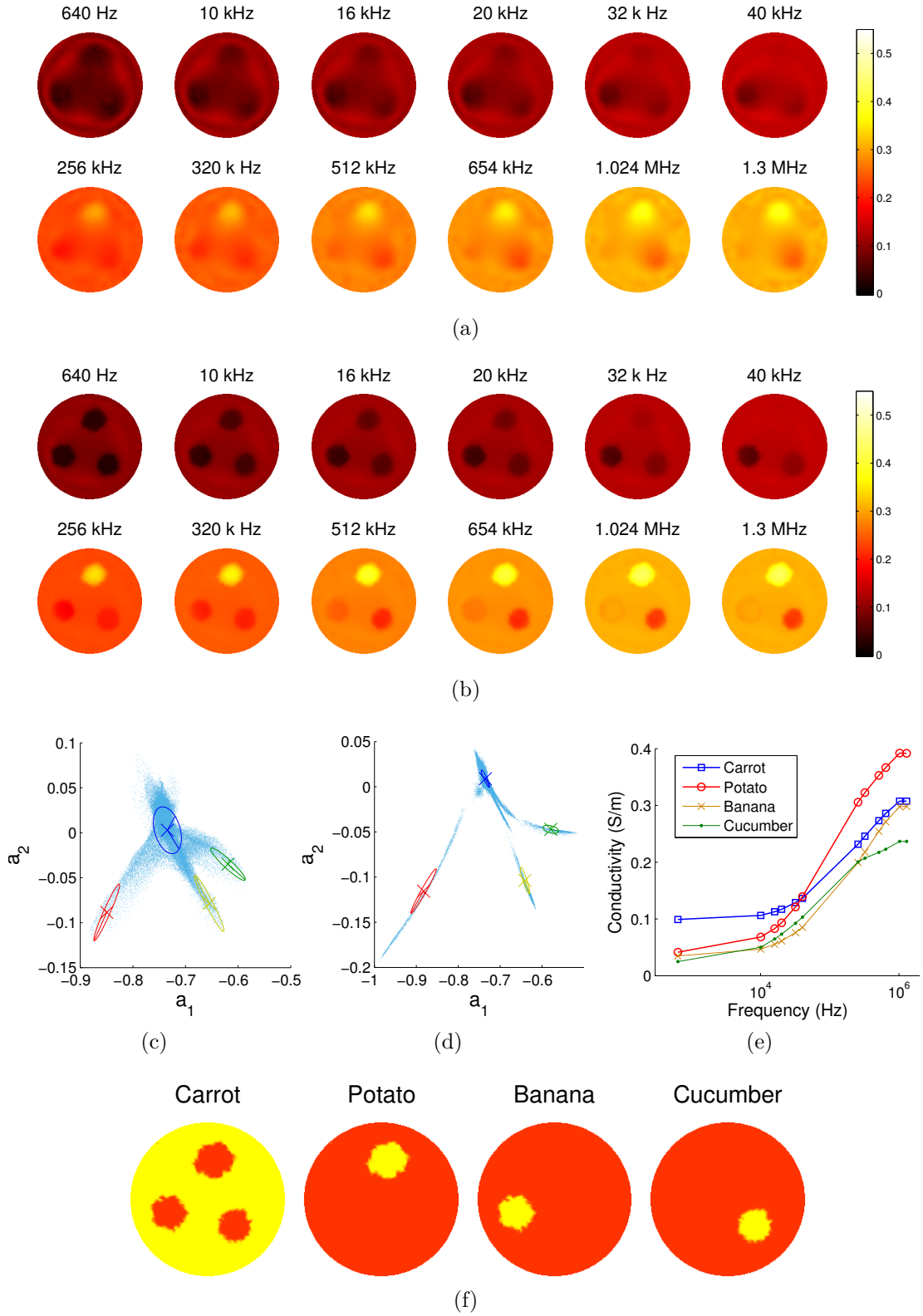


Figure 5.2: Reconstruction-classification with homogeneous MRF: conductivity at (a) iteration 1 and (b) iteration 6 (final) (scale is S/m); scatter plots of the projection onto the primary a_1 and secondary a_2 eigenvectors of the conductivity images at (c) iteration 1 and (d) iteration 6 (the cross indicates the mean, the ellipse the variance, and the colour map is: blue-carrot, red-potato, yellow-banana, green-cucumber); (e) mean conductivity spectra m and (f) responsibility (5.17) recovered at final iteration.

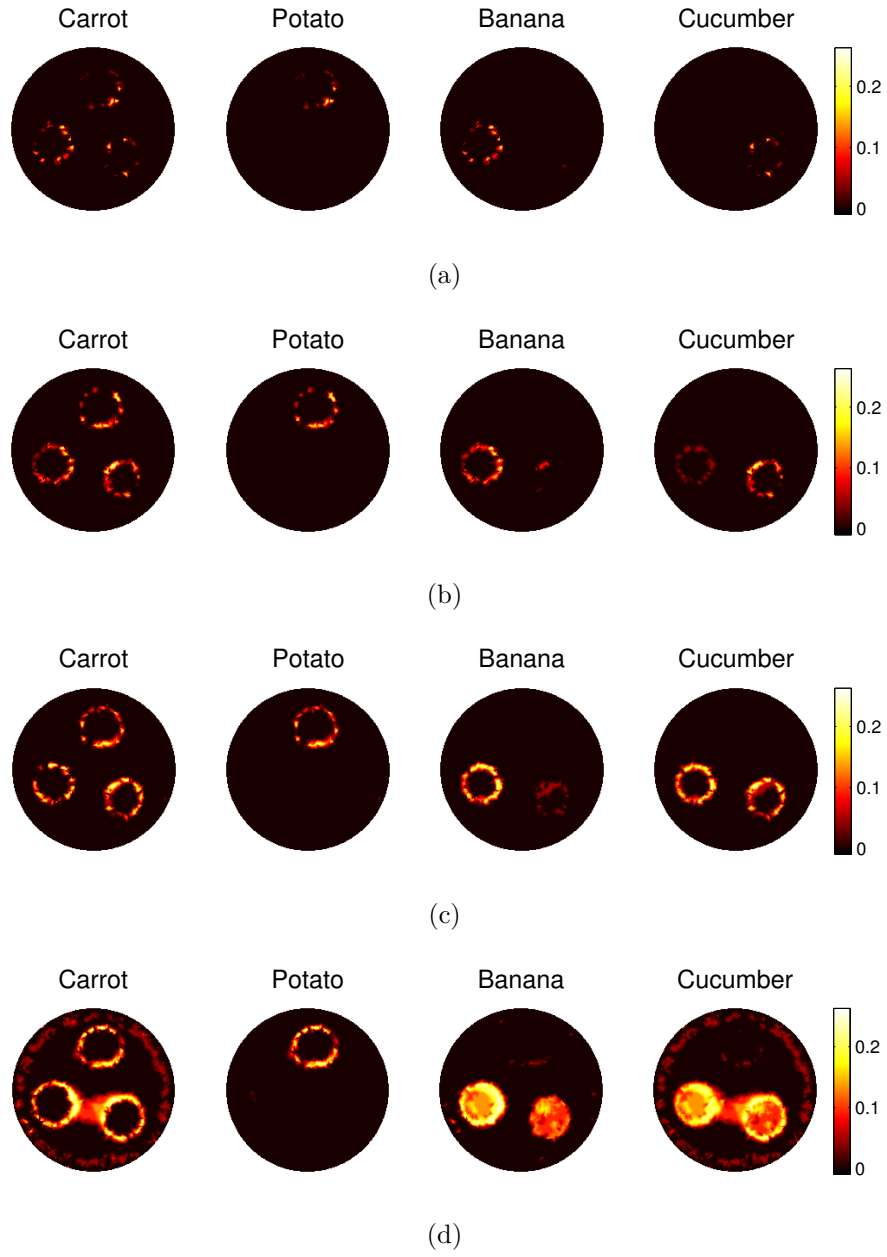


Figure 5.3: Robustness to errors in the initial guess of the tissue spectra: images of variance over 20 trials of the labels obtained after adding errors to the tissue spectra with variance 1% (a), 5% (b), 10% (c) and 20%(d).

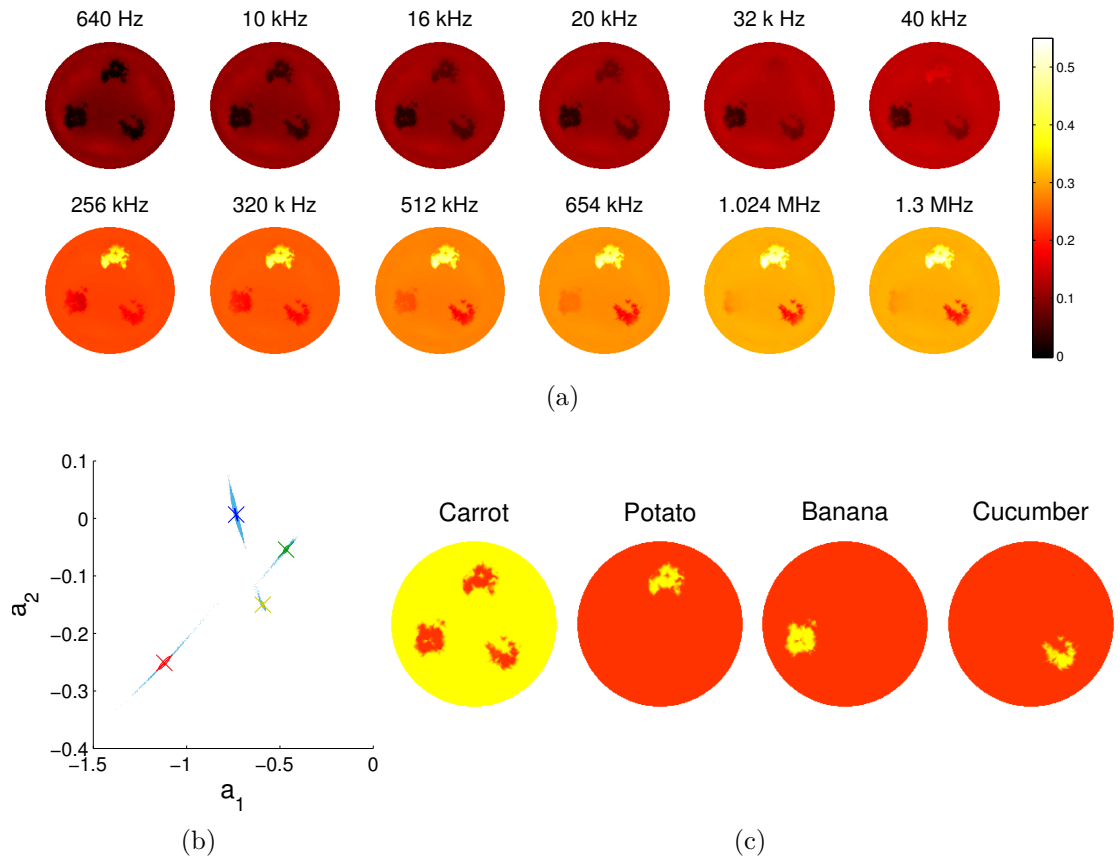


Figure 5.4: Reconstruction-classification in the case of independent elements: (a) conductivity (scale is S/m), (b) and scatter plot at final iteration and (c) responsibility.

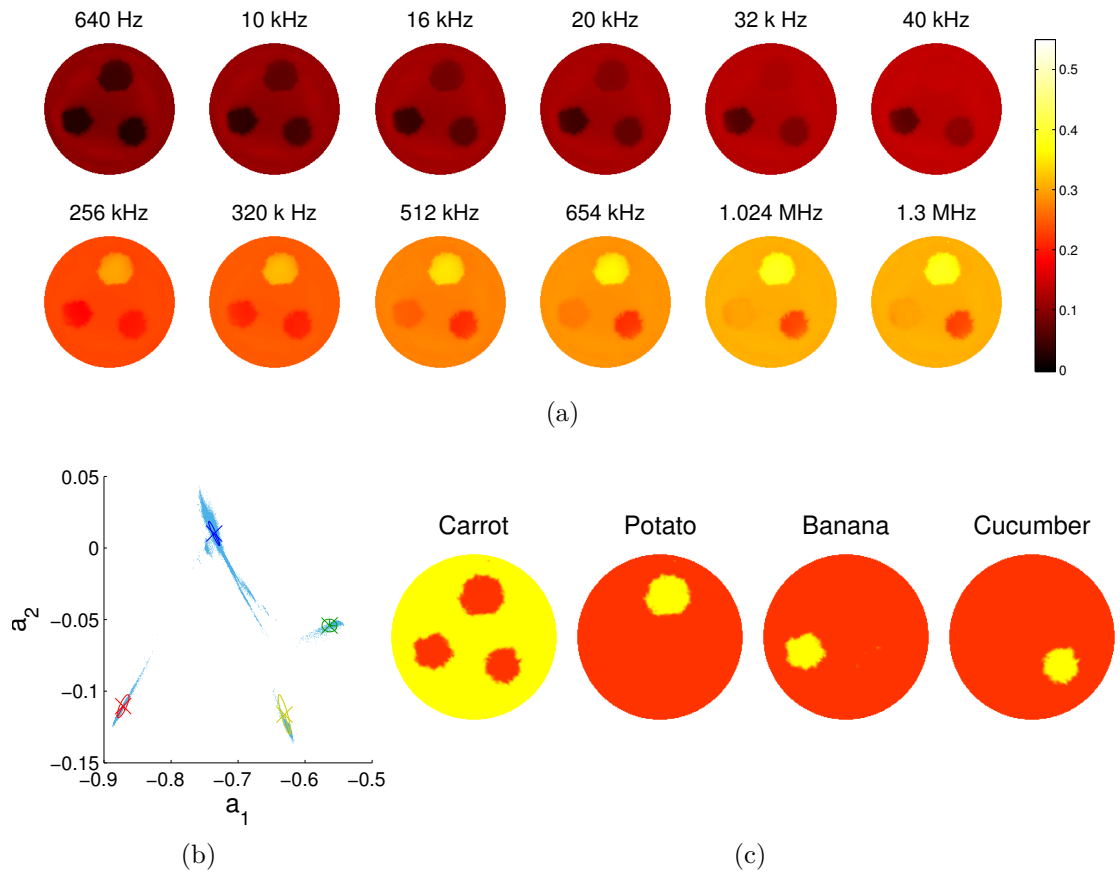
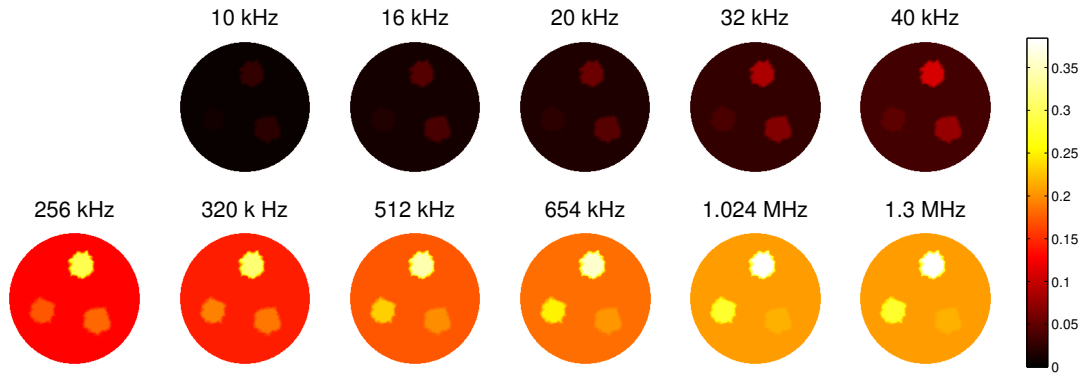
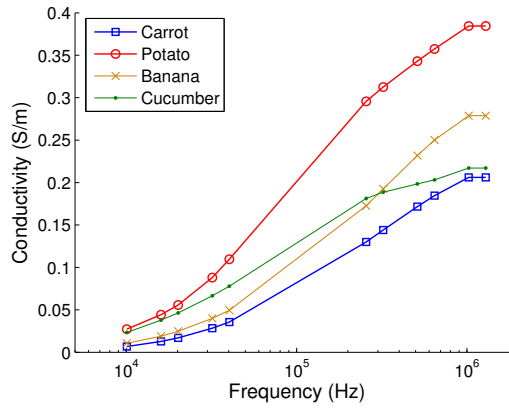


Figure 5.5: Reconstruction-classification with label-dependent MRF: (a) conductivity (scale is S/m), (b) and scatter plot at final iteration and (c) responsibility.



(a)



(b)

Figure 5.6: Frequency-difference reconstruction-classification model: (a) frequency-difference conductivity model for all frequencies (scale is S/m); (b) relative frequency-difference conductivity spectra of the tissues ϵ^{fd} in S/m .

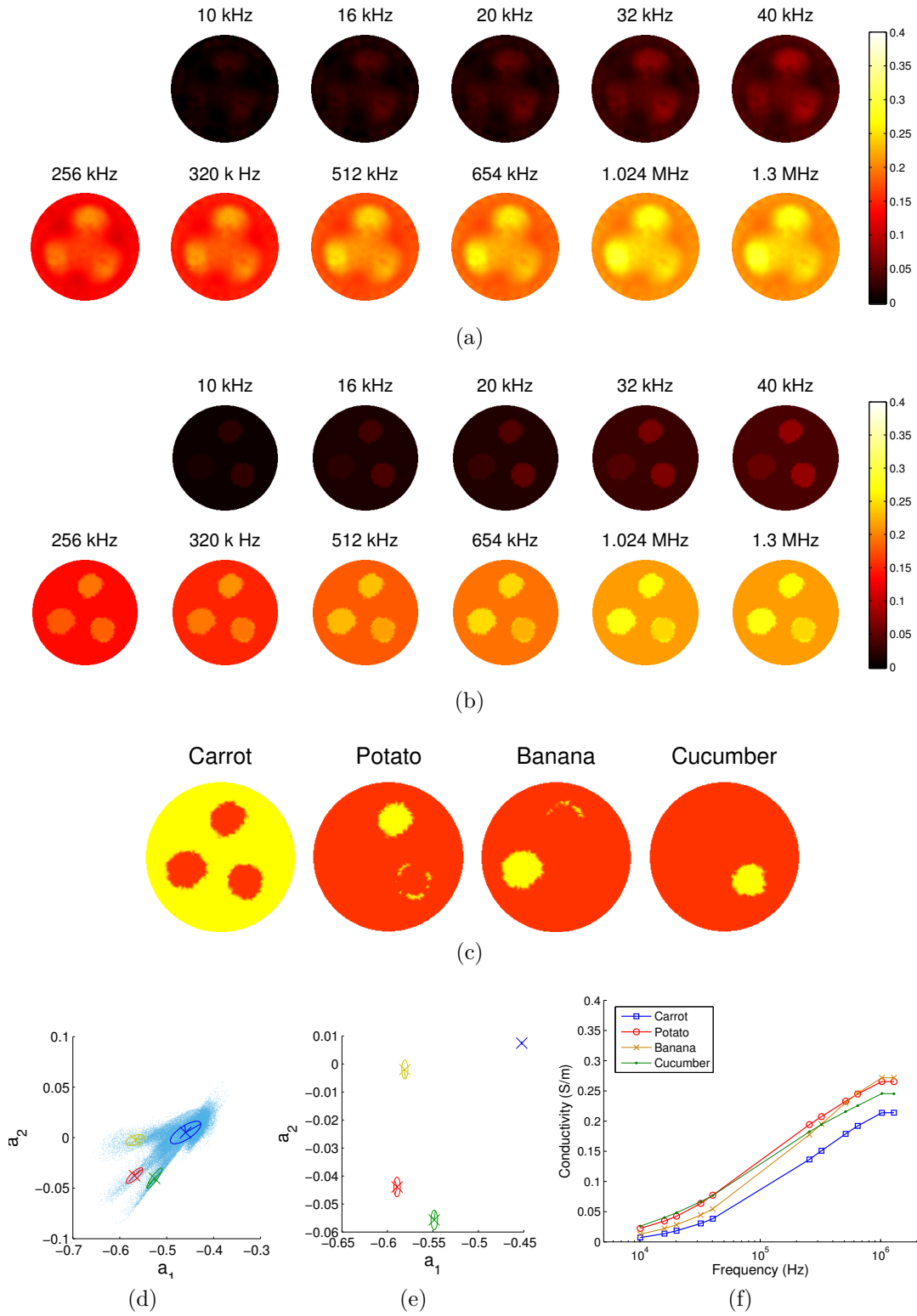


Figure 5.7: Frequency-difference reconstruction-classification results: frequency-difference conductivity images obtained at (a) iteration 1 and (b) iteration 6 (final) (scale is S/m); (c) responsibility at final iteration; scatter plots at (d) iteration 1 and (e) iteration 6; (f) mean frequency-difference conductivity spectra m^{fd} recovered by the reconstruction-classification method in S/m .

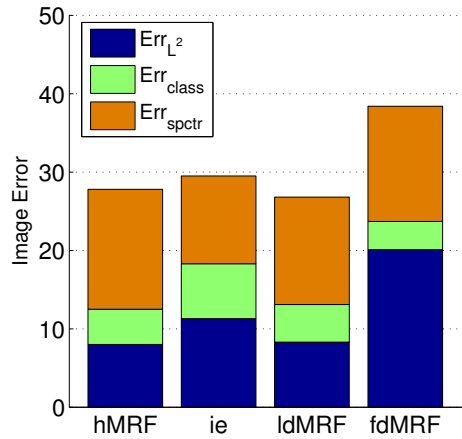


Figure 5.8: Image quality of numerical results: reconstruction classification method with homogeneous MRF (hMRF), independent elements (ie), label-dependent MRF (ldMRF), and frequency-difference with label-dependent MRF (fdMRF)

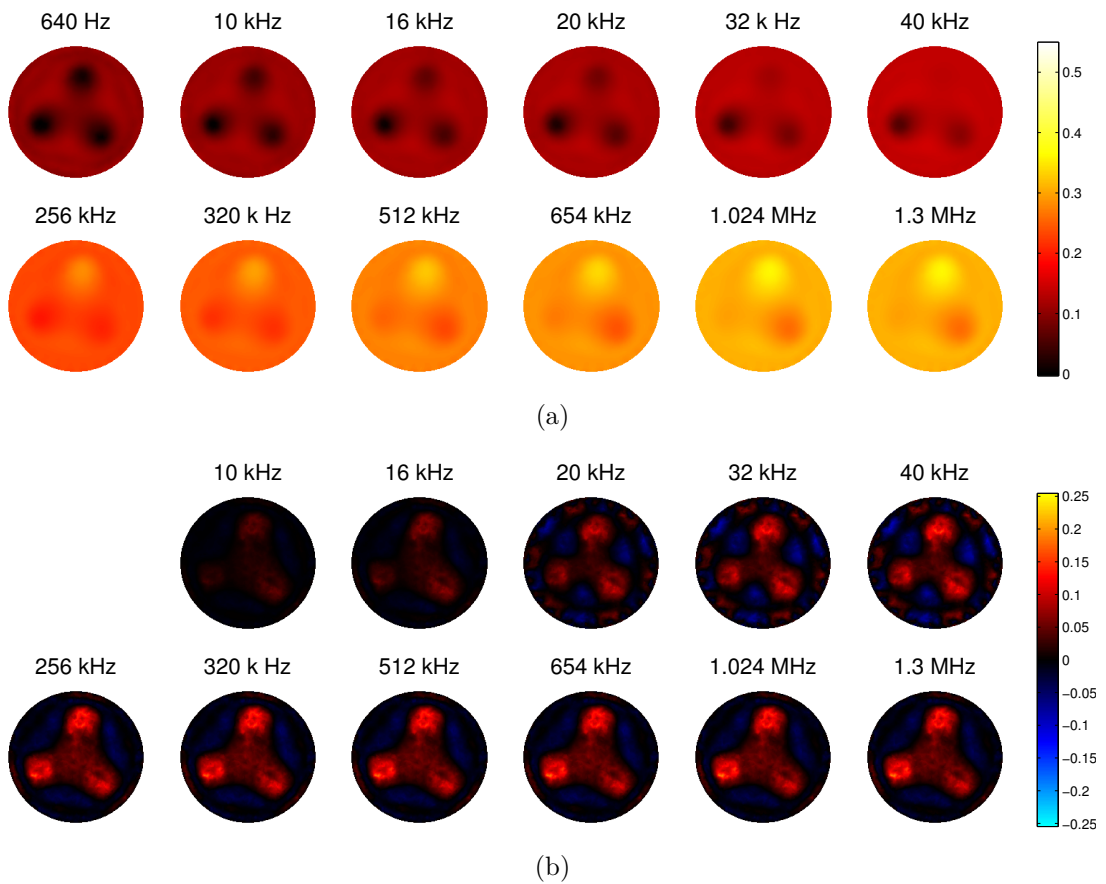
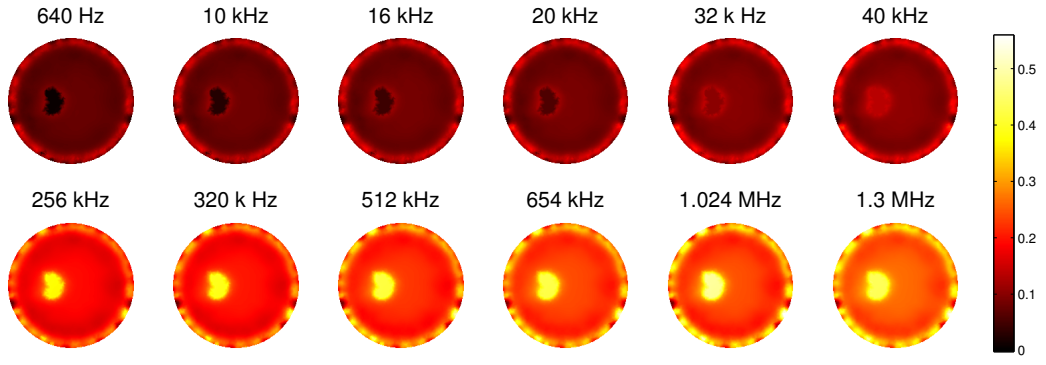
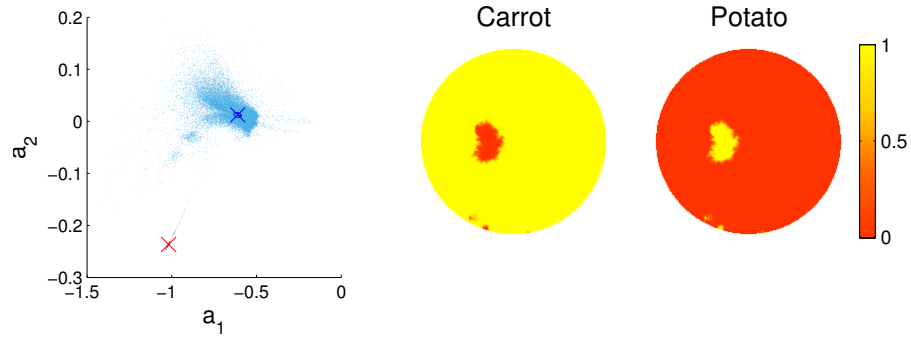


Figure 5.9: Comparison with other methods: (a) absolute conductivity images obtained using damped Gauss-Newton (scale is conductivity S/m), and (b) weighted frequency-difference images of the numerical phantom (scale is weighted conductivity difference S/m).

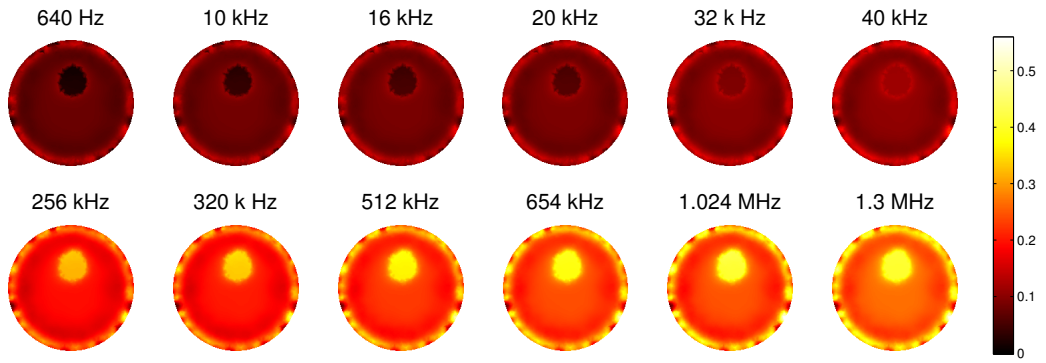


(a)

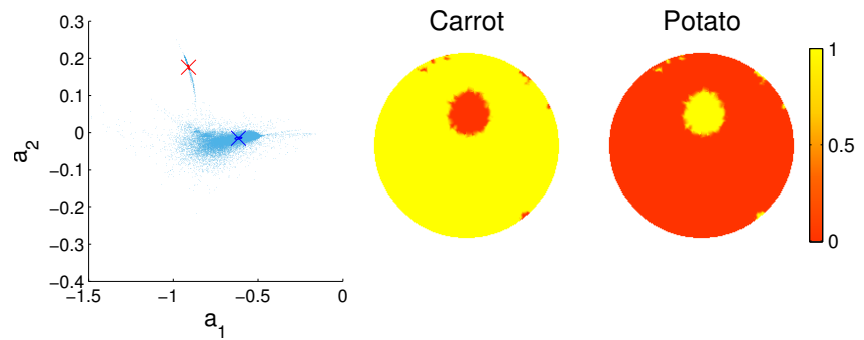


(b)

(c)



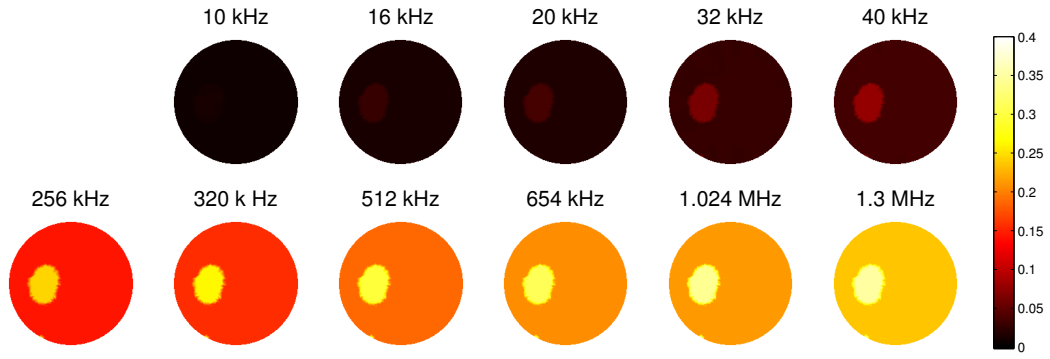
(d)



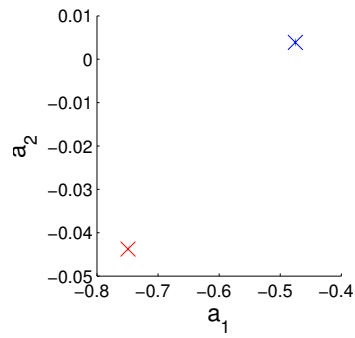
(e)

(f)

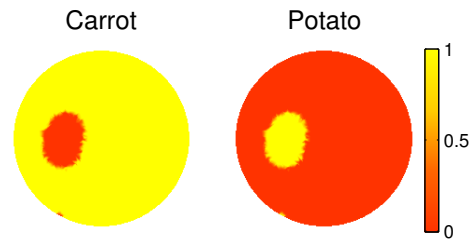
Figure 5.10: Phantom experiment setup and reconstruction-classification results for absolute data: conductivity image (scale is S/m), scatter plot and responsibility image for (a)–(c) position $(-4\text{ cm } 0\text{ cm } 0\text{ cm})$ and (d)–(f) position $(0\text{ cm } +4\text{ cm } 0\text{ cm})$.



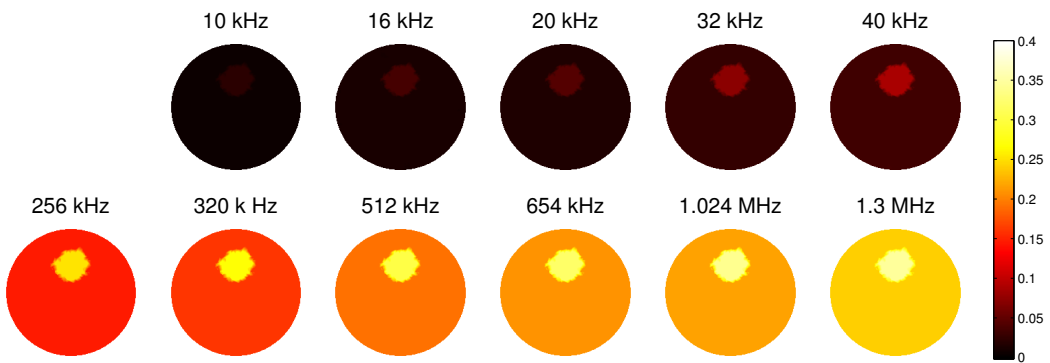
(a)



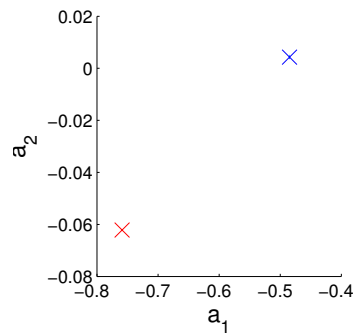
(b)



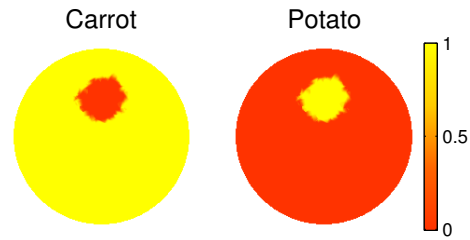
(c)



(d)



(e)



(f)

Figure 5.11: Phantom experiment reconstruction-classification results for frequency-difference data: (a) conductivity image (scale is S/m) and (b) scatter plot and (c) responsibility image for position $(-4 \text{ cm } 0 \text{ cm } 0 \text{ cm})$; (d) conductivity image (scale is S/m), (e) scatter plot and (f) responsibility image for position $(0 \text{ cm } +4 \text{ cm } 0 \text{ cm})$.

5.4 Discussion

5.4.1 Numerical results obtained with homogeneous MRF, independent elements and label-dependent MRF

The choice of introducing homogeneous Markov Random field regularization had the effect of increasing the error in the estimation of the tissue spectra. This was visible in the "streaking" between the clusters in the scatter plots (see figure 5.2). The reason for this is that the hMRF regularization favours spatially smooth solutions. Therefore, instead of a jump-change in the conductivity of areas assigned to different tissues, elements along the boundary between tissues assumed intermediate conductivity values. These elements caused an increase in the covariance associated to the tissue classes. In the final image, the largest eigenvalue of the covariance of each perturbation class corresponded to the direction of the line joining the mean conductivity of the perturbation to that of the background. However, from the comparison with the case of independent elements (no spatial smoothing, figure 5.4) it was evident that the use of hMRF regularization had the effect of significantly improving the overall image quality, as reflected by the reduction in the L_2 -norm and the classification errors (figure 5.8).

The choice to use the result of the classification step to qualify the successive reconstruction step by using label-dependant MRF allowed for sharp edges between tissues whilst favouring large homogeneous areas. Neighbouring voxels that were assigned to different tissues in the previous classification step were not considered in the calculation of the regularization term; therefore elements lying along the edge between tissues assumed a conductivity closer to the mean of one or the other tissue. This modification returned an improvement in the spectral errors with respect to hMRF.

5.4.2 Robustness to spectral errors

The variance of the labels obtained after adding errors to the initial guess of the tissue spectra was found to be very low. This result indicated that the classification step corrected the estimate of the tissue properties. For an error of 10% or less, misclassified elements are limited to the boundary between tissues, and only in the case of 20% error the banana and cucumber perturbations are sometimes confused.

5.4.3 Frequency-difference combined reconstruction-classification

The advantage of using frequency-difference data in the image reconstructions was that the result was more robust to modelling errors. The sensitivity of the method to errors in the geometry of the boundary, the localization and shape of the electrodes, and contact

impedance is higher if absolute data is used. In an experimental setup, this may result in severe edge artefacts, which can significantly affect image quality. The effect of referring the data to a low frequency is the suppression of frequency-independent modelling and instrumentation errors, in the same way that the use of time-difference data allows for the suppression of time-independent errors.

The disadvantage to using frequency difference data is that the number of data points is reduced from $K \cdot M$ to $K \cdot (M - 1)$, whereas the number of unknown remains constant N . Also, the reconstruction problem is no longer unique. The reconstructed absolute values are therefore not expected to agree with the simulated model. Therefore, tissues are distinguished only by the difference in the relative slope of the spectrum, rather than the absolute conductivity values, and this can result in a loss in contrast.

In conducting the simulation study (section 5.3.6, figures 5.7 and 5.8), it proved difficult to perform the correct classification of the tissues when the class means were initialized to the expected values ϵ , and the class variances were set to a multiple of the identity matrix. The reason for this is that the conductivity values recovered by the first reconstruction step were too distant from the real values. Instead, following the method used in [45], the parameters were initialized using the result of the first reconstruction step. This requires knowledge of the approximate location of the perturbation tissues, which may either be held *a priori*, or may also be gained from the first reconstruction result. In this case the data was simulated, and the region of interest corresponding to the location of each tissues was already known. However in an experimental setup it would have been necessary to view the first reconstructed image and select the areas corresponding to significant perturbations. This could be achieved either manually, by visualizing the result, or by choosing an automatic criterion. For example, the image could be thresholded to consider voxels with significant variations from the background value as "other than the background tissue". Then the perturbation tissues could be distinguished by finding neighbouring clusters of voxels, and considering each cluster as a distinct tissue.

5.4.4 Comparison with other methods

The same numerical problem was considered, and equivalent images were reconstructed using alternative methods. The contrast-to-noise ratio obtained with the reconstruction-classification method was superior to that obtained using absolute and weighted frequency-difference imaging for all tissues. The reconstruction-classification method holds a further advantage over the weighted frequency-difference method in that the application of the

latter is limited by restrictive assumptions (see 5.3.8). However, if absolute data is used, the reconstruction-classification method is equally sensitive to modelling errors as the absolute conductivity method.

5.4.5 Phantom experiment

The phantom experiment was designed to highlight the effect of using frequency-difference data in the reconstruction. The images recovered from absolute data (figure 5.10) presented a ring-shaped artefact around the edge of the tank. This was caused by the mismatch between the model and the real shape of the boundary and electrodes, electrode localization, contact impedance, and instrumentation errors [13, 62]. The errors were most evident near the electrodes because the sensitivity to noise is highest in the areas where the current density is highest.

The use of frequency-difference data allowed for the subtraction of frequency-invariant errors in the data, and thus resulted in the suppression of the boundary artefact (figure 5.11). However, information about the absolute values of the conductivity of the tissues was lost, and the recovered contrast was lower with respect to the case of absolute data (section 5.3.9). As the observer is likely to be most sensitive to the appearance of the artefacts, the use of frequency-difference data has the effect of improving the overall visual quality of the image. However, the images obtained from absolute data contain relatively more information about the conductivity of the object, and perform better in terms of an objective evaluation measure.

5.5 Conclusion

A combined reconstruction-classification method for MFEIT was proposed. The novelty of the method lies in the simultaneous estimation of the conductivity and the spectra of the tissues in the domain. This allows for the use of the spectral information in the reconstruction step, while the constraints are updated in the classification step to correct possible errors in the initial assumptions.

The robustness of the method to errors in the initial guess of the tissue spectra was demonstrated. Alternative choices of regularization were compared, and it was found that it is preferable to introduce spatial smoothing, and that edges can be enhanced by using the classification result to inform the regularization in the reconstruction step. A frequency-difference variant of the method was formalized and validated. Absolute and frequency-difference reconstruction-classification was applied to phantom data collected in a tank, and it was found that the use of frequency-difference data results in the

suppression of edge artefacts, but also in a reduction in contrast.

Further work is necessary to compare the performance of the reconstruction classification method using absolute and frequency-difference data. The results are likely to be dependant on the spectra of the tissues involved, and on the distance of the anomalies from the electrodes. Further analysis is required to investigate the robustness of the method to modelling errors such as erroneous electrode location and contact impedance. The method could also be improved by modifying the prior distribution of the spectral properties of the tissues to include information about cross-frequency correlation.

Chapter 6

Reconstruction-classification using graph cut optimization

6.1 Introduction

6.1.1 Overview

The reconstruction-classification algorithm discussed in the previous chapter allows for the inclusion of spectral information in the reconstruction step, while the spectral model is improved by the classification step. The addition of a spatial prior on the conductivity was investigated as a means to improve image quality. In this chapter, a more rigorous approach to spatial smoothing in the reconstruction-classification method is pursued. A method is devised to allow for the inclusion of a spatial prior on the labels, rather than the conductivity. This approach is formalized and justified in the Bayesian framework. As in the previous chapter, the method is tested on the simulated and phantom data, and the results are compared.

6.1.2 Related work

The graph cut optimization algorithm described in section 2.7.3 is suitable for classifying piecewise constant images with known level sets. A method known as *Grabcuts* extends graph cuts to allow for a statistical *appearance model* for the image, such as a mixture of Gaussians model [94, 120]. In the Grabcut method, the result of the graph cut step is used to define a hard classification of the image voxels, and the parameters of the Gaussian model are updated simply by taking the mean and variance of each class. A different approach is needed in order to allow for a soft classification of the image because computing the conditional probability in the E-step is mathematically intractable in the MRF framework. The *hidden MRF* model [121] was developed to overcome this problem: the result of the labelling step is used to calculate the mixed probability term

in the E-step and update the class parameters.

6.1.3 Purpose

In this chapter, a method is presented for including a spatial prior on the tissue labels in a reconstruction-classification scheme. A *hidden Markov random field* model is defined on the labels, and *graph cut optimization* is applied to solving the labelling problem. The method is validated on simulated data, the robustness to spectral errors is investigated, and the method is applied to experimental phantom data.

6.1.4 Experimental design

6.1.4.1 Numerical validation

The reconstruction-classification method using graph cut optimization was validated on the same numerical example considered in the previous chapter (section 5.3.2). The aim was to compare results obtained with the spatial prior placed on the conductivity and on the labels. Images were evaluated by an objective measure of image quality.

6.1.4.2 Robustness to spectral errors

A robustness test was performed to evaluate the ability of the algorithm to correct for errors in the initial spectral model. The reconstruction was repeated after adding errors to the initial guess of the spectral parameters, and the variance of the reconstructed images was assessed. Results were compared to those obtained in the previous chapter (section 5.3.3).

6.1.4.3 Phantom experiment

The method was applied to experimental phantom data measured previously (section 3.3.4) and evaluated in terms of the recovered contrast-to-noise ratio.

6.2 Method

In this section, a formulation of the reconstruction-classification method in the Bayesian sense is provided. First, the expression for recovering conductivity from voltage measurements is derived explicitly, then the solution to the labelling problem and the update rules for the spectral model parameters are obtained.

6.2.1 Bayesian formulation of the inverse problem of EIT

In Bayesian inversion, given the boundary voltage measurements \mathbf{v} , the maximum-a-posteriori (MAP) estimate of the conductivity $\boldsymbol{\sigma}$ is obtained by minimizing

$$\begin{aligned}\boldsymbol{\sigma} &= \arg \max_{\boldsymbol{\sigma}} p(\mathbf{v}|\boldsymbol{\sigma})p(\boldsymbol{\sigma}) \\ &= \arg \min_{\boldsymbol{\sigma}} \mathcal{L}(\boldsymbol{\sigma}, \mathbf{v}) + \tau\Psi(\boldsymbol{\sigma}),\end{aligned}\tag{6.1}$$

where $\mathcal{L}(\boldsymbol{\sigma}, \mathbf{v}) = -\log p(\mathbf{v}|\boldsymbol{\sigma})$ is the negative log-likelihood of measuring \mathbf{v} given the conductivity $\boldsymbol{\sigma}$, $\Psi = -\log p(\boldsymbol{\sigma})$ is the negative log of the prior, and τ is the regularization parameter. Assuming that the measurement noise is Gaussian distributed, and highlighting the dependence of the variables on the modulation frequency of the current ω , the objective function becomes

$$\boldsymbol{\sigma}(\omega) = \arg \min_{\boldsymbol{\sigma}(\omega)} \frac{1}{2} \|A(\boldsymbol{\sigma}(\omega)) - \mathbf{v}(\omega)\|_{\boldsymbol{\Sigma}_v^{-1}}^2 + \tau\Psi(\boldsymbol{\sigma}(\omega)),\tag{6.2}$$

where $A(\boldsymbol{\sigma}(\omega)) : \boldsymbol{\sigma}(\omega) \rightarrow \mathbf{v}(\omega)$ is the forward map and $\boldsymbol{\Sigma}_v$ is the covariance of the measurement noise.

6.2.2 Labelling in MFEIT

The segmentation problem can be interpreted as a multinomial labelling problem, where the aim is to assign to each voxel a vector that identifies a single tissue. As in the previous chapter, the number of tissues, or classes, is equal to the number of tissues that have distinct spectra.

Supposing that a multifrequency set of EIT images was recovered by some imaging method, we define

$$\boldsymbol{\sigma}_n = \sigma_{ni}; \quad \forall i = 1, \dots, M.\tag{6.3}$$

as the array of conductivity values taken by the n th voxel for each frequency $i = 1, \dots, M$, where M is the number of frequencies. Whereas in the imaging problem the conductivity is the unknown recovered by the optimization process, in the segmentation problem the image provides the observed data and the unknowns are the labels. The task is to assign each voxel a vector $\boldsymbol{\zeta}_n$ that identifies a single tissue

$$\zeta_{nj} = \begin{cases} 1 & \text{if the } j\text{th tissue is assigned to the } n\text{th voxel;} \\ 0 & \text{otherwise.} \end{cases}\tag{6.4}$$

From equation (2.126) we have that the labelling problem is solved by maximizing the MAP

$$\zeta = \arg \max_{\zeta} \prod_{n=1}^N p(\sigma_n | \zeta_n) p(\zeta), \quad (6.5)$$

which gives us an energy minimization problem.

6.2.3 Hidden Markov Random field model

A *hidden Markov Random field model* (HMRF) describes a random variable generated by an MRF field which can only be observed through measurement of another dependent variable. We assume that

- the labels constitute a hidden Markov random field $\zeta = \{\zeta_n; n = 1, \dots, N\}$ with known probability distribution $p(\zeta)$;
- the conductivity is an observable variable $\sigma = \{\sigma_n; n = 1, \dots, N\}$ with known conditional probability $p(\sigma_n | \zeta_n)$;
- we have *conditional independence* whereby

$$p(\sigma | \zeta) = \prod_{n=1}^N p(\sigma_n | \zeta_n), \quad (6.6)$$

which means that the conductivity of the n th voxel is dependent only on the corresponding label ζ_n (figure 6.1).

6.2.4 Gaussian HMRF model

A Gaussian model is chosen for the *emission probability* of the conductivity, that is the conditional dependence of the conductivity of the n th voxel given the corresponding label assignment,

$$\begin{aligned} p(\sigma_n | \theta_j) &= p(\sigma_n | \zeta_{nj} = 1, \theta_j) \\ &= \frac{1}{\sqrt{(2\pi)^J |\Sigma_j|}} \exp \left(-\frac{1}{2} (\sigma_n - \mathbf{m}_j)^T \Sigma_j^{-1} (\sigma_n - \mathbf{m}_j) \right) \\ &= \mathcal{N}(\sigma_n | \mathbf{m}_j, \Sigma_j), \end{aligned} \quad (6.7)$$

where $\mathbf{m}_j = \{m_{ij}; i = 1, \dots, M\}$ is the mean and $\Sigma_j \in \mathbb{R}^{M \times M}$ is the covariance matrix of the spectrum of the j th tissue.

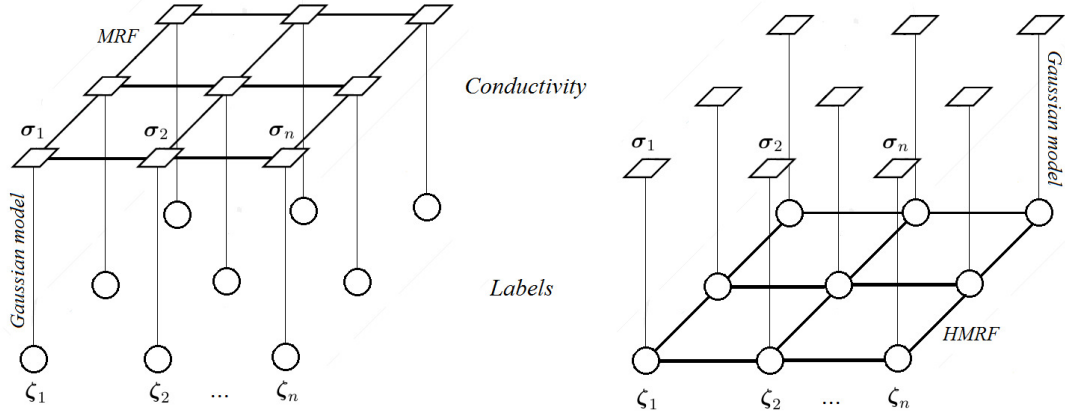


Figure 6.1: Schematic representation of the prior models used in the reconstruction-classification algorithms for a 3x3 voxel example: the conductivity values are shown as squares, the labels as circles, and the links indicate statistical dependence. In the left figure, the model used in chapter 5 is shown: the conductivity of each voxel depends on both the assigned label and the conductivity of the neighbouring voxels. This corresponds to an MRF prior on the conductivity (in this example the prior is homogeneous as each voxel is linked to all of its neighbours). In the right figure, the model used in this chapter is shown: the conductivity of each voxel depends only on the assigned label, and the values of the labels depend on the neighbouring voxels. This corresponds to a hidden MRF prior on the labels.

6.2.5 Gaussian HMRF model-based labelling in MFEIT

An *appearance model* is included in the labelling problem to describe the statistical distribution of the conductivity image for a given set of labels

$$p(\sigma_n | \zeta_n) \rightarrow p(\sigma_n | \zeta_n, \theta) = \prod_{j=1}^J [p(\sigma_n | \theta_j)]^{\zeta_{nj}}, \quad (6.8)$$

where θ indicates the parameters of the appearance model. Substituting into (6.5) the problem becomes

$$\zeta = \arg \max_{\zeta} \prod_{n=1}^N \prod_{j=1}^J [p(\sigma_n | \theta_j)]^{\zeta_{nj}} \cdot p(\zeta). \quad (6.9)$$

For a Gaussian emission model for the conductivity (6.7) we have, up to a constant,

$$\zeta = \arg \min_{\zeta} \sum_{n=1}^N \sum_{j=1}^J \zeta_{nj} \frac{1}{2} (\sigma_n - \mathbf{m}_j)^T \Sigma_j^{-1} (\sigma_n - \mathbf{m}_j) + \Psi(\zeta). \quad (6.10)$$

For a pair-wise HMRF prior on the labels we have

$$\begin{aligned}
 p(\zeta) &= \prod_{n=1}^N p(\zeta_n | \zeta_{l \in \mathcal{N}_n}) \\
 &= \prod_{n=1}^N \prod_{j=1}^J p(\zeta_{nj} = 1 | \zeta_{l \in \mathcal{N}_n}) \\
 &= \prod_{j=1}^J \lambda_j \prod_{n=1}^N \prod_{l \in \mathcal{N}_n} \exp(-\xi_{nl(n)} R(\zeta_n, \zeta_l))
 \end{aligned} \tag{6.11}$$

where λ_j is the overall probability of a tissue being assigned to the j th class, $\xi_{nl(n)}$ is a weighting factor, and

$$R(\zeta_n, \zeta_l) = \zeta_n^T \cdot \zeta_l = \begin{cases} 1 & \text{if voxels } n \text{ and } l \text{ are assigned the same tissue;} \\ 0 & \text{otherwise.} \end{cases} \tag{6.12}$$

Therefore the regularization term in the labelling problem is given by

$$\Psi(\zeta) = -\log p(\zeta) = -\sum_{j=1}^J \sum_{n=1}^N \log \lambda_j + \sum_{n=1}^N \sum_{l \in \mathcal{N}_n} \xi_{nl(n)} R(\zeta_n, \zeta_l). \tag{6.13}$$

Ignoring terms which do not depend on ζ , which do not affect the solution, and assuming $\xi_{nl(n)} = \xi \forall n$, the regularization term is simply

$$\Psi(\zeta) = \xi \sum_{n=1}^N \sum_{l \in \mathcal{N}_n} R(\zeta_n, \zeta_l). \tag{6.14}$$

6.2.6 Reconstruction-classification with HMRF: outline

The reconstruction, labelling and classification problems are solved sequentially.

1. Reconstruction:

$$\sigma^{t+1} = \arg \max_{\sigma} p(v | \sigma) p(\sigma | \zeta^t, \theta^t), \tag{6.15}$$

2. Labelling:

$$\zeta^{t+1} = \arg \max_{\zeta} \prod_{n=1}^N \prod_{j=1}^J [p(\sigma_n^{t+1} | \theta_j^t)]^{\zeta_{nj}} p(\zeta_{nj} = 1 | \zeta_{l \in \mathcal{N}_n}). \tag{6.16}$$

3. Classification:

$$\text{E-step: compute } E(\zeta_{nj} | \boldsymbol{\sigma}_n, \theta_j, \boldsymbol{\zeta}_{l \in \mathcal{N}_n}) \quad (6.17)$$

$$\text{M-step: } (\boldsymbol{\theta}^{t+1}, \boldsymbol{\lambda}^{t+1}) = \arg \max_{(\boldsymbol{\theta}, \boldsymbol{\lambda})} p(\boldsymbol{\sigma}^t | \boldsymbol{\theta}, \boldsymbol{\lambda}) p(\boldsymbol{\theta}) p(\boldsymbol{\lambda}). \quad (6.18)$$

In the following, the update rules for the solutions of $\boldsymbol{\sigma}$, $\boldsymbol{\zeta}$, $\boldsymbol{\theta}$ and $\boldsymbol{\lambda}$ are derived. After each update cycle of steps 1-2-3, the process is repeated for a set number of iterations.

6.2.7 Reconstruction

We substitute the Gaussian model for the conductivity (6.7) into the imaging problem (6.15)

$$\boldsymbol{\sigma}^{t+1} = \arg \min_{\boldsymbol{\sigma}} \frac{1}{2} \|A(\boldsymbol{\sigma}) - \mathbf{v}\|_{\boldsymbol{\Sigma}_v^{-1}}^2 + \frac{1}{2} \tau \|\boldsymbol{\sigma} - \bar{\boldsymbol{\sigma}}^t\|_{\boldsymbol{\Sigma}_{\bar{\sigma}}^{-1}}^2, \quad (6.19)$$

where $\boldsymbol{\sigma} \in \mathbb{R}^{N \cdot M}$ accounts for N voxels and M frequencies, $\|\cdot\|$ indicates the Frobenious norm, and $\boldsymbol{\Sigma}_v$ is a weighting matrix. The mean $\bar{\boldsymbol{\sigma}}^t$ and covariance $\boldsymbol{\Sigma}_{\bar{\sigma}}$ of the prior are given by the result of the previous labelling and classification steps: for each element, the mean and covariance of the tissue class corresponding the assigned label $\boldsymbol{\zeta}_n^t$ are taken for all frequencies. The reconstruction problem is solved via damped Gauss-Newton optimization [53], and at each cycle a single update step is performed.

6.2.8 Labelling with graph-cut optimization

Substituting the expression for the regularization (6.14) into the objective function (6.10), the labelling problem becomes

$$\boldsymbol{\zeta}^{t+1} = \arg \min_{\boldsymbol{\zeta}} \sum_{n=1}^N \sum_{j=1}^J \zeta_{nj} \frac{1}{2} (\boldsymbol{\sigma}_n - \mathbf{m}_j^t)^T \boldsymbol{\Sigma}_j^t{}^{-1} (\boldsymbol{\sigma}_n - \mathbf{m}_j^t) + \xi \sum_{n=1}^N \sum_{l \in \mathcal{N}_n} R(\boldsymbol{\zeta}_n, \boldsymbol{\zeta}_l). \quad (6.20)$$

A solution $\boldsymbol{\zeta}$ is sought such that $\zeta_{nj} \in \{0, 1\}$, and $\sum_{j=1}^J \zeta_{nj} = 1$. The objective function (6.20) cannot be minimized via standard optimization techniques because the variable $\boldsymbol{\zeta}$ is discrete, and therefore the function is non-differentiable. Instead, the solution is found using the graph cut method described in section 2.7.3. Open source Matlab and C++ scripts are available that implement the standard graph cut optimization algorithms [63, 12, 11]. The results presented in this chapter were produced using the α -expansion algorithm.

6.2.9 Classification: fitting the HMRF model with EM

It follows the assumptions in section 6.2.3 that the joint probability of $(\boldsymbol{\sigma}, \boldsymbol{\zeta})$ is

$$p(\boldsymbol{\sigma}, \boldsymbol{\zeta}) = p(\boldsymbol{\sigma}|\boldsymbol{\zeta})p(\boldsymbol{\zeta}) = \prod_{n=1}^N p(\boldsymbol{\sigma}_n|\boldsymbol{\zeta}_n)p(\boldsymbol{\zeta}), \quad (6.21)$$

and given the neighbourhood system \mathcal{N}_n

$$p(\boldsymbol{\sigma}_n, \boldsymbol{\zeta}_n|\boldsymbol{\zeta}_{l \in \mathcal{N}_n}) = p(\boldsymbol{\sigma}_n|\boldsymbol{\zeta}_n)p(\boldsymbol{\zeta}_n|\boldsymbol{\zeta}_{l \in \mathcal{N}_n}). \quad (6.22)$$

Thus we have the marginal probability

$$\begin{aligned} p(\boldsymbol{\sigma}_n|\boldsymbol{\zeta}_{l \in \mathcal{N}_n}) &= \int_0^1 p(\boldsymbol{\sigma}_n, \boldsymbol{\zeta}_n|\boldsymbol{\zeta}_{l \in \mathcal{N}_n}) d\zeta \\ &= \sum_{j=1}^J p(\boldsymbol{\sigma}_n, \zeta_{nj} = 1|\boldsymbol{\zeta}_{l \in \mathcal{N}_n}) \\ &= \sum_{j=1}^J p(\boldsymbol{\sigma}_n|\zeta_{nj} = 1)p(\zeta_{nj} = 1|\boldsymbol{\zeta}_{l \in \mathcal{N}_n}). \end{aligned} \quad (6.23)$$

Substituting (6.7) into (6.23) we obtain the probability of the conductivity given the Gaussian HMRF model when the labels are unknown

$$p(\boldsymbol{\sigma}_n|\boldsymbol{\theta}, \boldsymbol{\zeta}_{l \in \mathcal{N}_n}) = \sum_{j=1}^J p(\boldsymbol{\sigma}_n|\theta_j)p(\zeta_{nj} = 1|\boldsymbol{\zeta}_{l \in \mathcal{N}_n}). \quad (6.24)$$

6.2.9.1 E-step

Using Bayes' theorem, the probability that the n th voxel is assigned to the j th tissue is given by

$$p(\zeta_{nj} = 1|\boldsymbol{\sigma}_n, \theta_j, \boldsymbol{\zeta}_{l \in \mathcal{N}_n}) = \frac{p(\boldsymbol{\sigma}_n|\zeta_{nj} = 1, \theta_j)p(\zeta_{nj} = 1|\boldsymbol{\zeta}_{l \in \mathcal{N}_n})}{p(\boldsymbol{\sigma}_n|\boldsymbol{\theta}, \boldsymbol{\zeta}_{l \in \mathcal{N}_n})}. \quad (6.25)$$

Substituting (6.24) then

$$p(\zeta_{nj} = 1|\boldsymbol{\sigma}_n, \theta_j, \boldsymbol{\zeta}_{l \in \mathcal{N}_n}) = \frac{p(\boldsymbol{\sigma}_n|\theta_j)p(\zeta_{nj} = 1|\boldsymbol{\zeta}_{l \in \mathcal{N}_n})}{\sum_{j=1}^J p(\boldsymbol{\sigma}_n|\theta_j)p(\zeta_{nj} = 1|\boldsymbol{\zeta}_{l \in \mathcal{N}_n})}, \quad (6.26)$$

where $p(\boldsymbol{\sigma}_n|\theta_j)$ is given by the Gaussian model (6.7), and $p(\zeta_{nj} = 1|\boldsymbol{\zeta}_{l \in \mathcal{N}_n})$ by the HMRF model (6.11):

$$p(\zeta_{nj} = 1|\boldsymbol{\zeta}_{l \in \mathcal{N}_n}) = \lambda_j^t \prod_{l \in \mathcal{N}_n} \exp\left(-\xi \cdot R(\boldsymbol{\zeta}_n^{t+1}, \boldsymbol{\zeta}_l^{t+1})\right), \quad (6.27)$$

where ζ^{t+1} is the result of the previous labelling step. Finally, the expectation for the labels is

$$\begin{aligned} E(\zeta_{nj}|\boldsymbol{\sigma}_n, \theta_j, \boldsymbol{\zeta}_{l \in \mathcal{N}_n}) &= \int_0^1 \zeta \, p(\zeta_{nj}|\boldsymbol{\sigma}_n, \theta_j, \boldsymbol{\zeta}_{l \in \mathcal{N}_n}) \, d\zeta \\ &= 1 \cdot p(\zeta_{nj} = 1|\boldsymbol{\sigma}_n, \theta_j, \boldsymbol{\zeta}_{l \in \mathcal{N}_n}) + 0 \cdot p(\zeta_{nj} = 0|\boldsymbol{\sigma}_n, \theta_j, \boldsymbol{\zeta}_{l \in \mathcal{N}_n}) \\ &= p(\zeta_{nj} = 1|\boldsymbol{\sigma}_n, \theta_j, \boldsymbol{\zeta}_{l \in \mathcal{N}_n}) \end{aligned} \quad (6.28)$$

$$(6.29)$$

In the following, the notation $E(\zeta_{nj}) = E(\zeta_{nj}|\boldsymbol{\sigma}_n, \theta_j, \boldsymbol{\zeta}_{l \in \mathcal{N}_n})$ is introduced for simplicity.

6.2.9.2 M-step

The update steps for the parameters are found by maximizing the log posterior

$$\begin{aligned} (\boldsymbol{\theta}^{t+1}, \boldsymbol{\lambda}^{t+1}) &= \arg \max_{(\boldsymbol{\theta}, \boldsymbol{\lambda})} \log p(\boldsymbol{\sigma}^t|\boldsymbol{\theta}) + \log p(\boldsymbol{\theta}, \boldsymbol{\lambda}) + \log p(\boldsymbol{\lambda}) \\ &= \arg \max_{(\boldsymbol{\theta}, \boldsymbol{\lambda})} \int_{\zeta} \log p(\boldsymbol{\sigma}^t, \boldsymbol{\zeta}|\boldsymbol{\theta}) \, d\zeta + \log p(\boldsymbol{\theta}) + \log p(\boldsymbol{\lambda}) \\ &= \arg \max_{(\boldsymbol{\theta}, \boldsymbol{\lambda})} \sum_{n=1}^N \sum_{j=1}^J E(\zeta_{nj}) \log p(\sigma_n|\boldsymbol{\theta}) + \log p(\boldsymbol{\theta}) + \log p(\boldsymbol{\lambda}), \end{aligned} \quad (6.30)$$

where we have used

$$\begin{aligned} \int_{\zeta} \log p(\boldsymbol{\sigma}^t, \boldsymbol{\zeta}|\boldsymbol{\theta}) \, d\zeta &= \sum_{n=1}^N \sum_{j=1}^J \int_{\zeta} \log \left[E(\zeta_{nj}) \frac{p(\sigma_n^t, \zeta_{nj}|\boldsymbol{\theta})}{E(\zeta_{nj})} \right] \, d\zeta \\ &\geq \sum_{n=1}^N \sum_{j=1}^J \int_{\zeta} E(\zeta_{nj}) \log \frac{p(\sigma_n^t, \zeta_{nj}|\boldsymbol{\theta})}{E(\zeta_{nj})} \, d\zeta. \end{aligned} \quad (6.31)$$

For non-informative priors on $(\boldsymbol{\theta}, \boldsymbol{\lambda})$ the update rules for the model parameters are obtained:

$$\lambda_j^{t+1} = \frac{\sum_n E(\zeta_{nj})^t}{N}, \quad (6.32)$$

$$\mathbf{m}_j^{t+1} = \frac{\sum_n E(\zeta_{nj})^t \boldsymbol{\sigma}_n}{\sum_n E(\zeta_{nj})^t}, \quad (6.33)$$

$$\boldsymbol{\Sigma}_j^{t+1} = \frac{\sum_n E(\zeta_{nj})^t (\boldsymbol{\sigma}_n - \mathbf{m}_j)(\boldsymbol{\sigma}_n - \mathbf{m}_j)^T + \boldsymbol{\Gamma}_j}{\sum_n E(\zeta_{nj})^t + \nu_j + d + 1}. \quad (6.34)$$

6.3 Results

6.3.1 Numerical validation

The 4-tissue numerical phantom was described in section 3.3.8. The mean of the tissue classes was initialized to the simulated values, and the covariance was set to $\Sigma_j = 10^{-3}\mathbf{I}$ for all four tissues. The parameters of the inverse Wishart distribution were fixed at $\nu_1 = 20000$ and $\Gamma_j = 10^{-2}\mathbf{I}$ for the background, and $\nu_j = 5000$ and $\Gamma_j = 10^{-1}\mathbf{I}$ for the other tissues. These are the same parameters used previously for the reconstruction-classification method, see section 5.3.2. The regularization parameters were $\tau = 10^{-8}$ (conductivity) and $\xi = 5$ (labels). Results obtained after 1 and 6 iterations are displayed (figure 6.2). The images were evaluated by the quantification method set out in section 5.2.9 (figure 6.3).

6.3.2 Robustness to spectral errors

A Gaussian distributed error was added to the tissue conductivity before simulating the boundary voltage data, and the reconstruction was performed using the mean value as the initial guess for the spectral parameters. The reconstruction was repeated 20 times for increasing levels of error: 1%, 2%, 5% and 10%. The parameters of the spectral model and regularization terms were set to the values use in section 6.3.1. The voxel-wise standard deviation of the recovered labels was computed (figure 6.4). The mean percentage of misclassified voxels ($\text{Err}_{\text{class}}$) was 6.16%, 7.13%, 7.65% and 8.23% for increasing levels of error.

6.3.3 Phantom experiment

The phantom and measurement acquisition protocol were described in section 3.3.4. As in the previous chapter, the mean of the spectra was initialized to the sample measurements, and the covariance was set to $\Sigma_j = 10^{-2}\mathbf{I}$ for the background, and $\Sigma_j = 10^{-3}\mathbf{I}$ for the perturbation. The parameters of the inverse Wishart distribution were set to $\nu_1 = 10^6$ and $\Gamma_j = 10^{-1}\mathbf{I}$ for the background, and $\nu_j = 20000$ and $\Gamma_j = 10^{-3}\mathbf{I}$ for perturbation. The regularization parameters were $\tau = 10^{-8}$ and $\xi = 1$ for both positions of the perturbation. The CNR (equation (5.39)) was 9.75 and 8.62 for the positions (−4 cm 0 cm 0 cm) (figure 3.7a) and (0 cm +4 cm 0 cm) (figure 3.7b) respectively. Images were recovered by performing 6 iterations of the proposed method (figure 6.5).

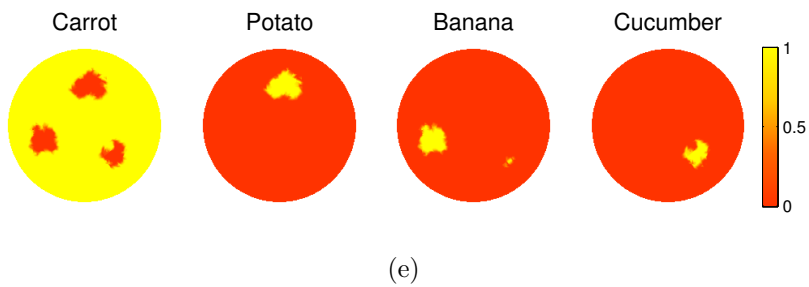
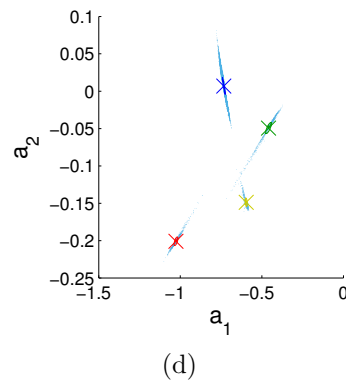
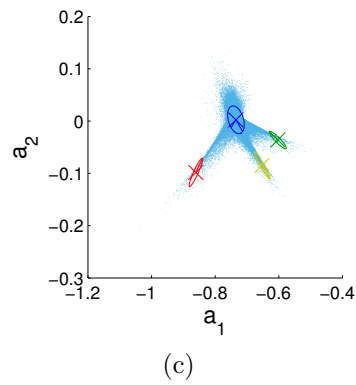
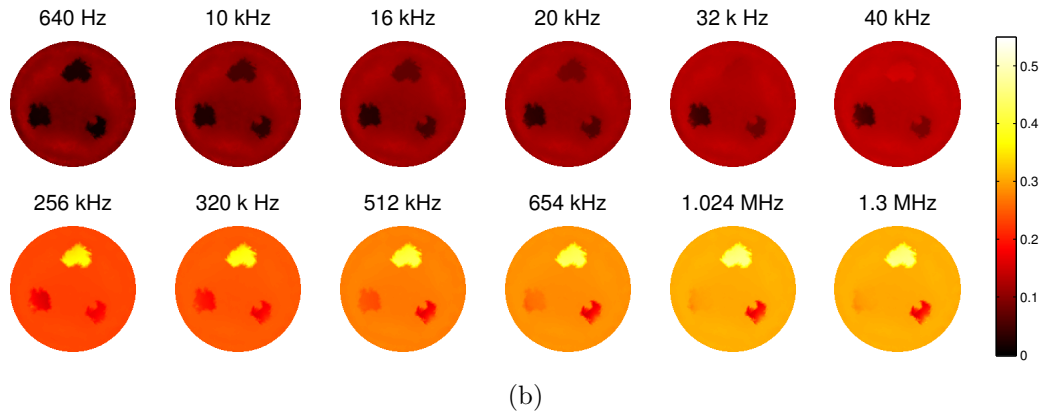
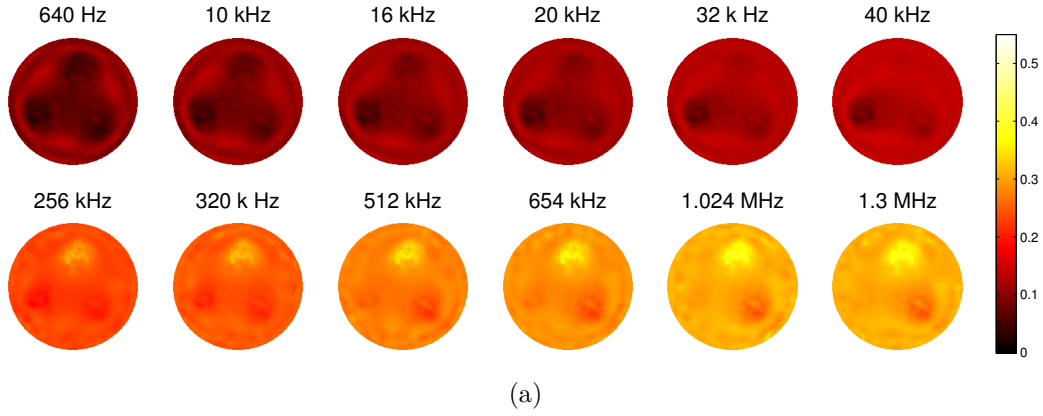


Figure 6.2: Reconstruction-classification with graph cuts, numerical validation: conductivity at (a) iteration 1 and (b) iteration 6 (final) (scale is S/m); scatter plots of the projection onto the primary a_1 and secondary a_2 eigenvectors of the conductivity images at (c) iteration 1 and (d) iteration 6 (the cross indicates the mean, the ellipse the variance, and the colour map is: blue-carrot, red-potato, yellow-banana, green-cucumber); (e) labelling recovered by graph cuts in final iteration.

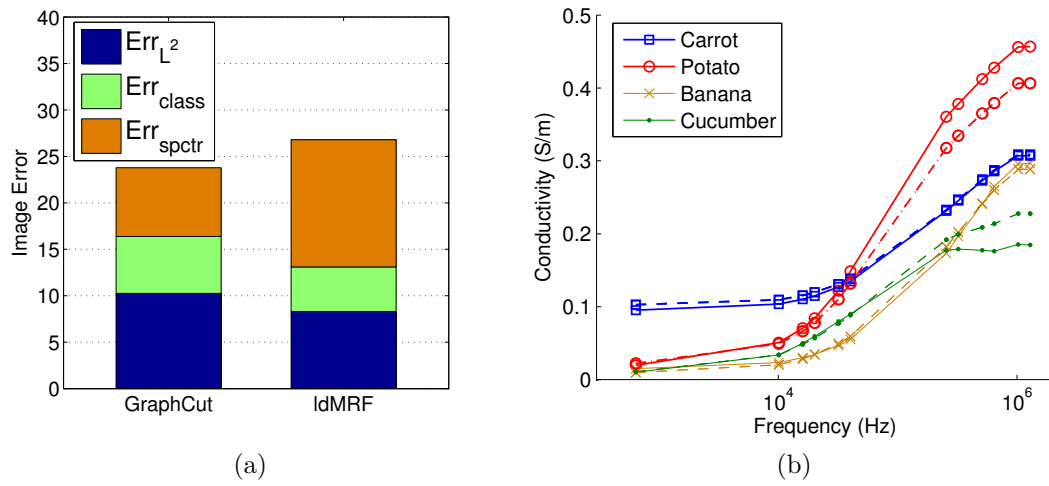


Figure 6.3: Reconstruction-classification with graph cuts, numerical validation: (a) comparison between image quantification results obtained using graph cuts and label-dependent MRF (section 5.3.5 and figure 5.8) (b) mean conductivity spectra m recovered by the final classification step (solid lines), and real spectra (dashed lines).

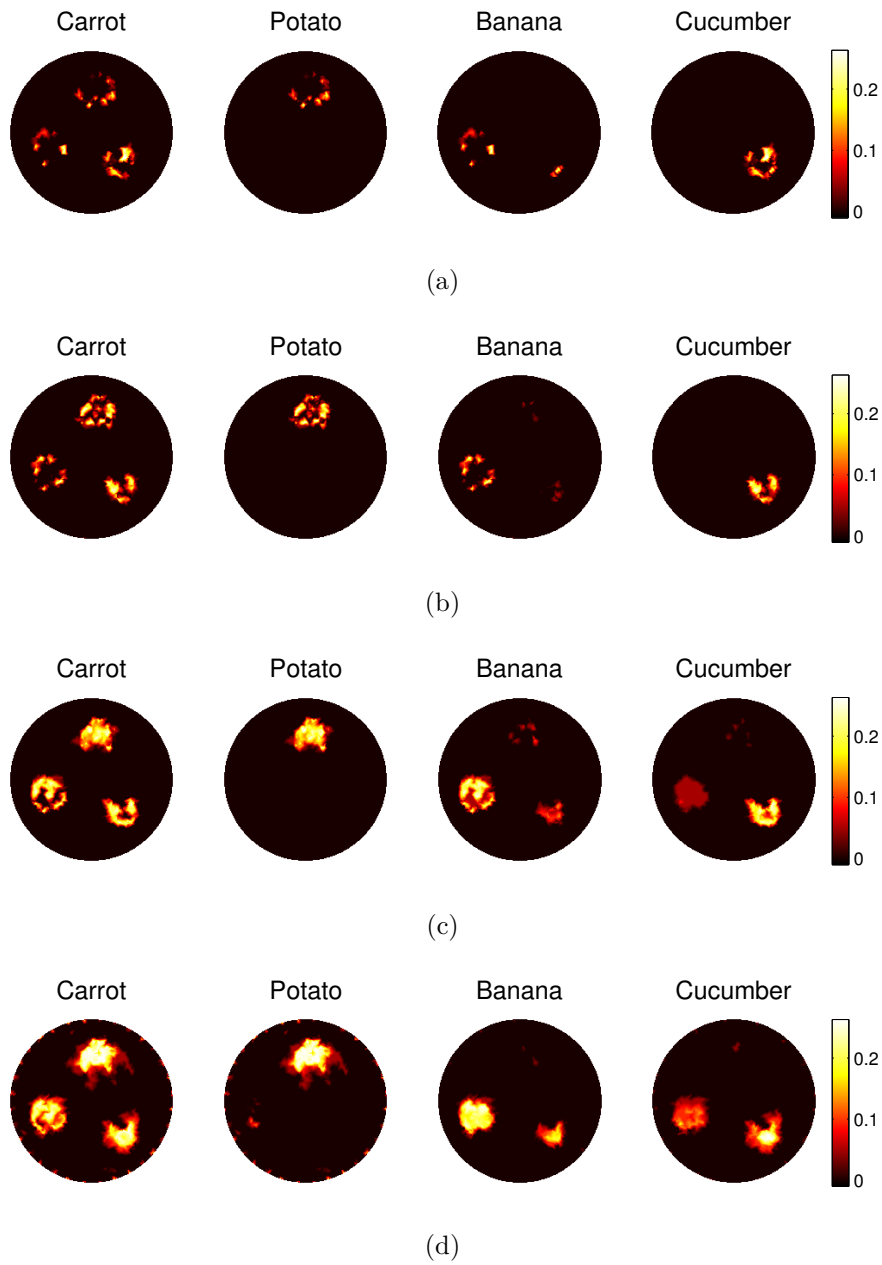
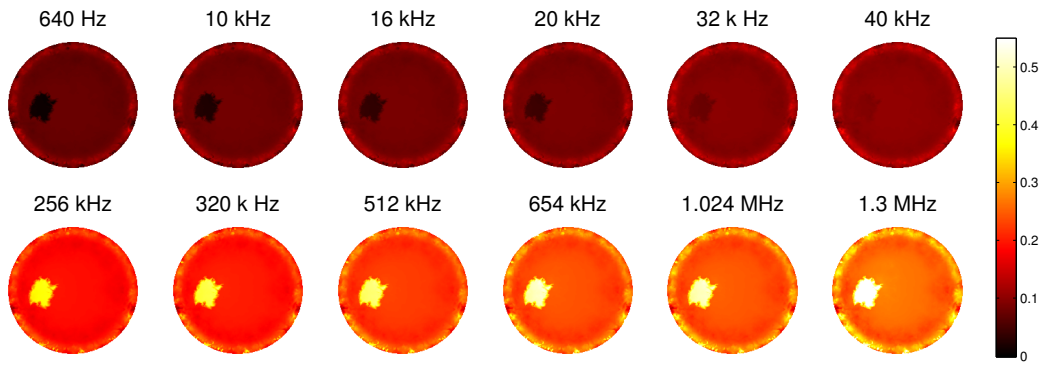
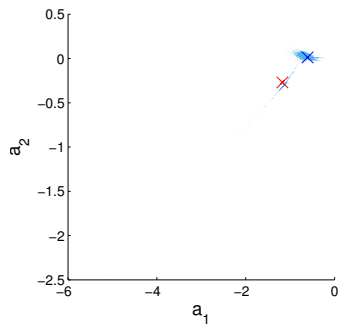


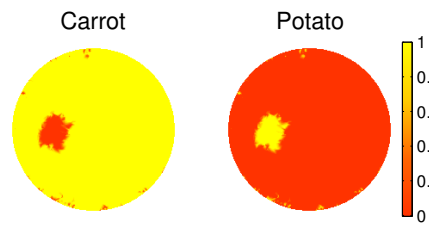
Figure 6.4: Robustness to errors in the initial guess of the tissue spectra: images of variance over 20 trials of the labels obtained after adding errors to the tissue spectra with variance 1% (a), 5% (b), 10% (c) and 20%(d).



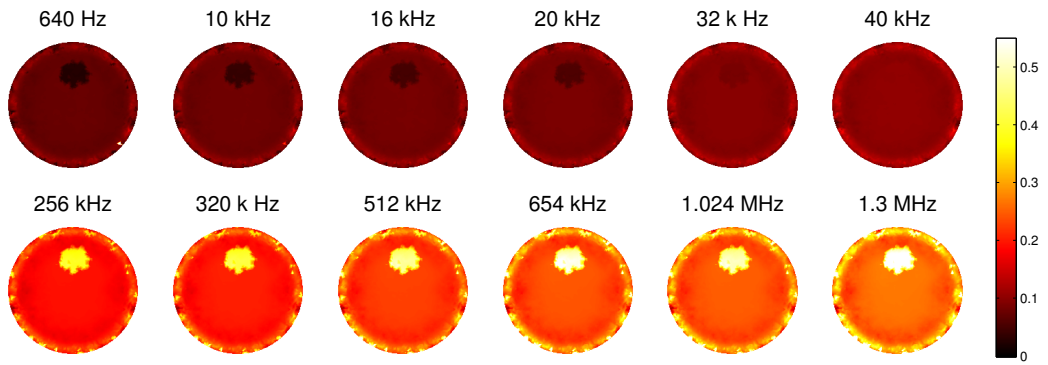
(a)



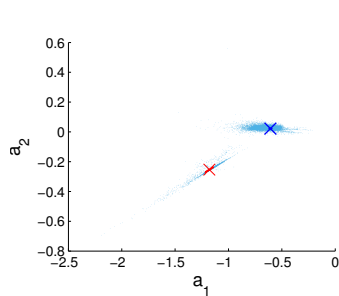
(b)



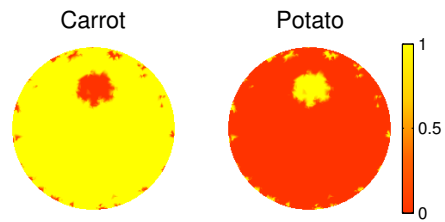
(c)



(d)



(e)



(f)

Figure 6.5: Phantom experiment images obtained by reconstruction-classification with graph cuts: conductivity image (scale is S/m), scatter plot and labels image for (a)–(c) position $(-4\text{ cm } 0\text{ cm } 0\text{ cm})$ and (d)–(f) position $(0\text{ cm } +4\text{ cm } 0\text{ cm})$.

6.4 Discussion

6.4.1 Methodology

The main difference between the reconstruction-classification methods presented in this and previous chapters is the approach to spatial smoothing. It has already been shown that without the introduction of a spatial prior, and the sole consideration of a spectral prior in the conductivity reconstruction, poor image quality is achieved (section 5.3.4). In the previous chapter, imaging errors were reduced by applying Markov random field regularization in the reconstruction step (section 5.3.1), and further improvements were achieved by using the labelling result to qualify the spatial prior (section 5.3.5). The method set out in this chapter enables the placement of a spatial prior on the labels, rather than the conductivity. This allows for a more intuitive interpretation of the spatial prior, and a closer correspondence between the model and the real object. Our expectation, which is the prior information encoded by the spatial model, is that neighbouring voxels are more likely to be occupied by the same tissue. Given that a statistical model for tissue spectra is assumed, it does not immediately follow that neighbouring voxels are more likely to take the same conductivity value. Therefore it is more appropriate to consider a spatial prior on the labels, rather than on the conductivity image. Furthermore, whereas justification of the labelling prior in the Bayesian framework is easily achieved, justification of the conductivity prior would require a proof of independence of the spatial and spectral priors (so that the two terms are additive in the objective function), which is non trivial.

6.4.2 Numerical validation

The imaging results achieved with graph cuts are similar to those obtained previously, however the image quantification measures reflect some important differences (figure 6.3a). From the comparison with label-dependant MRF (the best example amongst the results obtained by applying the spatial prior to the conductivity) it is evident that recovery of the conductivity and labels, reflected by the errors Err_{L_2} and $\text{Err}_{\text{class}}$ respectively, is poorer in the graph cuts case. This is expected, as it is more likely that direct application of the spatial prior will yield smoother conductivity images. However, estimation of the conductivity spectra of the tissues is greatly improved, as evident from the lower value of $\text{Err}_{\text{spectr}}$ and the accordance between the simulated and recovered spectral curves in figure 6.3b. This is due to the inclusion of spatial smoothness information in the classification step, specifically in the calculation of the E-step from of

the labelling result. The spectral curves are well matched for the low frequencies and for the potato and carrot tissues, but the agreement drops off at the higher frequencies for the potato and cucumber. It is likely that the error caused in the estimation of the spectra by misclassified elements is highest in these cases because the spread of the conductivity is larger, and the values are further from those of the background.

6.4.3 Robustness to spectral errors

The purpose of the robustness study was to evaluate the capability of the method to correct for errors in the initial spectral model. From comparison with the results obtained in the previous chapter (section 5.3.3), the images show that reconstruction-classification with graph cut optimization is less successful in recovering the labels (figure 6.4). For an error with variance 5% or lower, the misclassified electrodes are limited to the boundary between tissues, but for 10% or higher the perturbations may not be identified correctly.

6.4.4 Phantom experiment

The technique developed in this chapter was successful in recovering the position of a perturbation placed in an experimental phantom. As in the case of reconstruction-classification using absolute data (section 5.3.9, figure 5.10) the images present artefacts around the edge of the tank caused by incongruities in the boundary geometry of the model (figure 6.5). As discussed in chapter 5, these artefacts could be reduced by modifying the method to allow for the use of frequency-difference data, at the cost of losing image contrast and the capability to recover the absolute conductivity spectra (section 5.4.5).

6.5 Conclusion

In this chapter, a method for performing combined reconstruction-classification using graph cut optimization was formalized in the Bayesian framework. Whereas the reconstruction step was relatively unchanged with respect to the algorithm presented in chapter 5, substantial modifications to the classification step were required to model a neighbourhood system on the labels. Previously, the E-step of the expectation-maximization algorithm involved the calculation of the responsibility, i.e. the probability that the j th tissue had contributed to the conductivity of the n th voxel (equation (5.17)). Then the labels were simply taken to be the MAP of the responsibility. With the inclusion of a spatial prior on the labels (equation (6.11)), calculation of the responsibility is mathematically intractable if the labels are unknown (equation (6.26)). For this reason, it becomes necessary to estimate the labels before performing the classification step. This

was achieved by introducing a Hidden Markov Random Field model for the dependence of the conductivity on the labels, and solving the resulting labelling problem via graph cut optimization.

The method was validated by application to a numerical example, and it was demonstrated that this approach results in better recovery of the tissue spectra. The method was also shown to be robust to small errors in the initial guess of the spectral model, and images were successfully recovered from phantom data.

Future work should focus on increasing the automation of the method. Given the added complication of the labelling and classification process, the reconstruction-classification method required the selection of numerous model and regularization parameters. In this chapter, the parameters of the spectral model were left unchanged with respect to the previous chapter in order to adequately compare the results. Further consideration is needed to find the optimal balance between the choice of parameters for the HMRF model and the inverse Wishardt distribution. Furthermore, the method could be modified to allow for the deduction of the algorithm parameters from the result of the first reconstruction step, without external intervention by the user. In this chapter, a homogenous spatial prior was used in the segmentation process. Anatomical information derived from a supplementary imaging modality or statistical atlas of the region-of-interest could be employed to produce a patient-specific spatial prior. This could significantly improve the quality of the resulting images.

Chapter 7

Conclusion

The focus of this dissertation is on novel image reconstruction techniques for performing EIT using multifrequency data. The use of prior spectral information has been investigated as a means to overcome the limitations inherent in the standard frequency-difference and absolute imaging approaches to static EIT imaging. The overall purpose was to propose image reconstruction algorithms with sufficient flexibility and robustness to be applied to experimental problems in a clinical setting, and place within reach the ultimate goal of diagnostic EIT imaging. In particular, the application of EIT to early stroke type differentiation was of primary interest. In this chapter, the findings presented in this dissertation are summarized, the conclusions and limitations to this work are discussed, and future research directions are set out.

7.1 Summary of findings

In chapter 3, a method was proposed for introducing explicit spectral constraints in a nonlinear multifrequency reconstruction technique for EIT. A fraction model was defined, whereby the conductivity is expressed as a linear combination of the conductivities of individual tissues present in the domain. This approach allowed for the simultaneous use of all data in a direct multifrequency method, which resulted in a reduction of the degrees of freedom of the imaging problem, and was shown to be superior to an indirect method. The devised *fraction reconstruction* technique was validated on two-tissue and four-tissue numerical examples, and robustness to small errors in the assumed tissue spectra was demonstrated. The performance of the algorithm was shown to be superior to pre-existing static methods, absolute and weighted frequency-difference (WFD) imaging, in the case of resolving an anomaly in a tank phantom and a numerical example violating the assumptions of WFD. Finally, it was shown empirically that the approximation error introduced by the fraction model is small.

In chapter 4, the results of application of the fraction reconstruction method to a realistic numerical head phantom were presented. Images of ischaemic and haemorrhagic stroke in a human head model including a resistive skull were produced for the first time. The robustness of the method to typical sources of modelling errors was investigated, and it was found that the method is robust to errors in the contact impedance, moderately sensitive to errors in the tissue spectra, and highly sensitive to errors in the electrode positions. Whereas the sensitivity to spectral errors was addressed in chapters 5 and 6, this work highlights the importance of obtaining accurate estimates of the electrode positions in 3D. This can be achieved either by inserting the electrodes in a rigid helmet with known geometry, or by acquiring the location of the electrodes for each experimental setup. Alternatively, it may be possible to consider the electrode positions as unknowns in the image reconstruction process, and recover these simultaneously to the conductivity.

In chapter 5, a method was proposed for simultaneously reconstructing conductivity images using spectral information, and estimating the parameters of a statistical spectral model. A Gaussian mixture model was introduced for the conductivity, and an expectation-maximization (EM) algorithm was devised to update the mean and variance of the tissue spectra after each reconstruction step. It was shown that this combined *reconstruction-classification* technique is highly robust to errors in the initial guess of the tissue conductivities. Different approaches to spatial smoothing in the reconstruction step were investigated; the best results were obtained by penalizing differences in conductivity across voxels assigned to the same tissue in the previous classification step. Two variants of the reconstruction-classification method were formulated, using absolute and frequency-difference data, and the performance was compared on phantom data; it was found that while using difference data reduced the edge artefacts caused by modelling errors, the contrast between the perturbation and the background was affected.

In chapter 6, an alternative approach to solving the reconstruction-classification problem was proposed, which allowed for the inclusion of a spatial prior on the labels. The problems of reconstructing multifrequency conductivity images, segmenting the images per tissue type, and updating the spectral model, were tackled simultaneously in an iterative scheme. The labelling step was performed by a graph cut optimization method, which allowed for the use of a hidden Markov random field model. The result of the labelling step was used to update the parameters of the tissue classes by an EM algorithm. It was shown empirically that this approach results in improved recovery of the tissue spectra, but is less robust to spectral modelling errors than the method

proposed in the previous chapter.

7.2 Limitations and future work

7.2.1 Conductivity modelling

The main idea developed in this thesis is the exploitation of prior knowledge about the spectral properties of tissues to improve the ill-posedness of the inverse problem of EIT. Methods for including both exact and statistical models of the conductivity have been proposed.

The fraction reconstruction method discussed in chapter 3 assumes perfect knowledge of the spectra of tissues in the domain (section 3.2.1). Although robustness to a small amount of uncertainty was demonstrated (section 3.3.3), significant errors in the estimation of the spectral model can severely deteriorate image quality. Knowledge of the tissue conductivities is bound to be uncertain: the gold standard is sample measurements acquired with an impedance spectroscoper, which are unavoidably affected by instrumentation noise. This approach proved successful in the phantom study presented in chapter 3 (section 3.3.4), where it was possible to take tissue samples out of the tank and acquire spectral measurements. However, a different approach is needed for clinical applications, for example the use of conductivity values found in the literature, or the collection of a library of tissue spectra by a preclinical study. Furthermore, variations in composition, temperature, flow rate and cell count of biological tissues will cause variations in the conductivity which are difficult to model and account for. With regard to stroke imaging, the dynamic nature of ischaemia and haemorrhage will cause the conductive properties of tissues in the head to vary in time. Therefore accurate modelling of the tissue spectra may require knowledge of the length of time passed since the onset of the stroke.

The combined reconstruction-classification method presented in chapter 5 was designed to overcome the limitations of the fraction reconstruction method in terms of robustness to spectral errors. The introduction of a Gaussian mixture model allowed for the tissue conductivities to assume a non-zero variance, and also provided a framework for updating the model (section 5.2.1); after each reconstruction step, the conductivity image is subject to a soft-classification procedure, and the spectral properties are derived. It was shown that this approach resulted in a highly robust method with regards to errors in the initial guess of the tissue spectra (section 5.3.3). Although the classification step is very fast and the cost in terms of computation time is minimum, a disadvantage

to the inclusion of a statistical model is the increase in the number of parameters which require "tuning" by the user. A process whereby the spectral parameters are initialized automatically after the first reconstruction step by some pattern recognition technique would provide a valuable addition to the method. In this study the algorithm was applied exclusively to problems involving a known number of tissues; further development could allow for the estimation of the number of classes, or the addition of a class with large initial variance to include anything "other" than a small number of tissues of interest. A technical issue introduced by the use of a spectral model is the need to combine the model with a spatial prior. The label-dependent MRF idea tested in chapter 5 provided an empirical solution, in that application to a numerical example returned high quality images (section 5.3.5). However, the issue remains of justifying the method in the Bayesian sense and providing an elegant mathematical formulation.

In chapter 6, an attempt was made to include a spatial prior on the labels rather than the conductivity, thus removing the problem of treating the spectral and spatial models simultaneously. The conductivity model is given only by the statistical spectral prior, which in the Bayesian framework delivers a single regularization term in the reconstruction problem. In order to avoid calculating the mixed probability term in the E-step of the classification problem, the labels were first estimated by graph cut optimization. Although this method provided a more accurate recovery of the tissue spectra, the other measures of image quality and the robustness to spectral errors were compromised. Further analysis is required to determine the optimal choice of parameters for the spectral and spatial priors.

7.2.2 Boundary modelling errors

Sensitivity to modelling errors in static EIT imaging is one of the greatest challenges faced by the research community, and is currently an unresolved issue. In chapter 3, the effect of modelling errors on fraction imaging of ischaemic and haemorrhagic stroke in a realistic 3D human head model was investigated. It was found that errors in the modelling of the electrode positions constitute a major, if not the primary, obstacle to clinical application of the method. Even small errors have the effect of severely deteriorating image quality, and the position of the electrodes must be measured to sub-millimetric precision. In order to accurately represent the shape and size of the electrodes, high resolution meshes and refinement at the boundary are also necessary. This can significantly affect the run time and memory use of the imaging algorithm.

It has recently been proposed in the literature to include the position and shape of

the electrodes as unknowns in the imaging problem, so that the electrode locations can be estimated simultaneously to the conductivity. The idea is that the boundary voltage data contains information both about the internal conductivity distribution and the boundary shape of the object, and that image artefacts can be avoided by recovering these together. A method for reconstructing the boundary following a deformation was developed in [14] for a 2D model with point electrodes, and using a linear time-difference approach. The *approximation error method* [60], which allows for the correction of errors with known statistics, was adapted to account for inaccuracies in the geometry in [80]. An analytical approach to the absolute imaging problem was recently formalized and applied to 2D problems using the complete electrode model by Dardé *et al.* [29, 30]. Extension of this method to fully three-dimensional problems is relatively straightforward and would constitute a significant breakthrough.

7.2.3 Algorithm speed

Application of EIT imaging to complex geometries, such as a human head, requires the use of very high resolution meshes to ensure convergence of the forward problem. The size of the elements must be small enough to represent detailed features and minimize discretization errors. In particular, mesh refinement at the electrodes is crucial to reducing artefacts caused by mismatched electrode sizes and locations. For large scale meshes, the speed and memory efficiency of the image reconstruction algorithm are critical. With regards to solving the forward problem, significant advances were recently made by Jehl *et al.* [57] in developing a parallel solver. However, an iterative nonlinear inversion scheme involves solving the forward problem, calculating the Jacobian, and computing the update step several times, which is computationally very labour intensive. There is scope for optimizing the imaging methods presented in this thesis to minimize run time and memory usage. For example, by introducing a suitable preconditioner to improve the solve time of the Gauss-Newton search direction, or applying a memory efficient inversion method such as limited-memory BFGS [81]. Integration with the approximation error method could also allow for the use of lower-resolution meshes without loss of image quality [60, 79].

Bibliography

- [1] J. F. P. J. Abascal, W. R. B. Lionheart, S. R. Arridge, M. Schweiger, D. Atkinson, and D. S. Holder. Electrical impedance tomography in anisotropic media with known eigenvectors. *Inverse Problems*, 27(6):065004, June 2011.
- [2] A. Adler, P. O. Gaggero, and Y. Maimaitijiang. Adjacent stimulation and measurement patterns considered harmful. *Physiological measurement*, 32(7):731–44, July 2011.
- [3] S. Ahn, T. I. Oh, S. C. Jun, J. K. Seo, and E. J. Woo. Validation of weighted frequency-difference EIT using a three-dimensional hemisphere model and phantom. *Physiological measurement*, 32(10):1663–80, Oct. 2011.
- [4] K. Astala, J. Mueller, and L. Päiväranta. Direct electrical impedance tomography for nonsmooth conductivities. *Inverse Problems*, pages 1–24, 2011.
- [5] A. P. Bagshaw, A. D. Liston, R. H. Bayford, A. Tizzard, A. P. Gibson, a. T. Tidswell, M. K. Sparkes, H. Dehghani, C. D. Binnie, and D. S. Holder. Electrical impedance tomography of human brain function using reconstruction algorithms based on the finite element method. *NeuroImage*, 20(2):752–64, Oct. 2003.
- [6] D. C. Barber and a. D. Seagar. Fast reconstruction of resistance images. *Clinical physics and physiological measurement*, 8 Suppl A:47–54, Jan. 1987.
- [7] R. H. Bayford, a. Gibson, a. Tizzard, T. Tidswell, and D. S. Holder. Solving the forward problem in electrical impedance tomography for the human head using IDEAS (integrated design engineering analysis software), a finite element modelling tool. *Physiological measurement*, 22(1):55–64, Feb. 2001.
- [8] L. Borcea. Electrical impedance tomography. *Inverse Problems*, 18, 2002.
- [9] A. Borsic, B. M. Graham, A. Adler, and W. R. B. Lionheart. In vivo impedance imaging with total variation regularization. *IEEE transactions on medical imaging*, 29(1):44–54, Jan. 2010.

- [10] C. Boumann and K. Sauer. A generalized gaussian image model for edge-preserving MAP estimation. *IEEE transactions on image processing*, 2, 1993.
- [11] Y. Boykov and V. Kolmogorov. An experimental comparison of min-cut/max-flow algorithms for energy minimization in vision. *IEEE transactions on pattern analysis and machine intelligence*, 26(9):1124–37, Sept. 2004.
- [12] Y. Boykov, O. Veksler, and R. Zabih. Fast approximate energy minimization via graph cuts. *IEEE Transactions on Pattern Analysis and Machine Intelligence*, 23(11):1222–1239, 2001.
- [13] A. Boyle and A. Adler. The impact of electrode area, contact impedance and boundary shape on EIT images. *Physiological measurement*, 32(7):745–54, July 2011.
- [14] A. Boyle, A. Adler, and W. R. B. Lionheart. Shape deformation in two-dimensional electrical impedance tomography. *IEEE transactions on medical imaging*, 31(12):2185–93, Dec. 2012.
- [15] R. P. Brent. *Algorithms for minimization without derivatives*. Prentice-Hall, Englewood Cliffs, New Jersey, 1973.
- [16] B. Brown, D. Barber, W. Wang, L. Lu, A. Leathard, R. Smallwood, A. Hampshire, R. Mackay, and K. Hatzigalanis. Multi-frequency imaging and modelling of respiratory related electrical impedance changes. *Physiological measurement*, 15(A1), 1994.
- [17] B. Brown and A. Seagar. The Sheffield data collection system. *Clinical Physics and Physiological Measurement*, 91, 1987.
- [18] B. H. Brown, A. D. Leathard, L. Lu, W. Wang, and A. Hampshire. Measured and expected Cole parameters from electrical impedance tomographic spectroscopy images of the human thorax. *Physiological measurement*, 16(3A):A57–67, Aug. 1995.
- [19] A. Brownell, D. Isaacson, G. Saulnier, and J. Newell. Full Maxwell Equations as a forward model for EIT in the mammography geometry. In *Bioengineering Conference (NEBEC), 2011 IEEE 37th Annual Northeast*, number 1, 2011.

- [20] M. Brühl. Explicit characterization of inclusions in electrical impedance tomography. *SIAM Journal on Mathematical Analysis*, 32(6):1327–1341, 2001.
- [21] M. Brühl and M. Hanke. Numerical implementation of two noniterative methods for locating inclusions by impedance tomography. *Inverse Problems*, 1029, 2000.
- [22] A. P. Calderon. On an inverse boundary value problem. *Comp. Appl. Math*, 25(2-3):133– 138, 2006.
- [23] M. Cheney. Inverse boundary-value problems. *American Scientist*, 85:448–455, 1997.
- [24] CIBC. Seg3d: Volumetric image segmentation and visualization. scientific computing and imaging institute (sci), 2014.
- [25] K. S. Cole and R. H. Cole. Dispersion and Absorption in Dielectrics I . Alternating Current Characteristics. *Current*, 341, 1941.
- [26] R. D. Cook, G. Saulnier, D. G. Gisser, J. C. Goble, J. C. Newell, and D. Isaacson. ACT3: a high-speed, high-precision electrical impedance tomograph. *IEEE transactions on bio-medical engineering*, 41(8):713–22, Aug. 1994.
- [27] A. Corlu, R. Choe, T. Durduran, K. Lee, M. Schweiger, S. Arridge, E. M. C. Hillman, and A. G. Yodh. Diffuse optical tomography with spectral constraints and wavelength optimization. *Applied optics*, 44(11):2082–93, Apr. 2005.
- [28] H. Cornean, K. Knudsen, and S. Siltanen. Towards a d-bar reconstruction method for three-dimensional EIT. *Journal of Inverse and Ill-Posed Problems*, 14(2):111–134, Apr. 2006.
- [29] J. Dardé and N. Hyvönen. Simultaneous reconstruction of outer boundary shape and admittivity distribution in electrical impedance tomography. *SIAM Journal on Imaging Sciences*, 6(1):176–198, 2013.
- [30] J. Dardé, N. Hyvönen, A. Seppänen, and S. Staboulis. Simultaneous recovery of admittivity and body shape in electrical impedance tomography: an experimental evaluation. *Inverse Problems*, 29(8):085004, Aug. 2013.
- [31] J. C. de Munck, T. J. Faes, and R. M. Heethaar. The boundary element method in the forward and inverse problem of electrical impedance tomography. *IEEE transactions on bio-medical engineering*, 47(6):792–800, June 2000.

- [32] A. Dedner, R. Klöfkorn, M. Nolte, and M. Ohlberger. A generic interface for parallel and adaptive discretization schemes: abstraction principles and the dune-fem module. *Computing*, 90(3-4):165–196, 2010.
- [33] J. F. Edd, L. Horowitz, and B. Rubinsky. Temperature dependence of tissue impedivity in electrical impedance tomography of cryosurgery. *IEEE transactions on bio-medical engineering*, 52(4):695–701, Apr. 2005.
- [34] B. M. Eyuboglu, B. H. Brown, and D. C. Barber. In vivo imaging of cardiac related impedance changes. *IEEE Engineering in Medicine and Biology magazine*, 8(1):39–45, Jan. 1989.
- [35] L. Fabrizi, a. McEwan, T. Oh, E. J. Woo, and D. S. Holder. An electrode addressing protocol for imaging brain function with electrical impedance tomography using a 16-channel semi-parallel system. *Physiological measurement*, 30(6):S85–101, June 2009.
- [36] Q. Fang, P. Meaney, and K. Paulsen. Microwave image reconstruction of tissue property dispersion characteristics utilizing multiple-frequency information. *IEEE Transactions on Microwave Theory and Techniques*, 52(8):1866–1875, Aug 2004.
- [37] C. Gabriel, S. Gabriel, and E. Corthout. The dielectric properties of biological tissues: I. Literature survey. *Physics in medicine and biology*, 41(11):2231–49, Nov. 1996.
- [38] C. Gabriel, a. Peyman, and E. H. Grant. Electrical conductivity of tissue at frequencies below 1 MHz. *Physics in medicine and biology*, 54(16):4863–78, Aug. 2009.
- [39] M. Gee, C. Siefert, J. Hu, R. Tuminaro, and M. Sala. ML 5.0 smoothed aggregation user’s guide. Technical Report SAND2006-2649, Sandia National Laboratories, 2006.
- [40] G. H. Golub and C. F. V. Loan. *Matrix Computations*. The Johns Hopkins University Press, 3rd edition, 1996.
- [41] A. R. Hampshire, R. H. Smallwood, B. H. Brown, and R. A. Primhak. Multifrequency and parametric EIT images of neonatal lungs. *Physiological measurement*, 16(3A):A175–89, Aug. 1995.

- [42] C. Hansen and D. P. O’Leary. The use of the L-curve in the regularization of discrete ill-posed problems. *SIAM Journal on Scientific Computing*, 14(6):1487–1503, 1993.
- [43] P. Hansen. *The L-curve and its use in the numerical treatment of inverse problems*, volume 2. 1999.
- [44] P. Hansen, T. Sekii, and H. Shibahashi. The modified truncated SVD method for regularization in general form. *SIAM Journal on Scientific and Statistical Computing*, 13(5):1142–1150, 1992.
- [45] P. Hiltunen, S. J. D. Prince, and S. Arridge. A combined reconstruction-classification method for diffuse optical tomography. *Physics in medicine and biology*, 54(21):6457–76, Nov. 2009.
- [46] D. Holder. Brief introduction to bioimpedance. In *Electrical Impedance Tomography*, chapter Appendix A, pages 411–422. 2004.
- [47] D. Holder, A. Rao, and Y. Hanquan. Imaging of physiologically evoked responses by electrical impedance tomography with cortical electrodes in the anaesthetized rabbit. *Physiological measurement*, 179, 1999.
- [48] D. Holder and T. Tidswell. Electrical impedance tomography of brain function. In *Electrical Impedance Tomography*, chapter 4, pages 127–166. 2004.
- [49] D. S. Holder and a. Khan. Use of polyacrylamide gels in a saline-filled tank to determine the linearity of the Sheffield Mark 1 electrical impedance tomography (EIT) system in measuring impedance disturbances. *Physiological measurement*, 15 Suppl 2:A45–50, May 1994.
- [50] L. Horesh. Some novel approaches in modelling and image reconstruction for multi-frequency electrical impedance tomography of the human brain. *PhD thesis*, 2006.
- [51] L. Horesh, R. H. Bayford, R. J. Yerworth, A. Tizzard, G. M. Ahadzi, and D. S. Holder. Beyond the linear domain-The way forward in MFEIT image reconstruction of the human head. In *IFMBE Proceedings, vol. 11*, volume 3, pages 683–686, Gdansk, Poland, 2004. Gdansk University of Technology.
- [52] L. Horesh, O. Gilad, A. Romsauerova, A. McEwan, S. Arridge, and D. Holder. Stroke type differentiation by multi-frequency electrical impedance tomography -

- a feasibility study. In *3rd Eur Med Biol Eng Conf*, volume 11, pages 1252–1256, Prague, Czech Republic, 2005.
- [53] L. Horesh, M. Schweiger, S. Arridge, and D. Holder. Large-scale non-linear 3D reconstruction algorithms for electrical impedance tomography of the human head. *IFMBE Proceedings*, vol. 14, 14:3862–3865, 2007.
- [54] N. Hyvönen. Application of the factorization method to the characterization of weak inclusions in electrical impedance tomography. *Advances in Applied Mathematics*, 2007.
- [55] D. Isaacson. Distinguishability of conductivities by electric current computed tomography. *IEEE transactions on medical imaging*, 5(2):91–5, Jan. 1986.
- [56] D. Isaacson, J. L. Mueller, J. C. Newell, and S. Siltanen. Imaging cardiac activity by the D-bar method for electrical impedance tomography. *Physiological measurement*, 27(5):S43–50, May 2006.
- [57] M. Jehl, A. Dedner, T. Betcke, K. Aristovich, R. Kloforn, and D. Holder. A Fast Parallel Solver for the Forward Problem in Electrical Impedance Tomography. *IEEE transactions on bio-medical engineering*, 9294(c):1–13, July 2014.
- [58] S. C. Jun, J. Kuen, J. Lee, E. J. Woo, D. Holder, and J. K. Seo. Frequency-difference electrical impedance tomography (fdEIT): validation by simulation and tank experiment. *Physiological measurement*, 30(10):1087–99, Oct. 2009.
- [59] J. Kaipio and V. Kolehmainen. Statistical inversion and Monte Carlo sampling methods in electrical impedance tomography. *Inverse Problems*, 1487, 2000.
- [60] J. Kaipio and E. Somersalo. *Statistical and computational inverse problems*. 2005.
- [61] R. Kohn and M. Vogelius. Determining conductivity by boundary measurements II. Interior results. *Communications on Pure and Applied Mathematics*, XXXVIII(1985):643–667, 2006.
- [62] V. Kolehmainen, M. Vauhkonen, P. Karjalainen, and J. Kaipio. Assessment of errors in static electrical impedance tomography with adjacent and trigonometric current patterns. *Physiological measurement*, 18(4):289, 1997.

- [63] V. Kolmogorov and R. Zabih. What energy functions can be minimized via graph cuts? *IEEE transactions on pattern analysis and machine intelligence*, 26(2):147–59, Feb. 2004.
- [64] J. Latikka, T. Kuurne, and H. Eskola. Conductivity of living intracranial tissues. *Physics in medicine and biology*, 46(6):1611–6, June 2001.
- [65] A. Lechleiter, N. Hyvönen, and H. Hakula. The factorization method applied to the complete electrode model of impedance tomography. *SIAM Journal on Applied Mathematics*, 68(4):1097–1121, 2008.
- [66] W. Lionheart. EIT reconstruction algorithms: pitfalls, challenges and recent developments. *Physiological Measurement*, 25(1):125–142, Feb. 2004.
- [67] W. Lionheart, N. Polydorides, and A. Borsic. The reconstruction problem. In *Electrical Impedance Tomography*, chapter 1, pages 3–64. 2004.
- [68] a. D. Liston, R. H. Bayford, and D. S. Holder. The effect of layers in imaging brain function using electrical impedance tomography. *Physiological Measurement*, 25(1):143–158, Feb. 2004.
- [69] A. Malich, T. Böhm, M. Facius, I. Kleinteich, M. Fleck, D. Sauner, R. Anderson, and W. Kaiser. Electrical impedance scanning as a new imaging modality in breast cancer detection - a short review of clinical value on breast application, limitations and perspectives. *Nuclear Instruments and Methods in Physics Research*, 497(1):75–81, Jan. 2003.
- [70] Y. Mangnall, A. Baxter, and R. Avill. Applied potential tomography: a new non-invasive technique for assessing gastric function. *Clinical Physics and Physiological Measurement*, 119, 2001.
- [71] A. McEwan, G. Cusick, and D. S. Holder. A review of errors in multi-frequency EIT instrumentation. *Physiological measurement*, 28(7):S197–215, July 2007.
- [72] A. McEwan, A. Romsauerova, R. Yerworth, L. Horesh, R. Bayford, and D. S. Holder. Design and calibration of a compact multi-frequency EIT system for acute stroke imaging. *Physiological measurement*, 27(5):S199–210, May 2006.
- [73] K. Miller. Least squares methods for ill-posed problems with a prescribed bound. *SIAM Journal on Mathematical Analysis*, 1(1):52–75, 1970.

- [74] J. Mueller, D. Isaacson, and J. Newell. Reconstruction of conductivity changes due to ventilation and perfusion from EIT data collected on a rectangular electrode array. *Physiological measurement*, 97, 2001.
- [75] A. Nachman. Reconstructions from boundary measurements. *The Annals of Mathematics*, 128(3):531–576, 1988.
- [76] A. Nachman. Global uniqueness for a two-dimensional inverse boundary value problem. *Annals of Mathematics-Second Series*, 143(1):71–96, 1996.
- [77] C. Nicholson and J. a. Freeman. Theory of current source-density analysis and determination of conductivity tensor for anuran cerebellum. *Journal of neurophysiology*, 38(2):356–68, Mar. 1975.
- [78] P. Nicholson. Specific impedance of cerebral white matter. *Experimental neurology*, 401:386–401, 1965.
- [79] A. Nissinen, L. M. Heikkinen, and J. P. Kaipio. The Bayesian approximation error approach for electrical impedance tomography - experimental results. *Measurement Science and Technology*, 19(1):015501, Jan. 2008.
- [80] A. Nissinen and V. Kolehmainen. Reconstruction of Domain Boundary Voltage and Conductivity in Electrical Impedance Tomography Using an Approximation Error. *International Journal for Uncertainty Quantification*, 1(3):203–222, 2011.
- [81] J. Nocedal and S. Wright. *Numerical optimization*. Springer Series in Operations Research and Financial Engineering , Springer-Verlag, New York, 1999.
- [82] T. I. Oh, H. Wi, D. Y. Kim, P. J. Yoo, and E. J. Woo. A fully parallel multi-frequency EIT system with flexible electrode configuration: KHU Mark2. *Physiological measurement*, 32(7):835–49, July 2011.
- [83] B. Packham, H. Koo, A. Romsauerova, S. Ahn, A. McEwan, S. C. Jun, and D. S. Holder. Comparison of frequency difference reconstruction algorithms for the detection of acute stroke using EIT in a realistic head-shaped tank. *Physiological measurement*, 33(5):767–786, May 2012.
- [84] L. Päivärinta. Complex geometrical optics solutions for Lipschitz conductivities. *Revista Matematica Iberoamericana*, 19:57–72, 2003.

- [85] R. P. Patterson and J. Zhang. Evaluation of an EIT reconstruction algorithm using finite difference human thorax models as phantoms. *Physiological measurement*, 24(2):467–75, May 2003.
- [86] N. Polydorides and W. Lionheart. A Matlab toolkit for three-dimensional electrical impedance tomography: a contribution to the Electrical Impedance and Diffuse Optical Reconstruction Software project. *Measurement science and technology*, 13:1871, 2002.
- [87] M. Power. An update on thrombolysis for acute ischaemic stroke. *Advances in Clinical Neuroscience and Rehabilitation*, 4(3):36–37, 2004.
- [88] S. Prince. *Computer vision: models, learning, and inference*. Cambridge University Press, 2012.
- [89] S. Qian and Y. Sheng. A single camera photogrammetry system for multi-angle fast localization of EEG electrodes. *Annals of biomedical engineering*, 39(11):2844–56, Nov. 2011.
- [90] P. Rahmati, M. Soleimani, S. Pullett, I. Frerichs, and A. Adler. Level-set-based reconstruction algorithm for EIT lung images: first clinical results. *Physiological measurement*, 33(5):739–50, May 2012.
- [91] J. Ranck and S. BeMent. The specific impedance of the dorsal columns of cat: an anisotropic medium. *Experimental neurology*, 463:451–463, 1965.
- [92] A. Romsauerova, A. McEwan, L. Horesh, R. Yerworth, R. Bayford, and D. Holder. Multi-frequency electrical impedance tomography (EIT) of the adult human head: initial findings in brain tumours, arteriovenous malformations and chronic stroke, development of an analysis method and calibration. *Physiological measurement*, 27(5):S147–61, May 2006.
- [93] J. Rosell and J. Colominas. Skin impedance from 1 Hz to 1 MHz. *Biomedical Engineering*, 35(8):112–113, 1988.
- [94] C. Rother, V. Kolmogorov, and A. Blake. "grabcut": Interactive foreground extraction using iterated graph cuts. *ACM Trans. Graph.*, 23(3):309–314, Aug. 2004.

- [95] Y. Saad and M. H. Schultz. GMRES: A Generalized Minimal Residual Algorithm for Solving Nonsymmetric Linear Systems. *SIAM Journal on Scientific and Statistical Computing*, 7(3):856–869, 1986.
- [96] F. Santosa. A level-set approach for inverse problems involving obstacles. *ESAIM: Control, Optimisation and Calculus of Variations*, 1(January):17–33, 1996.
- [97] J. K. Seo, J. Lee, S. W. Kim, H. Zribi, and E. J. Woo. Frequency-difference electrical impedance tomography (fdEIT): algorithm development and feasibility study. *Physiological measurement*, 29(8):929–44, Aug. 2008.
- [98] J. Shewchuk. An introduction to the conjugate gradient method without the agonizing pain. *Science*, 1994.
- [99] X. Shi, F. You, F. Fu, R. Liu, Y. You, M. Dai, and X. Dong. Preliminary research on monitoring of cerebral ischemia using electrical impedance tomography technique. *Annual International Conference of the IEEE Engineering in Medicine and Biology Society. IEEE Engineering in Medicine and Biology Society. Conference*, 2008:1188–91, Jan. 2008.
- [100] S. Siltanen, J. Mueller, and D. Isaacson. An implementation of the reconstruction algorithm of A Nachman for the 2D inverse conductivity problem. *Inverse Problems*, 681, 2000.
- [101] M. Soleimani, O. Dorn, and W. R. B. Lionheart. A narrow-band level set method applied to EIT in brain for cryosurgery monitoring. *IEEE transactions on bio-medical engineering*, 53(11):2257–64, Nov. 2006.
- [102] M. Soleimani, W. R. B. Lionheart, and O. Dorn. Level set reconstruction of conductivity and permittivity from boundary electrical measurements using experimental data. *Inverse Problems in Science and Engineering*, 14(2):193–210, Mar. 2006.
- [103] E. Somersalo and M. Cheney. Layer stripping: a direct numerical method for impedance imaging. *Inverse Problems*, 899, 1999.
- [104] E. Somersalo, M. Cheney, and D. Isaacson. Existence and uniqueness for electrode models for electric current computed tomography. *SIAM Journal on Applied Mathematics*, 52(4):1023–1040, 1992.

- [105] N. Soni, K. Paulsen, H. Dehghani, and A. Hartov. Finite Element Implementation of Maxwell's Equations for Image Reconstruction in Electrical Impedance Tomography. *IEEE Transactions on Medical Imaging*, 25(1):55–61, 2006.
- [106] J. Sylvester. A Convergent Layer Stripping Algorithm for the Radially Symmetric Impedance Tomography Problem. *Communications in Partial Differential Equations*, 17(11-12):1955–1994, Jan. 1992.
- [107] C. Tang, F. You, G. Cheng, D. Gao, F. Fu, and X. Dong. Modeling the frequency dependence of the electrical properties of the live human skull. *Physiological measurement*, 30(12):1293–301, Dec. 2009.
- [108] C. Tang, F. You, G. Cheng, D. Gao, F. Fu, G. Yang, and X. Dong. Correlation between structure and resistivity variations of the live human skull. *IEEE transactions on bio-medical engineering*, 55(9):2286–92, Sept. 2008.
- [109] a. T. Tidswell, a. Gibson, R. H. Bayford, and D. S. Holder. Validation of a 3D reconstruction algorithm for EIT of human brain function in a realistic head-shaped tank. *Physiological measurement*, 22(1):177–85, Feb. 2001.
- [110] a. Tizzard, L. Horesh, R. J. Yerworth, D. S. Holder, and R. H. Bayford. Generating accurate finite element meshes for the forward model of the human head in EIT. *Physiological measurement*, 26(2):S251–61, Apr. 2005.
- [111] M. Vauhkonen, J. Kaipio, E. Somersalo, and P. Karjalainen. Electrical impedance tomography with basis constraints. *Inverse Problems*, 13:523, 1997.
- [112] M. Vauhkonen, W. R. Lionheart, L. M. Heikkinen, P. J. Vauhkonen, and J. P. Kaipio. A MATLAB package for the EIDORS project to reconstruct two-dimensional EIT images. *Physiological measurement*, 22(1):107–11, Feb. 2001.
- [113] P. Vauhkonen. Static Three-Dimensional Electrical Impedance Tomography. *Annals of the New York Academy of Sciences*, pages 0–3, 1999.
- [114] P. J. Vauhkonen, M. Vauhkonen, T. Savolainen, and J. P. Kaipio. Three-dimensional electrical impedance tomography based on the complete electrode model. *IEEE transactions on bio-medical engineering*, 46(9):1150–60, Sept. 1999.
- [115] T. Viklands and M. Gulliksson. Optimization tools for solving nonlinear ill-posed problems. In K.-H. Hoffmann, R. Hoppe, and V. Schulz, editors, *Fast Solution of*

- Discretized Optimization Problems*, volume 138 of *ISNM International Series of Numerical Mathematics*, pages 255–264. Birkhäuser Basel, 2001.
- [116] T. Vilhunen and J. Kaipio. Simultaneous reconstruction of electrode contact impedances and internal electrical properties: I. Theory. *Measurement Science and Technology*, 1848, 2002.
- [117] M. Vonach, B. Marson, M. Yun, J. Cardoso, M. Modat, S. Ourselin, and D. Holder. A method for rapid production of subject specific finite element meshes for electrical impedance tomography of the human head. *Physiological measurement*, 33(5):801–16, May 2012.
- [118] Website. CGAL, Computational Geometry Algorithms Library, 2014.
- [119] R. J. Yerworth, L. Horesh, R. H. Bayford, A. Tizzard, and D. S. Holder. Robustness of linear and non-linear reconstructions algorithms for brain EITS. In *IFMBE Proceedings, vol. 11*, volume 44, pages 499–502. Gdansk University of Technology, Gdansk, Poland, 2004.
- [120] R. Zabih and V. Kolmogorov. Spatially coherent clustering using graph cuts. *Proceedings of the 2004 IEEE Computer Society Conference on Computer Vision and Pattern Recognition, 2004. CVPR 2004.*, 2:437–444, 2004.
- [121] Y. Zhang, M. Brady, and S. Smith. Segmentation of brain MR images through a hidden Markov random field model and the expectation-maximization algorithm. *IEEE transactions on medical imaging*, 20(1):45–57, Jan. 2001.
- [122] T. X. Zhao, B. Jacobson, and T. Ribbe. Triple-frequency method for measuring blood impedance. *Physiological measurement*, 14(2):145–56, May 1993.
- [123] E. Ziegel, W. Press, B. Flannery, S. Teukolsky, and W. Vetterling. Numerical Recipes: The Art of Scientific Computing. In *Technometrics*, volume 29, pages 164–168. Nov. 1987.